Analysis and characterisation of biological samples in nano and microfluidic devices using AC and DC electric fields

Óscar Castillo Fernández

Tesis doctoral

Analysis and characterisation of biological samples in nano and microfluidic devices using AC and DC electric fields

Memoria presentada por

Óscar Castillo Fernández

Para optar al grado de **Doctor en Biomedicina**

Universitat de Barcelona

Departament d'Electrònica

Programa de doctorado de Biomedicina

2008-2012

Tesis doctoral dirigida por

Prof. Josep Samitier Martí

Barcelona, 2012

En memoria de José Javier,

Para mis padres,
mis abuelos,
y Lola

Acknowledgement

En primer lloc voldria agrair al Professor Josep Samitier, per donar-me l´oportunitat de realitzar la meva tesi doctoral en el seu grup i laboratori. Gràcies pels consells i les discussions establertes al llarg d´aquests quatre anys.

També vull agrair molt especialment a professors del departament, directors de projectes, i membres del grup que durant aquests anys han tingut algun paper rellevant en la meva feina. En Jaime López, que va ser qui hem va portar al laboratori a treballar amb en Romén i en Miquel. En Gabriel Gomila. Martin Arundell, who proposed me for a PhD position. Toni Homs, Bea , Patrizia. Finalmente, Elena Martínez, que siempre ha tenido tiempo para escuchar, aconsejar, enseñar y ayudar, muchas gracias Elena, te debo una... o dos.

Una part molt important de la feina, la vaig fer martiritzant a preguntes i perseguint a alguns ben intencionats biòlegs. En Xavi Fernández-Busquests, l´Alfred Cortés, en Francesc Miró, Hernando del Portillo, Lorena Martín i Ernest Moles. Molt agraït per la paciència, interès mostrats i pel coneixement i ajut proporcionats.

When I was in Enschede, during my stance in the BIOS group in Twente Universty. Jan Eijkel took care of me, being my teacher, director and also a friend. Thank you Jan. I am also grateful to Prof. Dr. Albert van den Berg for giving me this opportunity. It was also a pleasure to work with Georgette and Jan van Nieuwkasteele.... I would also thank to the large number of people that forms the BIOS group, who let me join the BIOS football team and their winter week in Swiss. It was a nice time.

Especialmente, quiero agradecer su ayuda a dos buenos amigos: Romén y Marc. Primero fueron compañeros de laboratorio y amigos, para finalmente convertirse en magníficos post-docs con los que trabajar y de los que aprender. Además de compartir larguísimas discusiones tanto científicas como personales.

Además, durante todo este tiempo he tenido la suerte de compartir espacio y tiempo con mucha gente del grupo y tengo que decir que me siento profundamente orgulloso de ello. Quiero agradecer a David Izquierdo, su atención y cuidado a todos los detalles, y reconocer además su inestimable ayuda en mi trabajo. A Miriam, la ′sita′, por ayudarme, enseñarme y corregirme mis torpes movimientos por el laboratorio y la sala de cultivos. A Sergio Martínez su apoyo y amistad, *estoy contigo a muerte bròda*. Al Cumi, molts anys han passat des de els temps de Màster, gràcies, ets un exemple i un referent. A los niños perdidos, Coco (eres la más fuerte, niña), Marilia, Marta y Juan Pablo, gracias por vuestro apoyo y cariño, y por esas larguísimas conversaciones sobre lo científico y lo divino, sois un equipo extraordinario y mi wiki personal. A *Queens* agradecerle la visita al final de la fiesta, gracias niña, *nada sería lo mismo sin ti, vamò*. A los *elenos*, les quiero agradecer la aceptación y permitirme el intrusismo. Ana, ja està dona no destorbo més, gràcies de tot cor. Sabine, gracias por estar siempre dispuesta a reír. A Vero, Maria, y Albert, que son contenedores de ciencia y sabiduría, gracias por vuestra ayuda y comentarios...

A los soles de la plataforma, que siempre han hecho todo lo posible para ayudar y facilitar el trabajo. Gracias, María Jesús y Yolanda. Y muy especialmente a Marina que me ha sufrido todos estos años, gracias por toda la paciencia que has tenido conmigo, y por ayudarme en todo.

En el laboratorio 221 del departamento hay mucho potencial y poca campana. Gracias a todos por los ratos compartidos y vuestra compañía. Javi, Juanma, Elia, César y Ana. Un beso.

También tuve la suerte de coincidir con la generación anterior del NanoBio. Muy grande. Quiero agradecer especialmente a Isabel, mi pepito grillo particular, que se haya tomado como algo personal el que este trabajo se acabara. A Pastora, su apoyo y *empujones,* además de la larga lista de buenos consejos. Me dijo una vez: *Todo el mundo debería hacer una tesis en su vida.* Después me dijo: *Tú, acabala.* El Sisqui, el

Mateu (gràcies senyor), la Muriel, la Maru, la Ramona, el Javi, el David, Ivón, Mathias... gracias a todos, en estos momentos echo de menos a los que no estáis cerca, me hubiera encantado compartir este momento con vosotros.

Mi familia también ha tenido mucho que ver en este proceso. En especial Lola. Tengo que reconocer que sin ella habría sido imposible terminar este trabajo, muchas gracias cielo. Gracias también a mi hermano Alberto, por estar siempre atento a todo y por tener esa paciencia infinita conmigo. También quiero agradecer a mis padres su aportación. A mi madre Marina, por darme todo lo que tengo, y enseñarme a confiar en la intuición. A mi padre, Eusebio, mi ángel de la guarda, mi mejor profesor y el auténtico sufridor de esta aventura, gracias. También quiero agradecer y recordar a mis mayores, que de algún modo, mediante su educación, apoyo incondicional y el ejemplo han contribuido a que culminara este trabajo: Luisa, Paco, María, Paco, Encarna, José, Aida, Evaristo, Lucía, Gloria, Constante, Mari Carmen y muy especialmente a José Javier.

List of contents:

Abbreviations

AC	Alternating current
DC	Direct current
DEP	Dielectrophoresis
DNA	Deoxyribonucleic acid
EOF	Electro osmotic flow
EP	Electrophoresis
LOC	Lab on a chip
MEMS	Micro electro mechanical system
nDEP	Negative dielectrophoresis
PBS	Phosphate buffered saline
PCR	Polymerase chain reaction
pDEP	Positive dielectrophoresis
PDMS	Polydimethylsiloxane
POC	Point of care
PVP	Polyvynilpyrrolidone
RBC	Red blood cell
TBE	Tris Borate EDTA solution
WBC	White blood cell
μTAS	Micro total analysis systems

Chapter 1 : Introduction

This chapter deals with the basic motivation of this thesis. We will introduce the main application of the tools we developed: the generation of autonomous, compact and easy to use systems to provide solutions to diagnostic needs in primary care units.

First, we will review the current state-of-the art in microfabrication and microfluidics. Afterwards, we will list the requirements of point-of-care devices and we will present an overview of the materials, methodologies and samples involved. Then, we will present the capabilities of electric fields in handling and sensing biological samples. Finally we make an overview of the three main topics covered in this work.

1.1. Lab on a Chip for point-of-care solutions

During the last 50 years a huge variety of silicon-based microfabrication techniques were developed. Nowadays, these fabrication techniques have been also applied to other materials such as glass or polymers. The fabrication knowledge acquired and the new materials lead to the development of miniaturised electro mechanical components, called MEMS, which combine electrical components with sensors and actuators. When MEMS are used to contain and move fluids, we use the term microfluidics devices.

The combination of microfluidics with biocompatible materials opened new perspectives in biomedical applications. New in vitro miniaturised tools and platforms based on micro and nanofluidics allow the quantification, managing and characterisation of biological samples at their metric scale. These systems, called lab on a chip devices (LOC) or micro total analysis systems (μTAS), are advantageous in comparison to traditional biological techniques due to the reduction of the sample and reagent volumes and the increase in the velocity of processing (*1*). These two concepts aims complete, compact and automated systems that could perform any laboratory process or analytical study under low volume conditions, high efficiency, reduced fabrication costs (*2, 3*).

The characteristics of LOC and μTAS devices imply benefits in analytical biomedical devices and provide solutions to the requirements of point of care devices (POC) (*4, 5*). Point of care devices can be defined as devices that provide efficient analytical results in a primary medical care environment. Such devices are used to support the traditional symptomatic diagnostics, providing fast and cheap diagnostics, accurate additional information, facilitating illness monitoring and therapy efficiency control.

The point of care systems are particularly important in developing countries, where there is a lack of resources in terms of laboratory facilities and trained personal. Actually, 95% of worldwide deaths due to major infectious diseases such as respiratory infections, malaria, AIDS and tuberculosis take place in these countries. Moreover, it

has been demonstrated that the combination of diagnostic based in symptomatic methods, with a syndromic management of an illness accelerate drug resistance (*5, 6*). For this reason, the World Health Organisation (WHO) has introduced several programs and projects to foster the research and production of lateral flow rapid diagnostic tests (RDT) for malaria diagnosis (*7*).

On the other hand, in developed countries it is important to control public health costs, especially now that the aging of the population implies a higher prevalence of chronic diseases. Point of care systems are meant to improve the quality and reduce the costs of the medical assistance giving faster diagnosis in emergency care, near-patient solutions such as ambulatory and home screening, and patient self-monitoring of chronic illnesses. (*5, 6*).

The requirements that LOC and μTAS have to accomplish to become useful point of care devices are well defined (*4-6*) and additionally to their high efficiency and reliability, there are other important issues that has to be taken in account when designing and fabricating them:

1) Reduced cost: the fabrication costs are normally related to the material employed, which defines the fabrication procedure, and the design possibilities.

2) Sample manipulation: the sample taken from the patient is a highly complex system. To provide reliable data and an efficient analysis, samples should be pre-treated and in some cases purified.

3) Fluid actuation and control: the analytical procedures require fluid handling to manage the reagents or the sample.

4) Instrumentation: the challenge is to include a detection system sensitive enough to signals coming from low volumes of sample, while accomplishing low cost, compactness and low power consumption.

5) Storage and Transport: especially in developing countries, the device will be subjected to strong environmental conditions as high temperatures and humidity. The devices and the contained reagents must resist these conditions.

In this thesis, we focused our work in two of the requirements listed above: sample manipulation and compact instrumentation. Regarding the storage and transport issues, the use of biological and chemical reagents is completely avoided, as the systems we propose are based on direct electrical signalling and sensing. This will increase the lifetime and robustness of the final device.

Fluid actuation and control, which are critical issues in microfluidics and lab on chip research, are not addressed specifically as a research topic in this thesis. We have used pressure driven fluidic pumps to control the fluid motion.

One of the requirements of a point of care device is the low fabrication cost, which is strongly dependent to the materials used. Additionally, materials have to be biocompatible and transparent in order to allow optical readout of the test results. In this thesis we chose fused silica to fabricate nanochannels because of the capabilities of the microfabrication technologies, and PDMS to fabricate the microchannels, because of its simple and cheap fabrication process.

1.2. Modular architecture of point-of-care devices

An idealised microsystem for a point of care application would include modules for cell culture, cell handling or sorting to obtain target cells, cell lysis to obtain their DNA, purification and amplification process and finally, the detection.

It is possible to find a large number of microfluidic systems focussed on single specific procedures or steps such as cell culture and signalling (*8-10*), cell sorting (*11-14*), cell lysis (*15, 16*), immunoanalysis (*17*), PCR amplification (*18-20*), electrophoresis separation (*21, 22*) and biosensing (*23, 24*). These individual devices can eventually be integrated in a modular and sequenced system that performs the whole analytical process (Figure 1.1) (*25-27*). We will focus our work on the cell sorting, the detection step and the DNA manipulation.

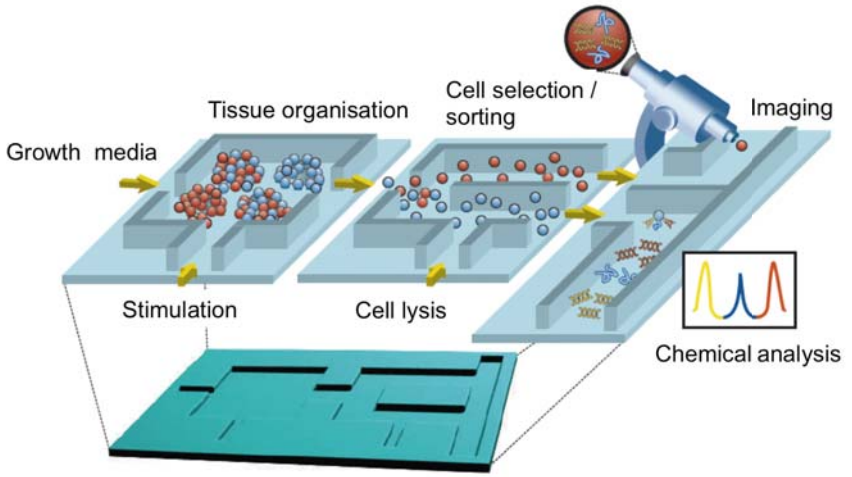

Figure 1.1: Schematic representation of a modular system for cell analysis. In this scheme three independent and interconnected modules are represented: a cell culture module to obtain the sample, a cell selection module to separate, manipulate or lyse cells and the analysis module. (25)

One of the most important tools in pathogen detection and diagnostics is the DNA separation by electrophoresis under gel and capillary movement restrictions (*28*).

In 2005, Pal et al. reported a lab on a chip device that included PCR amplification and capillary gel electrophoresis integrated in a simple chip (*18*). However, gel capillary systems are expensive to fabricate and have low reproducibility (*29*). As an alternative solution, it was proposed the fabrication of micro and nanostructures to generate

matrices that emulate the gel structure. These are viewed as a great opportunity to achieve a cheap and gel-free DNA separation method, which would be easy to fabricate and integrate (*30, 31*). Once separated, the DNA molecules have to be detected. Optical detection of labelled DNA is often used, although some devices work with electrical detection, which can be much easily integrated in simple instrumentation devices (*32, 33*).

Other technique highly relevant in biomedical applications is flow cytometry. This is a technique for cell counting and, in combination with inmunoassays and labelling, it can also detect changes in the morphology of cell surface membranes, cell structure or differences in protein composition. For this reason, flow cytometers are widely used in hospitals and laboratories (*34*). Conventional flow cytometers use complicated and expensive optical instrumentation. Microfluidic based cytometers, have been proposed a more affordable alternative, based in the Coulter Counter concept (*35*) and use electrical detection, which gives them versatility with good results (*36*). Still, the instrumentation used requires impedance analysers and lock-in systems, which are expensive and complex set-ups.

In addition, target cells have to be manipulated and sorted before counting. This can be done by tools such as optical and magnetic tweezers (*37, 38*), micromanipulators and micropipettes (*39*). These techniques, however, require large and complex set-ups. A better option to be integrated in Lab on a chip devices is the use of electrical forces, which allow selective cell manipulation applying electric fields produced by microelectrodes included in the device (*40*).

In this thesis, we focused our research on the application of electric fields for DNA separation to provide effective solutions to DNA separation by gel-free electrophoresis and cell counting and sorting modules under continuous flow conditions using cheap and compact impedance based instrumentation. We address our efforts to develop simple solutions, that can be easily included into a compact instrument.

Point of care devices are oriented to perform analytical processes with samples obtained directly from patients. Usually, these samples will be obtained from physiological fluids. The most common one is whole blood, normally obtained by venepuncture or finger prick (*17, 41*). However, other less invasive fluids are also used, such as saliva (*42, 43*) and urine (*44*).

We centred our work in blood samples, as a defined strategy of our research group. Basically, in this work we have used two types of samples: red blood cells (RBCs) and monocytes (see Figure 1.2). RBCs were obtained from donor whole blood. Monocytes, which are larger cells from the immune system, are related to inflammatory processes. In this work, monocytes were obtained from THP-1 cell line (ATCC). The DNA sample model used was λ-DNA (Sigma-Aldrich) as a very large molecule.

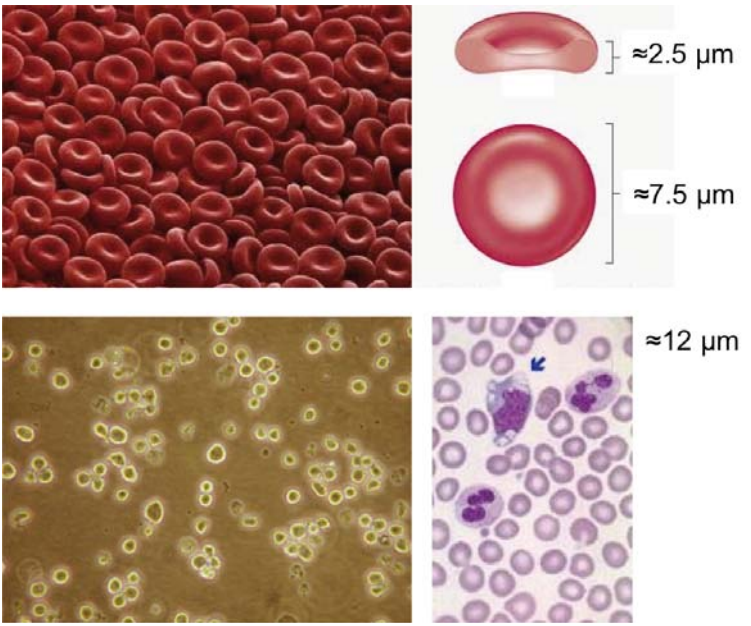

Figure 1.2: Images of RBCs and THP-1 suspensions. The top right image is a detailed scheme of the RBC morphology. At the bottom right image it is represented a comparison of the THP-1 (with nucleus labelled) cell line surrounded by RBCs (with no nucleus).

1.3. Introduction to the electric field theory in microfluidic environments

1.3.1. Electrical properties of biological samples

Biological samples, such complex tissues, single cells or individual proteins, are all formed by different components. Cells, for example, are composed by cell membrane, cytoplasm, organelles and nucleus. The organelles and even the nucleus have also a membrane and fluids inside which contain lipids, proteins and so on. Therefore, the effects of electric fields on biological samples will depend on the electrical charges and dielectric behaviour of each of their components.

When an electric field is applied to a material, the energy is lost by frictional motion of the charge carriers (resistive loss), or stored by the polarization of its components. This response of the material to the external electric field generally depends on the frequency of the field, as the polarization of a material does not respond instantaneously to the field variations. For this reason, the permittivity is treated as a complex function of the angular frequency of the applied field. Complex permittivity expresses the dependency in frequency of all the elements that constitute the sample, including each particular polarisation process.

The material polarisation depends on: (1) the orientation of permanent dipoles, as for example water molecules; (2) the orientation of charges at atomic level; and (3) the charge accumulation at dielectric interfaces (*48*). Figure 1.3 shows an idealised spectrum of the evolution of the complex permittivity of a cell suspension as a function of the frequency of the electric field applied. The steps in the graph are called dispersions and they are due to particular polarisation processes, which depend on the frequency of the electric field.

H.P. Schwan studied the evolution of dielectric dispersions with the frequency using biological tissues and cell suspensions (*49, 50*). Schwan established three main dispersions (α, β, γ). The α-dispersion occurs at low frequencies, around 10^2 Hz. It is

attributed to the polarisation of the ionic double layer around the cell. The β-dispersion is attributed to the Maxwell-Wagner effect, which normally occurs at the interface between two different dielectrics. This polarisation normally takes place around 10^6 Hz. The γ-dispersion is due to the incapacity of small polar molecules to follow the variations of the field. This dispersion is produced above 10^{10} Hz. Around 10^8 Hz, it is found another dispersion, called δ-dispersion, that is attributed to the non-rotation of some large polar molecules such as proteins.

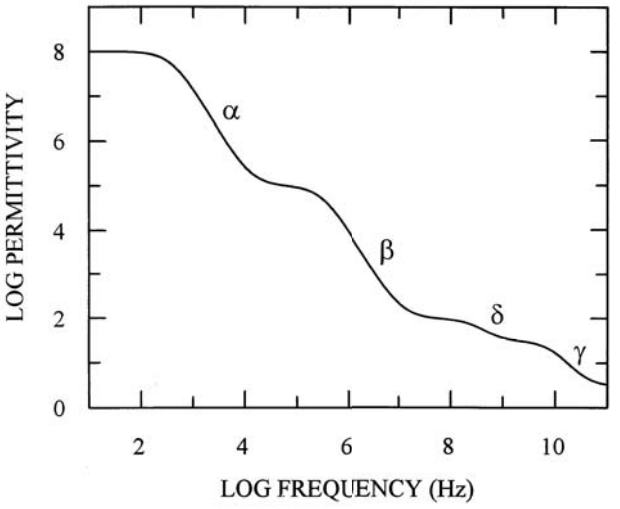

Figure 1.3: Idealised representation of the spectrum of the dielectric properties of a cell suspension. The step changes in the permittivity are called dispersions. α dispersion is due to the tangential crossing of ions across the cell surface, β is due to the Maxwell-Wagner effect on the cell membrane and γ-δ dispersions are due to molecules.

The dielectric nature of the biological samples is expressed by the complex permittivity ε^*:

$$\varepsilon^* = \varepsilon_0 \varepsilon - \frac{\sigma}{\omega} i \qquad \text{Equation 1.}$$

where ε and σ are the permittivity and conductivity of the dielectric, respectively, ω is the angular frequency of the applied field and i is $\sqrt{-1}$.

1.3.2. Debye length. Electrolyte interface

When a charged particle is placed in an electrolyte, free ions from the solution are attracted to it, generating a charged cloud around. The thickness of this ionic cloud is defined by the Debye length, λ_D, which is expressed by equation 2:

$$\lambda_D = \sqrt{\frac{\varepsilon k_B T}{2e^2 I}} \qquad \text{Equation 2.}$$

where ε is the permittivity of the solution, k_B is the Boltzmann constant, T is the temperature, e is the elementary charge and I is the ionic strength of the solution.

This Debye length is strongly dependent on the characteristics of the solution instead of the particle characteristics. In biological media, the Debye length is mostly affected by the ionic strength of the media and it decreases when the ionic strength increases.

This ion accumulation around the charged particles forms the so-called double layer, and it is structured in two main layers (Figure 1.4). First, close to the charged surface, it is placed the Stern layer, where the ions are tightly bounded to the surface. In this layer, the electric potential decays in a linear profile. Behind the Stern layer, there is the diffuse layer, where the counter ions experience less strong electrical attraction than at the first layer, and they are able to diffuse. The density of ions and the electric potential decay exponentially, with a characteristic distance given by the Debye length.

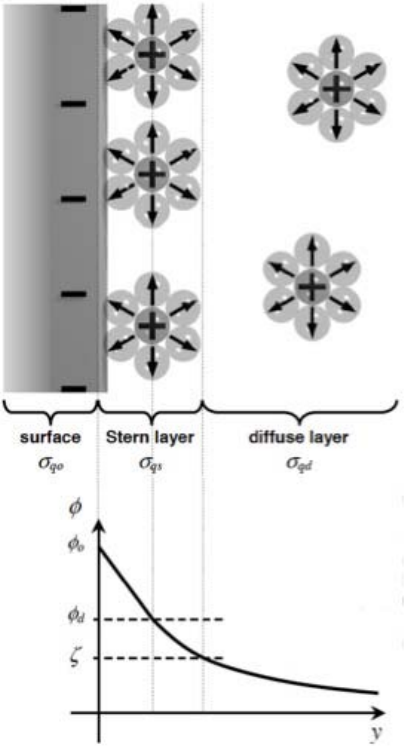

Figure 1.4: Schematic diagram of the layer of bond counter ions, the Stern layer, and the diffuse layer at a charged surface. It is also shown the variation of the electrical potential as a function of the distance from the surface, remarking the diffuse layer potential ϕ_d and the potential at the hydrodynamic slip plane ζ, the zeta potential (51).

The accumulation of charges with an opposite sign around the particle changes its effective charge. Thus, it is used the zeta potential parameter. The zeta potential, ζ, is defined as the potential at the shear plane and it is strongly dependent to the charge density of the surface and the ionic strength of the liquid.

1.3.3. Electrode-electrolyte interface

Similar charge accumulation also happens at an electrode interface, when electrodes are immersed in electrolyte solutions. Due to the charge of the metallic surface of the electrodes, positive ions are attracted to it, while negative charges are repelled. When an electric potential is applied through the electrodes immersed in a fluidic electrolyte, the charge distribution changes analogously as the charging process of a capacitor. This phenomenon is called electrode polarisation (*49*).

A double layer is also formed on the surface of electrodes. The first layer is determined by the ions immobilized on the electrode surface and it can be modelled by the Helmholtz model. Figure 1.5 represents the distribution of the so-called Helmholtz planes, the inner Helmholtz plane (*iHP*) and the outer plane (*oHP*), with the interface potential. Figure 1.5 also plots the interface potential according to the evolution of the ion concentration. Note that the difference between these schemes with the Stern approximation represented in Figure 1.4, is the incorporation of the solvated ions at the *iHP* layer.

The Helmholtz model determines that the electrode polarisation is affected by the ion accumulation. The interfaces represented in Figure 1.5 would behave like simple capacitors, one for each layer formed. The Helmholtz model defines the capacitor behaviour of the fixed layer (*iHP* and *oHP*) as an ideal capacitor. Then, C_H is defined in equation 3, where ε_r is the dielectric permittivity of the electrolyte, A_e is the area of the electrode interface and d_{oHP} is the length of the outer Helmholtz plane (*oHP*).

$$C_H = \varepsilon_r \varepsilon_0 \frac{A_e}{d_{oHP}} \qquad \text{Equation 3.}$$

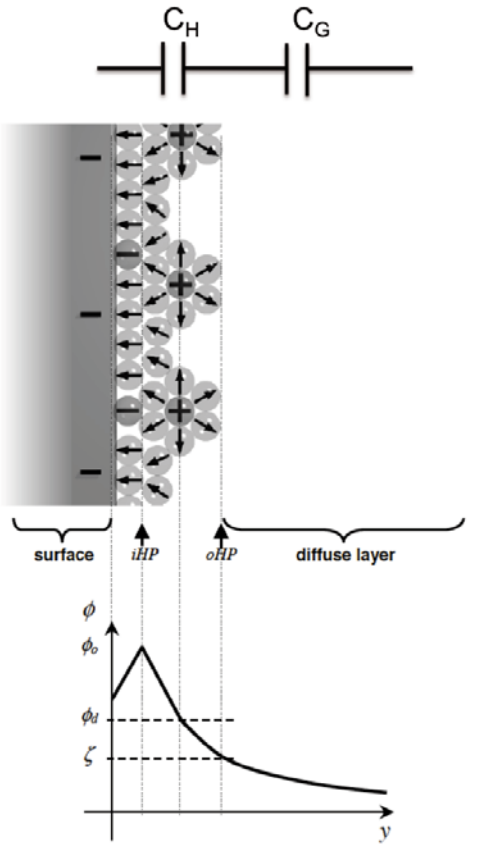

Figure 1.5: Schematic representation of the internal structure of the interface electrode-electrolyte, including the inner Helmholtz layer (iHP) of specific absorbed ions and the outer Helmholzt plane (oHP) with the hydrated ions. The evolution of the interface potential is related to this structure (51).

The capacitance due to the diffuse layer can be expressed by the Gouy-Chapman capacity (C_G), which is defined by the equation 4. The length of this layer is expressed in terms of the Debye length. The hyperbolic cosine compensates the effects of the mobile charges, where the c is the electrolyte concentration of ions, z is the ionic charge and V_t is the thermal voltage (k_BT/e), where k_B is the Boltzman constant, T is temperature and e is the electron charge.

$$C_G = \varepsilon_0 \varepsilon_r \frac{A}{\lambda_D} \cosh\left(\frac{zcV_0}{2V_t}\right) \qquad \text{Equation 4.}$$

Then, the total capacitance of the system, named interfacial capacitance (C_I), is expressed as the serial combination of Helmholtz capacitance (C_H) and the Gouy-Chapman capacitance (C_G) (equation 5).

$$\frac{1}{C_I} = \frac{1}{C_H} + \frac{1}{C_G} \qquad \text{Equation 5.}$$

For the electrode geometries used in this thesis, the C_I capacitance affects to the system at low frequencies, between 10^2 to 10^3 Hz. For that reason, the frequencies used in the Cell handling and Sensing chapters will be over these values. In the case of the DNA handling we used high electric fields, low conductivity buffers and large electrodes. Thus, this effect was not considered.

1.3.4. Electrophoresis

The electrophoresis is defined as the motion of a charged particle within a uniform electric field. Due to such electric field of magnitude E, a particle with a charge Q will experience a Coulomb force expressed by equation 6.

$$F_{EP} = QE \qquad \text{Equation 6.}$$

The velocity of a particle is defined by its intrinsic mobility in a given buffer solution. This specific mobility of a particle (μ_e) could be expressed by equation 7.

$$\mu_e = \frac{v}{E} \propto \frac{\zeta}{\eta} \qquad \text{Equation 7.}$$

where v is the linear velocity of the particle, and E is the electric field applied. The mobility of the particle is then independent to the electric field applied, and proportional to the zeta potential (ζ), which depends on the ionic strength of the fluid, and on its dynamic viscosity (η).

The Electrophoretic force could generate the movement of a fluid (*51*). When the surface walls of a microfluidic device are charged (i.e. fused silica) a double layer is established along these surfaces. When the electric field is applied, the mobile charges of the diffuse layer migrate towards the electrode of opposed charge. Since ions are solvated by water, the buffer fluid is also mobilised being dragged along by the migrating charges and producing the so-called electroosmotic flow (EOF).

1.4.5. Dielectrophoresis

When a cell is placed under an electric field, their inner elements, free charges and surrounding media are polarised, so a dipole is induced. As it is represented in Figure 1.6, the polarisation of the cell is related to the conductivity of the cell surrounding media and its dielectric characteristics.

If the electric field is non-homogeneous, the cell will experience a translational force because the induced dipole will experience forces of different magnitude on its negative and positive extremes. These forces depend on the magnitude and the frequency of the applied field, defining the so-called dielectrophoretic forces (DEP).

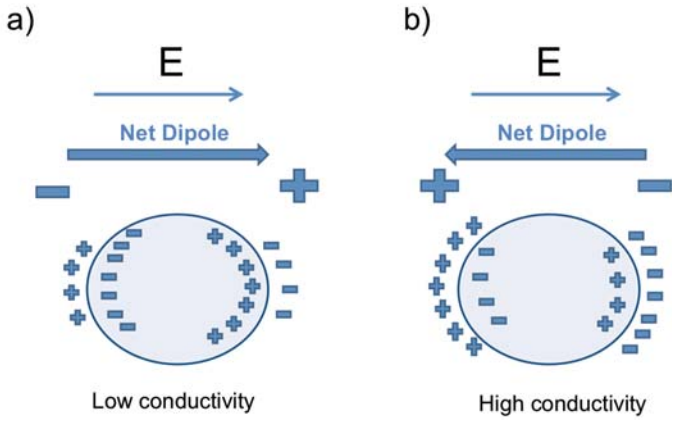

Figure 1.6: Schematic diagram of how different dielectric particles (cells) polarise when they have a much higher (a) or much lower (b) polarisability tan the suspending fluid medium. If the polarisability is higher, more charges are produced on the inside of the particle/fluid interface and there is a net dipole across the particle on the direction of the applied field. In the case (b) where the polarisability is lower, more charges are produced outside of the interface and the net dipole is in the opposite direction against the field.

In the case of spherical particles the time averaged DEP force is expressed by the following equation.

$$\left\langle F_{DEP} \right\rangle = 4\pi\varepsilon_m R^3 \,\mathrm{Re}\left[K(\omega)\right]\nabla\left|E_{rms}\right|^2 \qquad \text{Equation 8.}$$

where R is the radius of the particle, ε_m is the complex permittivity of the media, E_{rms} is the root mean square of the electric field, and Re $[K(\omega)]$ is the real part of the Claussius-Mossotti factor (CM), defined by the relationship between the complex permittivity of the surrounding media and the particle and, thus, depending on frequency (ω). The CM factor for spherical particles is expressed by equation 9:

$$K(\omega) = \frac{\varepsilon_p^* - \varepsilon_m^*}{\varepsilon_p^* + 2\varepsilon_m^*}$$ Equation 9.

where the indices *p* and *m* indicate the nature of the complex permittivity of the particle or the media, respectively. The interval range of Re [*K(ω)*] is between -0.5 and 1. The sign of Re [*K(ω)*] defines the sign of the DEP force. When the Re [*K(ω)*] is greater than 0, meaning that the cell is more polarisable than the medium (see Figure 1.6), the particle moves towards to regions of maximum electric field and the DEP force is positive (pDEP). When the cell is less polarisable than the medium, Re [*K(ω)*] is negative, the particle moves away from strong electric field regions and the DEP force is negative (nDEP).

The CM factor is related to the complex permittivity of cells, defined by the characteristics of the cell membrane and the density and conductivity of the cytoplasm. Therefore, the CM factor is used to monitor differences between cells, to distinguish between infected and non-infected cells, or to sense the immunologic cell activation.

1.4. Objectives

The objectives of this study are twofold, understanding the behaviour of the biological entities on our devices and designing modular systems to perform separation and sensing that can be integrated in a compact system. In this thesis we developed new methods for DNA and blood cells separation and sensing by using electric fields in micro and nanofluidic environments.

In chapter 2: *"Handling DNA molecules with electrophoresis"*, we investigate the dependence of DNA mobility with the electric field when the molecules are confined in a nanochannel, to determine if the gel-free electrophoresis separation capabilities is due by dielectrophoretic phenomena.

Indeed, we have studied the behaviour of λ-DNA inside 20 nm nanoslits in response to the electric field and investigated the mechanisms behind its mobility dependency. In particular, we have investigated if the roughness in the channel walls could be able to generate field non-homogeneities that lead to the trapping of DNA molecules by dielectrophoresis. The results obtained indicate that is indeed possible that the presence of rigid obstacles in the DNA pathway can induce DNA separation and mobility dependency with the applied electric field.

The aim of chapter 3: *"Handling cells with dielectrophoresis"* is study the utilisation of dielectrophoretic forces to separate cells by size, under a physiological buffer and continuous flow conditions.

We have developed a new dielectrophoretic separation system based on the competition of dielectrophoretic forces with fluidic dragging forces to generate a size depending sorting. We applied this system to separate red blood cells and monocytes, under physiological and continuous flow conditions. The system use electrical barriers that are able to deflect the cells in its transit, in competition with fluidic dragging forces.

In chapter 4: *"Impedance cytometer analysis"* we have focused on developing a custom-made instrumentation to achieve cell counting and sizing under a cheap, compact and fast electronic system.

In particular, we present a custom-made electronics able to count particles in a fluid at high fluid velocities. We also present a simple approach to validate the electrical counting based on high speed synchronised electrical and optical signals. Its detection capabilities have been tested by counting and sizing red blood cells and monocytes.

In chapter 5: *"Microcytometer with hydrodynamic focussing"* we used the hydrodynamic focussing principle to improve the benefits of the coplanar electrode architecture system.

The microfluidic devices used to validate the instrumentation were based in coplanar electrodes, which are easy to fabricate and cheap. But this geometry, traditionally used for in sensors, presents an important drawback, which is the non-homogeneity distribution of the electric field over the sensing area. This distribution of the electric field results in a sensitivity of the system that depends on the distance between the cell and the electrodes.

We centred our work in two aspects: first we demonstrated that the hydrodynamic focussing increases the sensitivity of the counting system, while providing a useful method to align the cells. Second, we use the hydrodynamic focussing to increase the resolution and detection capabilities to reduce errors when evaluating the cell density from the obtained counts from a sample.

References:

1. G. M. Whitesides, The origins and the future of microfluidics. *Nature* **442**, 368 (2006).

2. T. Vilkner, D. Janasek, A. Manz, Micro total analysis systems. Recent developments. *Analytical Chemistry* **76**, 3373 (2004).

3. P. S. Dittrich, K. Tachikawa, A. Manz, Micro total analysis systems. Latest advancements and trends. *Analytical Chemistry* **78**, 3887 (2006).

4. P. Yager, T. Edwards, E. Fu, K. Helton *et al.*, Microfluidic diagnostic technologies for global public health. *Nature* **442**, 412 (2006).

5. P. Yager, G. J. Domingo, J. Gerdes, Point-of-Care Diagnostics for Global Health. *Annual Review of Biomedical Engineering* **10**, 107 (2008).

6. C. D. Chin, V. Linder, S. K. Sia, Lab-on-a-chip devices for global health: Past studies and future opportunities. *Lab on a Chip* **7**, 41 (2007).

7. C. K. Murray, R. A. Gasser, Jr., A. J. Magill, R. S. Miller, Update on Rapid Diagnostic Testing for Malaria. *Clin. Microbiol. Rev.* **21**, 97 (January 1, 2008, 2008).

8. A. Tourovskaia, X. Figueroa-Masot, A. Folch, Differentiation-on-a-chip: A microfluidic platform for long-term cell culture studies. *Lab on a Chip* **5**, 14 (2005).

9. A. M. Taylor, M. Blurton-Jones, S. W. Rhee, D. H. Cribbs *et al.*, A microfluidic culture platform for CNS axonal injury, regeneration and transport. *Nature Methods* **2**, 599 (2005).

10. C. Y. Tay, S. A. Irvine, F. Y. C. Boey, L. P. Tan *et al.*, Micro-/Nano-engineered Cellular Responses for Soft Tissue Engineering and Biomedical Applications. *Small* **7**, 1361 (2011).

11. M. S. Pommer, Y. Zhang, N. Keerthi, D. Chen *et al.*, Dielectrophoretic separation of platelets from diluted whole blood in microfluidic channels. *Electrophoresis* **29**, 1213 (2008).

12. A. Valero, T. Braschler, N. Demierre, P. Renaud, A miniaturized continuous dielectrophoretic cell sorter and its applications. *Biomicrofluidics* **4**, 022807 (2010).

13. S. Choi, S. Song, C. Choi, J.-K. Park, Microfluidic Self-Sorting of Mammalian Cells to Achieve Cell Cycle Synchrony by Hydrophoresis. *Analytical Chemistry* **81**, 1964 (2009).

14. H.-S. Moon, K. Kwon, S.-I. Kim, H. Han *et al.*, Continuous separation of breast cancer cells from blood samples using multi-orifice flow fractionation (MOFF) and dielectrophoresis (DEP). *Lab on a Chip* **11**, 1118 (2011).

15. C.-P. Jen, J.-H. Hsiao, N. A. Maslov, Single-Cell Chemical Lysis on Microfluidic Chips with Arrays of Microwells. *Sensors* **12**, 347 (2011).

16. A. D. Hargis, J. P. Alarie, J. M. Ramsey, Characterization of cell lysis events on a microfluidic device for high-throughput single cell analysis. *Electrophoresis* **32**, 3172 (2011).

17. H. Jiang, X. Weng, D. Li, Microfluidic whole-blood immunoassays. *Microfluidics and Nanofluidics* **10**, 941 (2011).

18. R. Pal, M. Yang, R. Lin, B. N. Johnson *et al.*, An integrated microfluidic device for influenza and other genetic analyses. *Lab on a Chip* **5**, 1024 (2005).

19. K. Khairnar, D. Martin, R. Lau, F. Ralevski *et al.*, Multiplex real-time quantitative PCR, microscopy and rapid diagnostic immuno-chromatographic tests for the detection of Plasmodium spp: performance, limit of detection analysis and quality assurance. *Malaria Journal* **8**, 284 (2009).

20. F. Ahmad, S. A. Hashsham, Miniaturized nucleic acid amplification systems for rapid and point-of-care diagnostics: A review. *Analytica Chimica Acta* **733**, 1 (2012).

21. L. Kremser, D. Blaas, E. Kenndler, Capillary electrophoresis of biological particles: Viruses, bacteria, and eukaryotic cells. *Electrophoresis* **25**, 2282 (2004).

22. J. Regtmeier, R. Eichhorn, M. Viefhues, L. Bogunovic *et al.*, Electrodeless dielectrophoresis for bioanalysis: Theory, devices and applications. *Electrophoresis* **32**, 2253 (2001).

23. Y. Tanaka, K. Sato, T. Shimizu, M. Yamato *et al.*, Biological cells on microchips: New technologies and applications. *Biosensors & Bioelectronics* **23**, 449 (2007).

24. F. S. Rodrigues Ribeiro Teles, L. A. Pires de Távora Tavira, L. J. Pina da Fonseca, Biosensors as rapid diagnostic tests for tropical diseases. *Critical Reviews in Clinical Laboratory Sciences* **47**, 139 (2010).

25. J. El-Ali, P. K. Sorger, K. F. Jensen, Cells on chips. *Nature* **442**, 403 (2006).

26. P. S. Dittrich, A. Manz, Lab-on-a-chip: microfluidics in drug discovery. *Nature Reviews Drug Discovery* **5**, 210 (2006).

27. R. N. Zare, S. Kim, Microfluidic Platforms for Single-Cell Analysis. *Annual Review of Biomedical Engineering* **12**, 187 (2010).

28. F. Sanger, A. R. Coulson, A rapid method for determining sequences in DNA by primed synthesis with DNA polymerase. *Journal of Molecular Biology* **94**, 441 (1975).

29. C. P. Fredlake, D. G. Hert, T. P. Niedringhaus, J. S. Lin *et al.*, Divergent dispersion behavior of ssDNA fragments during microchip electrophoresis in pDMA and LPA entangled polymer networks. *Electrophoresis* **33**, 1411 (2012).

30. K. D. Dorfman, DNA electrophoresis in microfabricated devices. *Reviews of Modern Physics* **82**, 2903 (2010).

31. G. B. Salieb-Beugelaar, K. D. Dorfman, A. v. d. Berg, J. C. T. Eijkel, Electrophoretic separation of DNA in gels and nanostructures. *Lab on a Chip* **9**, 2508 (2009).

32. Y.-C. Jang, S. K. Jha, R. Chand, K. Islam *et al.*, Capillary electrophoresis microchip for direct amperometric detection of DNA fragments. *Electrophoresis* **32**, 913 (2011).

33. M. H. Ghanim, M. Z. Abdullah, Integrating amperometric detection with electrophoresis microchip devices for biochemical assays: Recent developments. *Talanta* **85**, 28 (2011).

34. H. M. Shapiro, *Practical flow cytometry*. Practical flow cytometry, Third edition (Wiley Liss, New York, ed. Third edition, 1995).

35. W. H. Coulter, U. S. P. a. T. Office, Ed. (United States, 1953), vol. 2,656,508.

36. T. Sun, H. Morgan, Single-cell microfluidic impedance cytometry: a review. *Microfluidics and Nanofluidics* **8**, 423 (2010).

37. M. Ozkan, T. Pisanic, J. Scheel, C. Barlow *et al.*, Electro-Optical Platform for the Manipulation of Live Cells. *Langmuir* **19**, 1532 (2003/03/01, 2002).

38. M. Ozkan, M. Wang, C. Ozkan, R. Flynn *et al.*, Optical Manipulation of Objects and Biological Cells in Microfluidic Devices. *Biomedical Microdevices* **5**, 61 (2003).

39. H. Thielecke, I. Impidjati, H. Zimmermann, G. Fuhr, Gentle cell handling with an ultra-slow instrument: creep-manipulation of cells. *Microsystem Technologies* **11**, 1230 (2005).

40. J. Voldman, Electrical forces for microscale cell mnaipulation. *Annual Review of Biomedical Engineering* **8**, 425 (2006).

41. M. Toner, D. Irimia, BLOOD-ON-A-CHIP. *Annual Review of Biomedical Engineering* **7**, 77 (2005).

42. B. L. Ziober, M. G. Mauk, E. M. Falls, Z. Chen *et al.*, Lab-on-a-chip for oral cancer screening and diagnosis. *Head and Neck-Journal for the Sciences and Specialties of the Head and Neck* **30**, 111 (2008).

43. R. W. Hart, M. G. Mauk, C. Liu, X. Qiu *et al.*, Point-of-care oral-based diagnostics. *Oral Diseases* **17**, 745 (2011).

44. C.-C. Lin, C.-C. Tseng, T.-K. Chuang, D.-S. Lee *et al.*, Urine analysis in microfluidic devices. *Analyst* **136**, 2669 (2011).

45. S. Pennathur, F. Baldessari, J. G. Santiago, M. G. Kattah *et al.*, Free-Solution Oligonucleotide Separation in Nanoscale Channels. *Analytical Chemistry* **79**, 8316 (2007).

46. J. D. Cross, E. A. Strychalski, H. G. Craighead, Size-dependent DNA mobility in nanochannels. *Journal of Applied Physics* **102**, 024701 (2007).

47. G. B. Salieb-Beugelaar, J. Teapal, J. v. Nieuwkasteele, D. Wijnperle *et al.*, Field-Dependent DNA Mobility in 20 nm High Nanoslits. *Nano Letters* **8**, 1785 (2008).

48. G. H. Markx, C. L. Davey, The dielectric properties of biological cells at radiofrequencies: applications in biotechnology. *Enzyme and Microbial Technology* **25**, 161 (1999).

49. H. P. Schwan, in Engineering in Medicine and Biology Society, 1990., Proceedings of the Twelfth Annual International Conference of the IEEE. (1990), pp. 11-11.

50. H. P. Schwan, in Engineering in Medicine and Biology Society, 1994. Engineering Advances: New Opportunities for Biomedical Engineers. Proceedings of the 16th Annual International Conference of the IEEE. (1994), pp. A70-A71 vol.1.

51. H. Morgan, N. G. Green, AC Electrokinetics: colloids and nanoparticles. *Herts: Research Studies Press*, (2003).

Chapter 2 : Handling DNA molecules with electrophoresis

In this chapter we investigate the electrokinetic transport behaviour of λ-DNA (48 kbp) in nanochannels. For this purpose, 20 nm high and 3 μm wide fused silica nanoslits were used and DC and AC (1kHz) electrical fields were applied to understand the phenomenon that allow DNA separation according to its molecular size.

We present theoretical simulations revealing that the roughness of the walls of the nanochannels could produce dielectrophoretic forces over the DNA molecules. On the contrary, experimental results show a number of phenomena that are typical in DNA transport through gels or polymer solutions: preferred pathways, caterpillar movement, field-dependent mobility and trapping at high field strengths. Such phenomena are indicative of migration obstacles in the DNA pathway. In view of the absence of significant nanochannel roughness, we hypothesize that the obstacles are created by the short-chain polyvinylpyrrolidone, which was added as an electroosmotic flow suppressor. This polymer would act as a nano-gel structure that could be responsible for the DNA separation.

2.1. Introduction

Deoxyribonucleic acid or DNA is a charged and semiflexible biopolymer built by 4 different monomers called nucleotides (Adenine, Thymine, Guanine and Cytosine), which are linked to a deoxyribose sugar and a phosphate group. These monomers are linked forming a long chain by phosphodiester bounds, which are responsible for the negative charge of the molecule. Such long chains form one strand of a DNA molecule. The bounding of two complementary sequences of nucleotides, by hydrogen bounding, forms a double stranded DNA.

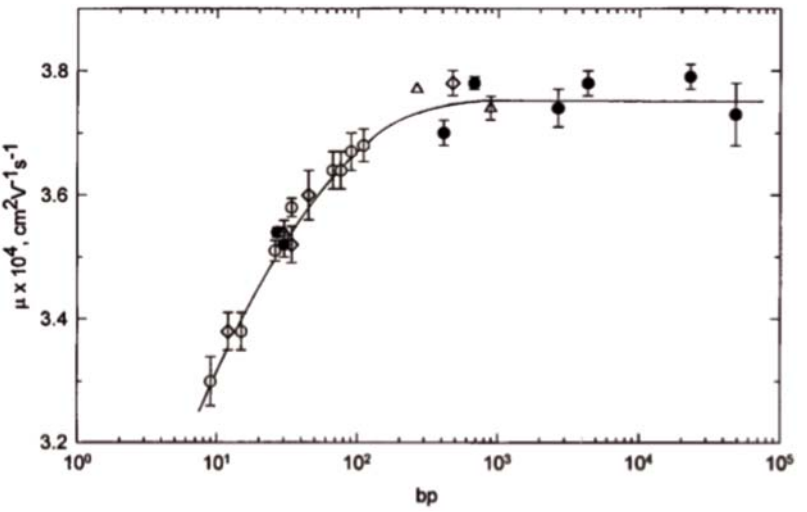

Figure 2.1: Free solution electrophoretic mobility of DNA molecules in TAE buffer (mixture of Tris buffer, acetic acid and EDTA). As it can be clearly seen, the mobility of DNA molecules reaches a plateau phase for sizes around 400 bp, meaning that DNA fragments larger than this size cannot be separated. However, molecules of less than 400 bp can be separated according to their mobility. (2)

In 1964, it was established that the electrophoretic mobility of DNA in free solution was independent of its molecular weight (*1*). This meant that the identification of the molecular weight of a DNA molecule by its charge is impossible. However, in 1997,

Stellwagen reported more accurate DNA mobility measurements carried out by capillary electrophoresis, which demonstrated a dependence of mobility with the molecular weight for small DNA molecules (*2*). Figure 2.1 represents the mobility of monodisperse DNA samples as a function of the molecular weight under TAE buffer conditions (Tris, acetic acid and EDTA). The mobility of molecules containing less than 200 bases increases by increasing its molecular weight. For larger molecules, above 400 bases, it appears a plateau and the mobility becomes independent on the molecular mass. These experiments demonstrate that larger fragments of DNA above 400 bases cannot be distinguished, but shorter molecules can indeed be separated.

2.1.1. DNA separation in free solution

A theoretical treatment often used to describe the DNA mechanics is by a simple elastic model (*3-5*), which defines DNA molecules as a group of Kuhn segments freely joined. Every Kuhn segment contains several monomers. The molecule is formed by N Kuhn segments of length l_{Kuhn}. Thus, the total length of the DNA is $L=N_{Kuhn}l_{Kuhn}$.

When the DNA molecule is in a solution without any confinement we say that the molecule is in free-solution. Under this condition, the DNA chain is presented as self-bended and it is contained in a 3D blob with a spherical shape. This blob can be described by a radius R_g, named radius of gyration, which corresponds to the average dimension of the molecule (see Figure 2.2). This magnitude depends both on the length and stiffness of the molecule. The radius of gyration is given by equation 1:

$$R_g = l_{Kuhn} N_{Kuhn}^{1/2} \qquad \text{Equation 1.}$$

The persistence length (p) is a magnitude that quantifies the semiflexible nature of a DNA molecule and it is considered as one half of a Kuhn segment length (l_{Kuhn}). The persistence length is related to the electrostatic interactions between the charges of the molecule backbone and the free charges of the buffer solution. These electrostatic interactions affect to the segmentation of the molecule and the join between these

segments, thus to the molecule conformation. When the persistence length increases, the molecule stiffness also increases. Consequently, the length of the Kuhn segments increases while its number decreases until a limit in which, the DNA molecule, is considered as a rod.

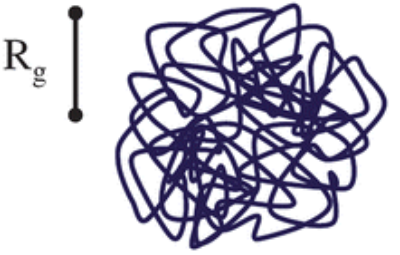

Figure 2.2: The 3D conformation of a DNA molecule in free solution.

The internal electrostatic interactions are produced by the negatively charged phosphate groups on the DNA backbone, which provide electrostatic repulsion among them. Bjerrum length (l_B) (*6*) expresses the length at which such electrostatic interactions are equal to the thermal energy, expressed by Equation 2. At room temperature and in water, the Bjerrum length is larger than the space between the phosphate groups, meaning that internal repulsion forces increase the stiffness of the molecule, since the free movement of the monomers is reduced, causing an effective stretching of the molecule.

$$l_B = \frac{e^2}{4\pi\varepsilon\varepsilon_0 k_B T} \qquad \text{Equation 2.}$$

When the molecule is in a buffer solution, the negative charge on the backbone of the DNA chain attracts the positive free ions of the solution. These positive ions generate a surrounding cloud of ions close to the molecule, with an ion density that decays with a characteristic length called Debye length λ_D.

2.1.1.1. Electrophoresis of DNA

DNA movement under electrophoresis in solution was described by Desruisseaux (*7*), who detailed three regimes. These regimes were defined depending on the relative magnitudes of the persistence length p, the Debye length λ_D, and the radius of gyration R_g and are represented in Figure 2.3. Basically, they define three movement cases and two DNA conformations. The possible conformations are a rigid rod when $p > R_g$, and an elastic fiber when $p < R_g$.

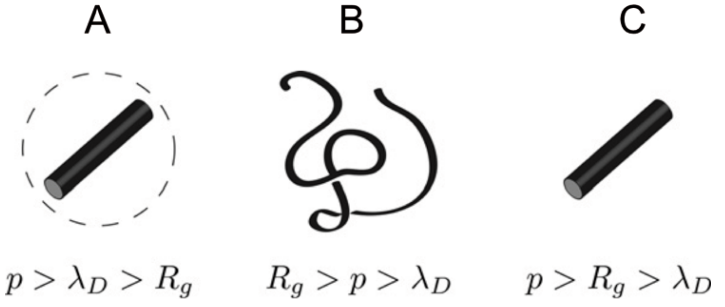

Figure 2.3: Schematic representation of a DNA molecule for different experimental conditions. The three regimes represented are (A) $p>\lambda_D>Rg$; (B) $Rg>\lambda_D>\lambda_D$; and (C) $p>Rg>\lambda_D$. The independent hydrodynamic blob elements of λ_D are represented as pieces of a chain.(7)

When $p>\lambda_D>R_g$ (Figure 2.3(A)), DNA is considered as a rigid rod with a radius of gyration defined by the radius of the sphere generated by projecting its length in all angular directions. In this case, λ_D is represented by a dotted circle around the molecule. It is considered that the ions of the solution are far away and do not interact with the rod. The mobility of the molecule depends on the charge density per Bjerrum length and on the total length of the chain. In these conditions, DNA molecules can be separated in free solution as a function of their length, as Stellwagen demonstrated (*2*).

When the Debye length is smaller than the geometrical magnitudes of the DNA chain ($\lambda_D<R_g$ and $\lambda_D<p$), as in the cases B and C, the ionic cloud of the buffer solution

interacts with the molecule. The largest contribution to the molecule charge is the ionic strength of the buffer solution and the ionic condensation surrounding the molecule (*6*). In these two situations, it is impossible to separate the DNA as a function of its length in free solution, because the molecule mobility depends on the charge density independently of its length.

2.1.1.2. DNA separation by dielectrophoresis. Polarisation of DNA

The DNA molecules in an ionic buffer are surrounded by a counter-ion cloud formed by the condensation of positive ions around them. When the molecule is placed under an electric field, the positive electrode attracts the DNA while the negative electrode attracts the counter-ion cloud. This movement of electric charges generates an effective polarisation of the DNA molecule (Figure 2.4a and Figure 2.4b). The generation of this dipole allows handling the molecule by dielectrophoresis under a non-homogenous electric field.

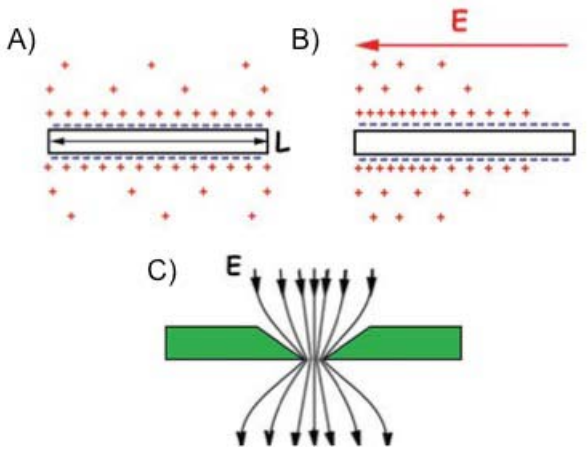

Figure 2.4: Representation of the polarisability of the DNA by the counter ions could, under electric field (a-b). And on the bottom scheme the representation of the modification of the electric field between two fused silica posts, showing the deformation of the field and the presence of a local maximum field (c).(10)

There are some examples of DNA handling by dielectrophoresis (DEP) in literature (*8, 9*). For example, Chou et al. (*10*) have demonstrated the generation of dielectrophoretic traps using a microstructured pattern fabricated in fused silica (Figure 2.4c). In these traps, the electric field was deformed, thus producing a gradient. By using this system, they were able to trap chains of double stranded DNA of 40000 bp applying electric fields of 10^4 V/m. They reported that DEP trapping force increased for longer DNA chains and that double stranded DNA molecules experienced higher forces than single stranded.

2.1.2. DNA separation in gel electrophoresis

In order to separate by size long chains of DNA, gel matrices are used. The idea is to use a friction matrix and, as friction forces depend on the size of the molecules, DNA separation according to its size can be achieved. One of the most common gels used is agarose, a polysaccharide. This gel is appropriate to separate DNA molecules from 100 bp up to tens of kbp. Other possibility is the use of polymers to generate a complex matrix. For instance, polyacrylamide polymer is suitable to separate double and single stranded DNA from 200 to 1000 bp.

Under gel conditions it is possible to define three regimes of DNA molecular separation depending on the relation between the gel pore size (b) and the Rg of the molecule.

Ogston sieving regime ($R_g<b$), where the radius of gyration of the DNA molecule is smaller than the nominal gel pore size. In this case the molecule is travelling through the network without any perturbation of its conformation. Under this premise, Ogston presented in 1958 a DNA separation model that relates the electrophoretic mobility in gel (μ) to the mobility in free solution (μ_0) and the volume available to a molecule of size R_g in a gel of concentration c (*11*). Then, the mobility of the molecule decreases for larger molecules when the volume available decreases.

Entropic trapping regime ($R_g \approx b$), where the radius of gyration is similar size than the gel pore size. In this case the molecule has two possibilities when it is pulled through the gel by the electrical field applied. First, the chain can be stretched and the molecule distributed among several pores. Second, the molecule can be contained in one single pore. In this last case, larger pores will be a preferred place because the less entropy cost. Such pores could act as entropic traps when their entropic trapping energy is lower that the electric field applied. These traps will decrease the mobility in a size-dependent fashion. (*12-14*).

Biased reptation regime ($R_g > b$), where the radius of gyration is larger than the gel pore size. In this case, the DNA is forced to change its free solution conformation and it must uncoil to enter into the pore space. The pore size can accommodate several Kuhn segments, forming a small blob. Figure 2.5 represents a confined molecule in a tube, in which any lateral movement is forbidden. The electric field leads movements to make it leave the tube. Under these conditions the DNA moves like a snake in a tube (reptating) and the electrical force causes preferential motion in the direction of the electrical field (biased). This biased reptation was originally proposed by Lerman and Frisch (*15*) from the Gennes´s concept of reptation in polymer melts (*16*).

2.1.2.1. Biased reptation movement

At this point, we will explain in detail this biased reptation mechanism because of its relevance in the understanding of the movements of DNA confined in a nanochannel. As described before, DNA is assumed to be uncoiled inside the pores of the gel, trapped in a tube formed by this pores, see Figure 2.5. The lateral movement of molecules is hindered and it is assumed that the electric field is weak enough to ensure that the molecule is encapsulated on the tube.

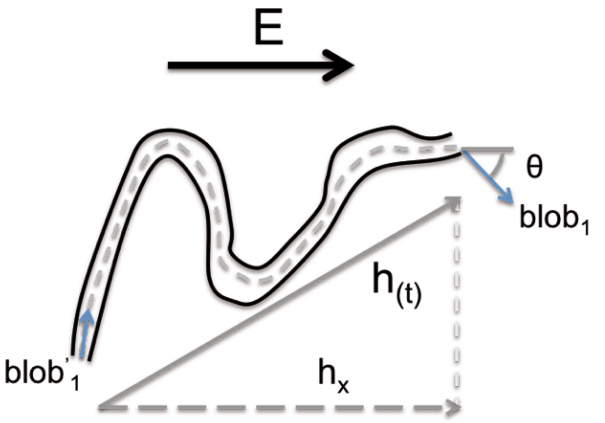

Figure 2.5: The DNA molecule (grey dotted line) is forced to move in a tube fixed by the surrounding gel matrix (solid black line). The chain is modelled by a series of N vector segments blobs. During a forward jump, the final end segment will leave the tube, creating a new blob$_1$ and being replaced by the blob'1 segment. The θ is the angle of this new segment with the filed direction, and $h_{(t)}$ is the effective length of the chain, and h_x is the projection of the segment $h_{(t)}$ on the field direction.

The leakage of the molecule from the tube, forming hernias, will remain improbable as long as the external electrical force (E) is smaller than the entropic force, meaning:

$$\frac{Eq_{blob}b}{K_BT} << 1 \qquad \text{Equation 3.}$$

In this equation q_{blob} is the effective charge of a blob contained in a pore. Following the theoretical development from Slater and Noolandi (*17*), the electrophoretic mobility of the chain is determined by a force balance of each chain blobs, proportional to their charge and to their orientation with the electric field. The total net force acting on the molecule is expressed by equation 4.

$$\sum F_{Bolb} = \frac{QEh_x}{L} \qquad \text{Equation 4.}$$

h_x is the projection of the vector h in the direction of the field (see Figure 2.5), Q is the effective charge of the chain and L is the total length of the chain. This force will drive the molecule with an electrophoretic velocity v_x. Thus, the DNA molecule takes a time ($t=L/v$) to reptate a distance h_x in the field direction. After this time, the conformation of the molecule in the tube can be different. So, the mean electrophoretic velocity and the mean chain mobility (μ) can be expressed as:

$$\langle v_x \rangle = \frac{QE\langle h_x^2 \rangle}{L^2 \xi}; \quad \langle \mu \rangle = \frac{Q\langle h_x^2 \rangle}{L^2 \xi} \qquad \text{Equation 5.}$$

Where ξ is the friction coefficient between the blobs and the gel matrix. In this model, the front end of the segment that leaves the tube aligns itself preferentially with the field direction to minimise its potential energy. Then, the probability that this leaving front end takes a direction with an angle θ with the field direction is low (see Figure 2.5). The average of the angles that the front end can take is related to the Boltzmann constant and to the electrical force experienced. It is given by equation 6.

$$\langle \cos\theta \rangle \approx \frac{Eq_{bolb}b}{6k_BT} \qquad \text{Equation 6.}$$

In summary, the mobility of the molecule depends on the field strength and on its orientation with the electric field, being maximal when the molecule is totally oriented. The angle θ depends on the electric field strength and its average value tends to 0º when the electric field strength increases, thus the molecule tends to be oriented with the electric field.

2.1.3. DNA movement inside nanochannels

When a DNA molecule is travelling along a nanochannel, the molecule will experience conformational and energy difficulties subjected to the force field distribution (*18*). First, the size of the nanochannel creates an entropic barrier for the molecule, which is forced to change its conformation because a large number of 3D conformations become forbidden. This effect leads to mechanical interactions of the molecule with the nanochannel walls as in a gel network. Second, the molecule will be also influenced by its electrostatic interaction with the charged nanochannel surfaces. In general terms, the materials used in micro and nano electrophoresis devices have a relatively strong charge surface. These surface charges generate a counter-ion condensation in a layer with a thickness corresponding to the Debye length, λ_D.

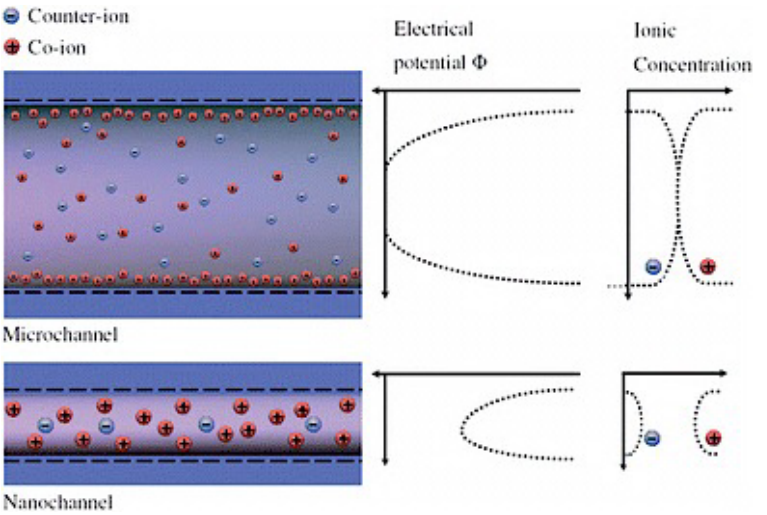

Figure 2.6: Compared evolution of the electric potential between walls for a microchannel and a nanochannel. In a nanochannel the surface to volume ratio is much larger, resulting in a comparable amount of surface and bulk charges. This leads to double layer overlap and a predominant presence of counter ions in the channel.(18)

In microchannels and under the usual electrophoresis buffers, the Debye length (λ_D) is smaller than the characteristic length scale of the channel. However, this relation

changes in nanochannels. By decreasing the size of the channel, the diffuse layers from opposite channel walls can overlap. This is because the surface charge density approaches to the volume charge density on the bulk electrolyte. In this situation, the electric potential does not decay to zero within the nanochannel and there is a predominant presence of positive charges (see Figure 2.6). Under these conditions, the DNA molecule will be repelled by the charged surface and the resulting potential.

2.1.4. DNA separation in nanostructures

Gel separation techniques present some drawbacks to be implemented in miniaturised devices. For instance, it is difficult to fabricate and maintain the matrices in small devices. The advances in the fabrication of micro and nanostructures allow the fabrication of systems inspired on the gel pore structures, capable of performing size-dependent DNA separation. This opens the possibility of doing DNA sequence identification in portable and cheap systems that can be incorporated into diagnostic devices. Excellent reviews in this field are for example those by Viovy (*19*), Slater (*20*), Dorfman (*21*) and Georgette et al. (*18*).

The nanostructured devices for size-dependent separation are inspired in gel pore structures and geometries used in gel electrophoresis. The simplest approach is the use of periodic arrays of thin nanoslits, which connect deep wells. These devices are also called nanofilters, and were reviewed by Han et.al. (*22*). They are normally used to reproduce the Ogston and entropic trap regimes of gel electrophoretic separation. An interesting example of these systems is the device reported by Fu et al. (*23*), that performs the separation of DNA chains between 500 to 5000 bp using nanoslits 73 nm in height connecting wells of 325 nm in depth. Under this geometry, DNA mobility increases with the electric field applied (2 to 7 kV/m) and the transition between the Ogston and entropic sieving regimes is for molecular weights of 1500 bp. They reported different mobility behaviour between both regimes. In the Ogston regime, for molecules shorter than 1500 bp the mobility decreases by increasing the length of the molecules. In this regime for field strengths higher than 6 kV/m, the resolution, related to the mobility differences, decreases. On the other hand, in the entropic regime, the

larger molecules experience higher mobilities and the resolution is better at high fields. However, there is a limit as the mobility of molecules larger than 5000 bp is independent of their molecular weight and only depends of the electric field strength. Then, the filter resolution is limited by the electric field on the Ogston regime, while the length of the molecule in the entropic regime limits the resolution.

Other approach used to mimic the gel porous structure is the fabrication of dense pillar arrays (< 1 μm in diameter, separated 300 nm). This network provides pore dimensions smaller than the radius of gyration of molecule, this means larger than tens of kbp. Ogawa et al. (*24*) reported the movement of large DNA chains through an array of pillars under an electric field of 5 kV/m. The movement of the molecules was described as a reptating movement by cycles of shrinking, stretching and hooking, which lead to molecule separation. This sort of movement is equivalent to one reported in conventional gel experiments (*19, 25, 26*).

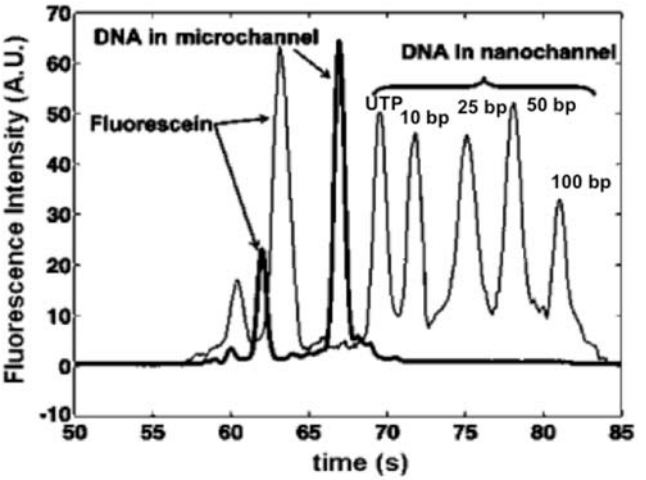

Figure 2.7: Comparison of a free solution separation provided in a 100 nm high channel (thin line) and a 50 μm high microchannel (thick line). A concentration of 10 mM sodium borate buffer and an electric field of 10 kV/m were used. It can be seen that nanochannel provided better resolution over a distance of 20 mm. Figure adapted from (27).

There is still other approach, which consists in reducing dramatically the capillary sections down to the nanoscale. Pennathur et al. (*27*) demonstrated good separation of double stranded DNA molecules with sizes of 10 – 100 bp using nanoslits of 100 nm and 1560 nm in height and electric fields of 100-200 V/m. They compared the results of electrophoresis obtained in nanochannels (100 nm high) with those obtained in microchannels (50 μm high) (Figure 2.7). Four different types of DNA molecules were used: 10, 25, 50, 100 bp, and two fluorescein molecules. In the microchannel the separation was not produced, while in the nanochannel it is possible to detect the peaks corresponding to the five DNA molecules.

Cross et al. (*28*) used the same principle to get gel-free separation of double stranded DNA molecules in nanoslits. Molecule sizes were varied from 2000 bp to 10000 bp. They used smaller channels of 19 nm and 70 nm in height and applied electric fields from 70 to 150 kV/m. They observed an effective size-dependent separation using the 19 nm channel, but no when using the 70 nm nanoslit. Cross et al. and Pennathur et al. related the separation capacity of their nanoslits to the interactions of the DNA molecules with the walls of the nanoslits.

Also by using nanochannels, Salieb-Beugelaar et al. investigated the transport behaviour of λ-DNA (48000 bp) and Litmus DNA (2800 bp) in fused silica nanoslits 20 nm high (*29*). They found that DNA mobility increased with the applied electric field until a threshold value of 40 kV/m. For electric fields below this threshold, the movement of the molecule was described as ″fluent″. On the contrary, for fields higher than the threshold, the mobility of the molecules was strongly reduced by their transient stopping, which produced intermittent movement.

In Salieb´s work, it was proposed that the intermittent movement found for the DNA was related to the field dependence of the mobility. One possibility is that the mobility of the molecule is affected by local variations in the electric field distribution, which could generate dielectrophoretic traps at high electric fields. Another possibility is the

existence of local topographical barriers, which obstruct the travelling of the molecules along the channel.

Pennathur, Cross and Salieb-Beugelaar, attributed the separation capacity of their systems to the small dimensions of the channels, which produced the necessary interaction of the molecule with the channel walls to produce the length separation as in gel mechanisms. They also reported a dependence of the DNA mobility with the applied electric field, which is not well understood.

It is the objective of this chapter to investigate the dependence of DNA mobility with the electric field applied when the molecules are confined in a nanochannel. We investigate the electrokinetic behaviour of λ-DNA molecules in the same system used by Salieb-Beugelaar et al (*29*). In order to determine if the observed phenomena of the DNA trapping in the nanoslits is related to dielectrophoretic phenomena (DEP) we studied the movement of molecule by increasing the dielectrophoresis, under the same electrophoretic conditions used on the Salieb-Beugelaar work (*29*).

Thus, we first evaluate the mechanisms to generate the non-homogeneities necessaries for the DEP phenomena could be created inside of nanoslits with 20 nm in height. And then to prove this possibility, we study the mobility of the molecule using alternating electric fields to increase the dielectrophoretic effects. The idea is that the electrophoretic mobility of the molecule will be lead by the mean value of the signal applied (DC field), while the amplitude of the signal (AC field) will increase the DEP phenomena. As the DEP forces depend on the root main square (E_{rms}) of the field. Thus, if the mean value of the electric field is comparable to the DC field value, the amplitude of the signal (AC field strength) will increase the strength of the DEP trapping and will reduce the DNA mobilities, compared to mobilities obtained when only DC fields were used.

2.2. Materials and Methods

2.2.1. Fabrication of the device

The device used in this chapter was designed and fabricated at the MESA+ institute (Twente University, The Netherlands). The device is composed of two polish fused silica wafers with dimensions of 10 mm per 20 mm (see Figure 2.8). It consists of two microchannels 19 μm high, 300 μm width and 12.5 mm long, connected by an array of 100 nanoslits 20 nm high, 3 μm width and 500 μm long. The nanoslits and the microchanels were manufactured on two distinct polished fused silica wafers. The nanoslits were obtained by standard photolithography and further etching in buffered hydrogen fluoride (BHF) and the microchannels were manufactured in by standard photolithography and wet etching with 0.5% HF solution. The outlet and inlets of the microfluidic system were made by photolithography and powder blasting techniques. Once the nanoslits and the microchannels were fabricated, the two silica wafers were bounded by fusion bonding at 1100ºC.

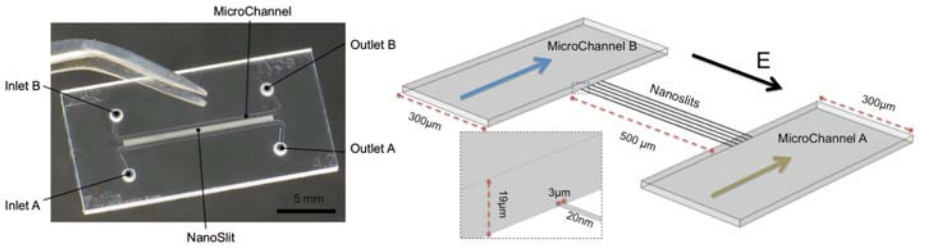

Figure 2.8: Top view of the fused silica device with a schematic scene of the microchannels interconnected by some nanoslits. The dimensions of the nanoslits are 3 μm wide, 500 μm long and 20 nm in height. The green arrow indicates the flow direction of the buffer containing the DNA molecules and the blue arrow indicates the flow direction of the buffer without ADN. The electric field applied forced the molecules to cross the nanoslits from channel A to channel B.

2.2.2. Generation of the electric field

The outlets of both microchannels were connected to reservoirs by silica tubing (Figure 2.9). These reservoirs were used to place two platinum electrodes to generate the electric fields, both in DC and AC. DC fields were applied by a Keithley instrument (Model 2410). The AC fields were applied by connecting a standard function generator (Agilent 33220A) to a high-voltage signal amplifier (Treck 677B), see Figure 2.9. The Treck signal amplifier allows the amplification of the input signal 200 times. When applying AC fields, we used signals with mean values similar to the DC field used. We consider that the system superposes an AC field expressed by the amplitude, to a DC field expressed by the mean value of the signal. The function generator was fixed a 1 kHz frequency. The amplifier was calibrated to correct the deviation generated on the expected DC mean values.

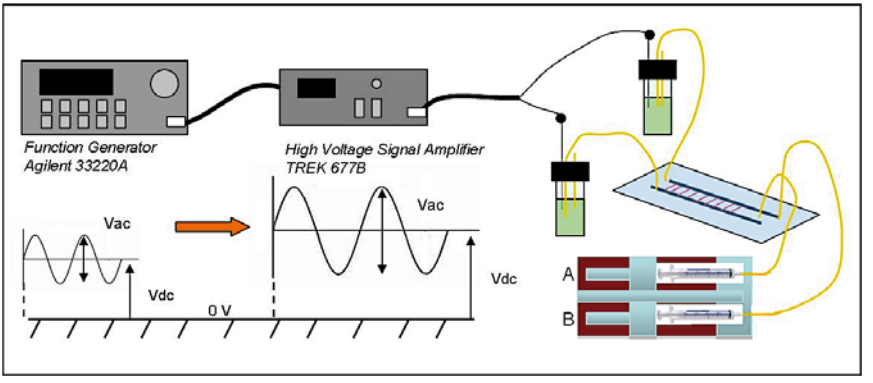

Figure 2.9: The experimental setup, showing the electrical equipment for AC field experiments, connected to the nanoslits device via the electrodes in the waste reservoirs. The two microchannels are connected via capillaries to two syringes driven by independent syringes pumps.

For the DC experiments, we applied electric potentials of 4-100 V, leading to electric fields of 8-200 kV/m. For AC experiments, the signal applied had 4-100 V as mean value and 5-100 V as amplitude. Then, the mean voltages lead to DC electric fields of

8-200 kV/m, and the amplitude voltages lead to AC electric fields of 10-200 kV/m, which are added to the mean value of the field.

2.2.3. Chemicals and reagents

The TBE buffer solution was prepared from Tris (Merck) Boric acid (Panreac) and EDTA (Sigma) solution 1x at pH of 8.3. A dilution of 1x TBE containing 2.5% (w/v) of polyvinylpyrrolidone (PVP; Aldrich) with molecular weight of 10 kDa was used in the experiments. The PVP polymer was used to supress the electroosmotic flow because, as it has a negative charge, it is absorbed by the wall surface neutralising the surface charge of the wall channel.

The DNA used is a non-methylated λ-DNA of 48000 bp (New-England Biolabs), which was labelled with intercalating YOYO-1 dye (Invitrogen) at a ratio of 1:5 (dye : basepair). In TBE buffer, the YOYO-1 dye increases the total length of the λ-DNA from ~16 μm to ~21 μm (*30*). After one hour of incubation at room temperature, the λ-DNA was diluted to a concentration of 400 ng/ml in the buffer solution. Moreover, 3% v/v of β-mercaptoethanol (Sigma) was added to supress photobleaching (*27*). Before the experiments, the buffer solution was degassed in vacuum.

2.2.4. Experimental protocol

Once the DNA solution was loaded in the device it is required to wait at least 10 minutes to ensure that the nanochannels are filled by capillarity. After this time, the λ-DNA was forced into the nanoslits by applying electric fields. We used high DC fields (100 kV/m) to accumulate some molecules inside the nanoslits and then applied the particular electric configuration for each individual experiment.

In AC experiments, we applied 5 superimposed AC amplitudes per DC signal (mean value) applied. The mobility of the molecules was calculated from the velocity obtained by tracking the DNA molecules in lifetime videos. For each electric field configuration (DC and AC), we obtained around 10 videos at different nanoslits. The data used for each configuration was extracted from averaging 10 DNA molecules. At

high DC electric fields, it was very difficult to acquire the movement of DNA molecules, thus the minimum number of molecules studied was reduced to 6.

In order to study the effect of the added amplitude, two different DNA mobilities were distinguished. The mobility calculated from the mean velocity of DNA molecules when crossing the whole nanoslit was named the ″overall″ mobility. Then, we used the velocity between small distances or segments to compute the ″go″ mobility.

2.2.5. Detection Setup

The optical setup consists in a Leica microscope with a 63x objective and Leica L5 filter set, illuminated by a mercury lamp. The acquisition system was a refrigerated camera Andor iXon EMCCD with a sample frame rate of 18,6 Hz. The total acquisition time was around 16-32 s depending on the acquisition area.

ImageJ free software (http://rsbweb.nih.gov/ij/) was used to process and analyse the video files. The velocity of the DNA molecules was calculated using the pixels travelled by the molecule (1 pixel = 0.12 μm) divided by the time consumed. The mobility was then computed from this velocity (v) and the field strength ($\mu = v/E$). In the case of AC fields, the field strength used in this calculation was the mean value of the signal.

2.3. Results and discussion

2.3.1. Simulation of the electric field distribution inside the nanoslit

The surface roughness in the nanoslit was studied by AFM. The characterisation showed a quite rough surface with relatively deep holes and scratches (see Figure 2.10) due to the polishing previous to the fabrication process. Images were acquired in tapping mode with a tip with a nominal radius of 2 nm. The *rms* values obtained from areas 1.6 x 1.6 μm were 1.2±0.4 nm.

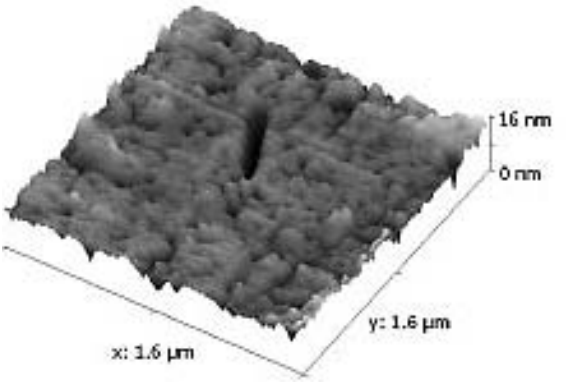

Figure 2.10: Surface topography of the 20 nm nanoslits after the HF etching as measured by AFM. The rms roughness found is 1.2±0.4 nm. There is a scratch in the centre of the scan with a depth of approximately 8 nm.

To determine if this roughness found on the nanoslit surfaces could generate non-homogeneities in the electric field, which are needed to get DEP effects, Multiphysiscs COMSOL software was used to simulate the electric field distribution in the nanoslit. The channel simulated was 200 nm in length and 20 nm in height. In there, it was established an electric field of 12 kV/m. In order to emulate the measured roughness we used ″holes″ at the walls of the channel. To better represent the observed geometry we simulated areas of low and high density of defects. According to the empirical values found, squares of 0.8 and 1.4 nm of depth were considered. Also, a large defect of 8 nm long rifts was included in the model.

Figure 2.11 shows a 2D axial cut of the simulated nanoslit and the resulting electric field distribution. The red lines separate isoelectric field strength regions and give an easy way to understand the effects that the rough valleys could have over the field distribution.

Simulations show that indeed the electric field is non-homogenous. The global and local minima of the electric field are located at all the valleys. Such minimum values are one (≈ 0.8 kV/m) or two orders (≈ 300 V/m) of magnitude smaller than the electric

field applied. Related to these minima, local maxima of values up to 10 kV/m appear at the edges of the valleys. This simulation also shows that the non-homogeneity effects depend on the depth of the surface defects. The field distortion is higher for the deeper holes although it remains confined in regions of some nanometres from the wall surface.

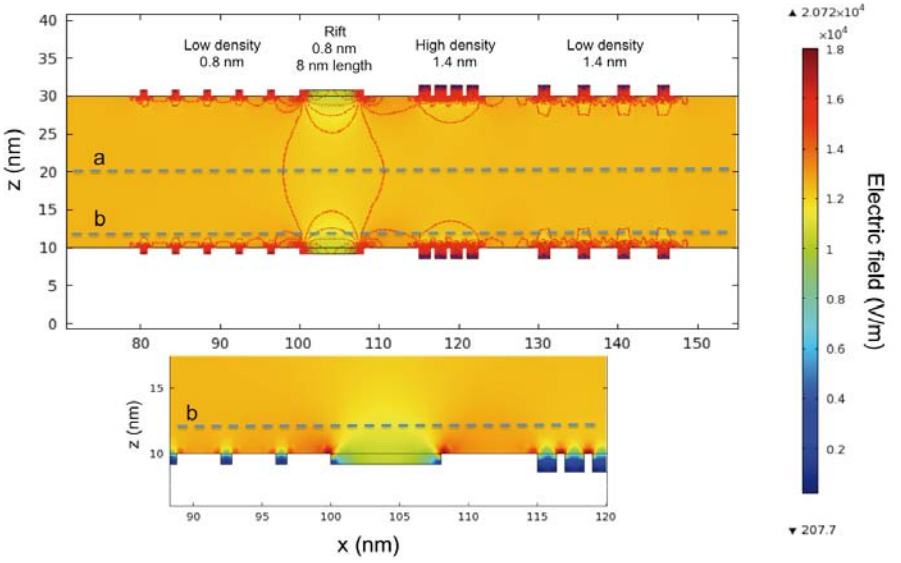

Figure 2.11: Representation of the field distribution on the 2D cut of a nanoslit, where some holes and scratches of 0.8 and 1.4 nm were placed at the channel walls. The colour indicates the local field strength when a 12 kV/m field was applied along the channel. The red line delimited the isoelectric field strength zones. The combined effect of a long scratch could generate a local field gradient at the whole section of the channel, while the small holes represent a local wall field variation. The 1.4 nm holes generate variations on the field at 2-3 nm from the wall. The detail of the wall roughness shows the changes on the electric field. Minimum values appear inside the holes and a maximum at edges.

The simulation also shows that the presence of rift sections (8 nm) makes the electric field change over the channel, because of the change of the effective channel section.

This result implies that long scratches could generate a variation of the electric field that could be experienced by a molecule located at the middle of the channel.

The evolution of the electric field as a function of the channel length (x) is plotted in Figure 2.12. Figure 2.12a presents the evolution of the electric field in the middle of the channel, 10 nm from the wall following line (a) in Figure 2.11. The electric field at this position is highly affected by the rift region. The small roughness represented by valleys of 0.8 nm and 1.4 nm long have very low effects. In Figure 2.12b, it is represented the field variation at 3 nm from the channel wall following the line (b) in Figure 2.11. In this case, the electric field is clearly affected by the roughness, the electric field differences are greater than in case (a) and the changes are more abrupt. At the rift region, in addition to the expected minimum, this defect produces local maxima by the valley borders. In conclusion, the effect of the roughness over the electric field distribution is mainly located close to the walls.

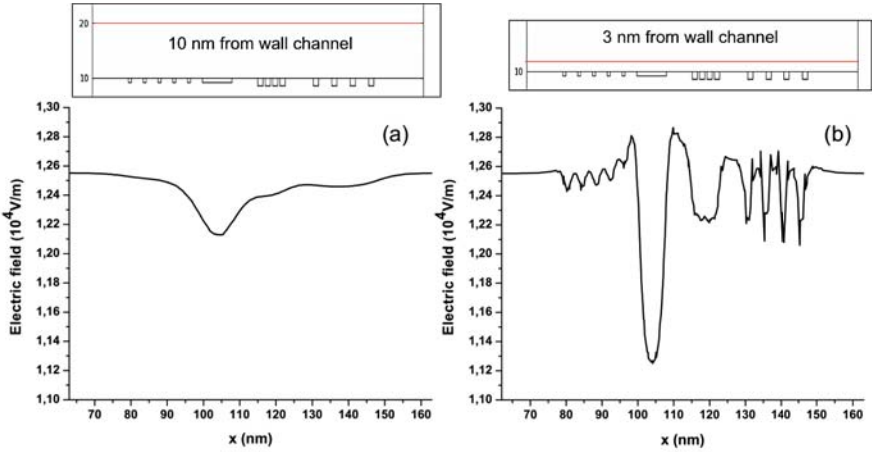

Figure 2.12: Evolution of the electric field strength following the lines (a) and (b) represented at Figure 2.11. It is possible to see how the major contribution to the variation of the electric field is close to the walls, while in the middle of the channel these variations are very low. The combined effect of long scratches could generate an important distortion of the field a long the section channel.

As the trapping phenomena reported for DNA molecules is positive DEP, if existing in the nanoslits, it will be produced at the maxima of the electric field, thus, close to the walls at the long rift regions. Moreover, there is a possibility that the molecule could sense a repulsion force by the minima of the electric field that will produce a velocity reduction or maybe act as a trapping point.

2.3.2. DNA mobility measurements in nanochannels

The movement of λ-DNA nanochannels 20 nm in height under DC electrical fields was described by Salieb-Beugelaar et al. (*29*). Two regimes of movement were identified. When electric fields lower than 20 kV/m were applied, the molecules moved along the nanochannel in a fluent manner with a nearly constant velocity. For electric field values higher than 20 kV/m, the movement of molecules changed drastically to an intermittent stop and go regime, where they become trapped and stopped during certain time lapses.

To investigate if this trapping behaviour could be the consequence of DEP forces due to field distortion created by the roughness of the walls, we used the AC electric field setup. By the addition of an AC field to the system we are increasing the root main square of the electric field (E_{rms}). Then, if the DEP forces are responsible for the trapping behaviour, we expect that for a fix value of DC electric fields (mean value of the signal applied), the λ-DNA molecule mobility will decrease when the amplitude increases.

2.3.2.1. Movement regimes depending on the electric field applied

Figure 2.13 represents the trajectory of a single λ-DNA molecule through the nanoslit when an AC electric field of low strength is applied. The electric signal was composed by a DC mean value of 8 kV/m and by an AC field of 10 kV/m. The channel walls were represented by the blue boxes. The image is a composite of 11 frames stacked together to represent the positions of the molecule along the channel over time. The images show the molecule as a compact point, meaning a bended conformation.

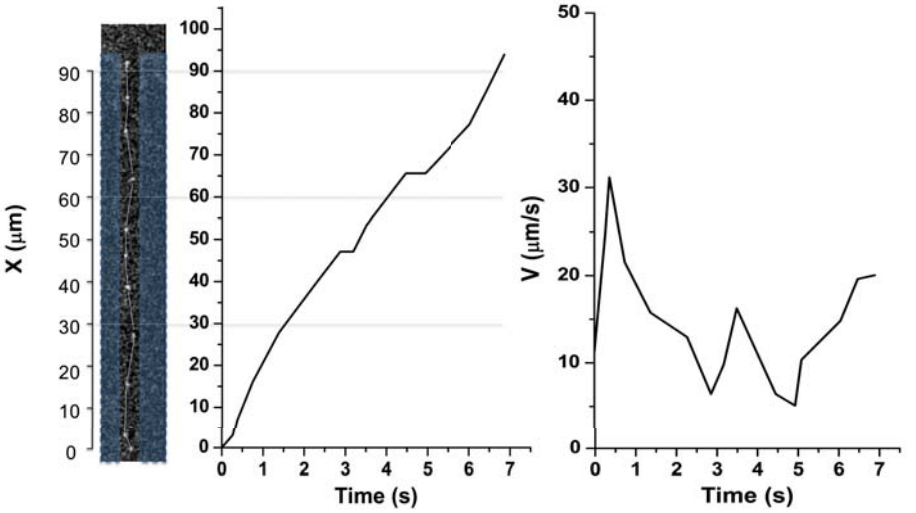

Figure 2.13: Representation of the trajectory of a single λ-DNA molecule under low electric field (DC 8 kV/m and AC 10 kV/m). The image of the molecule movement was build up by coupling 11 frames from a video acquisition. The channel is defined by the blue boxes that represent the fused silica walls. The position and the velocity of the molecule are represented as a function of time.

The movement of the molecule is fluent (Figure 2.13) and the DNA molecules experienced instantaneous variations of their velocity along the nanochannel at specific locations. In particular, velocity values drop considerably between 30 and 45 μm (corresponding to 1 to 3 seconds) and even the molecule is trapped for a short period of time at 45 μm and 65 μm (corresponding to 3 and 5 seconds).

Under these low electric AC fields, it was found that the molecules followed their pathways through the nanoslit in a cycle of shrinking and stretching. An example of this movement is presented in Figure 2.14, where three successive movie frames of a single molecule movement are represented. At t = 0 s (arbitrarily defined), the molecule has a short and compact shape. Then, at t = 0.16 s, the molecule is stretched, which is followed again by shrinking to a compact shape at t = 0.37 s. This

conformation change seems to indicate the presence of physical traps at the nanochannel. This kind of movement is named caterpillar movement, and it was related to entropic sieving[1]. It was observed during DNA electrophoresis in gels (*19, 26*) and in entangled polymers (*25*) when the pore size of the gel is $\approx R_g$ of the molecule. In this case, the molecule is contained in a pore and it moves from one pore to the next one by "jumping" in a coiling-uncoiling movement.

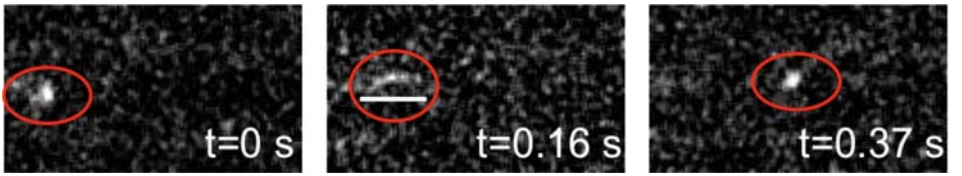

Figure 2.14: Representation of a three sequential frames of a DNA molecule moving from left to right in a nanochannel. The DNA molecule moves in a sequence of stretching and shrinking. The applied electric field was 8 kV/m in DC plus 10 kV/m in AC.

It was also observed that the large majority of DNA molecules followed exactly the same pathways through the nanoslits, indicating the existence of a preferred pathway. Such preferential pathways were detected by superimposing 600 video frames of the data acquired. The integration of the fluorescence signal corresponding of three independent acquisitions is represented in Figure 2.15 (a). These three signals contain around 20 molecules for fluent movement and 10 molecules for intermittent movement. In Figure 2.15 (b), we highlighted the pathways followed by the molecules. The brown dotted line indicates the pathway followed by the majority of molecules (80%), and the grey dotted line indicates alternative pathways. Encircled areas correspond to regions where molecules moved slowly through or even stopping places, in agreement with data plotted in Figure 2.13.

[1] See section 2.1.2. DNA separation in gel electrophoresis

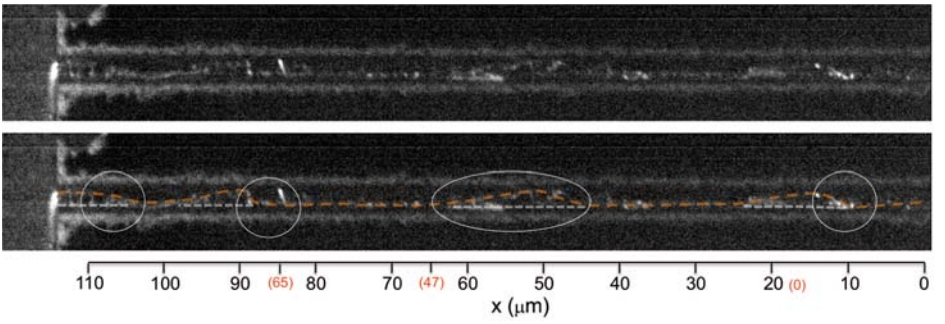

Figure 2.15: The upper view is the image of the sum of the superimposition of the 600 video frames of three independent records. The molecules had drawn their pathways inside the cannel. The bottom view represents the same image with colour lines to follow the preferential pathways. The brown dotted line indicates the main pathway and some alternative pathways are represented by the grey dotted line. The encircled areas indicate the places where the molecules show lower velocities or occasional trapping. Applied field: 8kV/m DC and 10kV/m AC. In the scale bar the red values correlate with the scale bar used in Figure 2.13.

Figure 2.16 shows the movement of a single molecule under high electric fields: 160 kV/m of DC, and 160 kV/m of AC. In this case, the molecule moved at high velocities between specific places, where it remained trapped and stretched for a while. This intermittent movement has peaks of velocity of up to 198 μm/s, while the mean velocity was similar to the one reported in Figure 2.13 (~15 μm/s).

The pathways followed by λ-DNA molecules under such high AC electric fields are plotted in Figure 2.17. Most of the molecules, also in this case, followed the same pathways in their intermittent movement. The stopping places were compared with the encircled areas in Figure 2.15. It was observed that those regions overlapped, indicating that the low velocity areas observed at low AC electric fields become trapping areas at high electric fields.

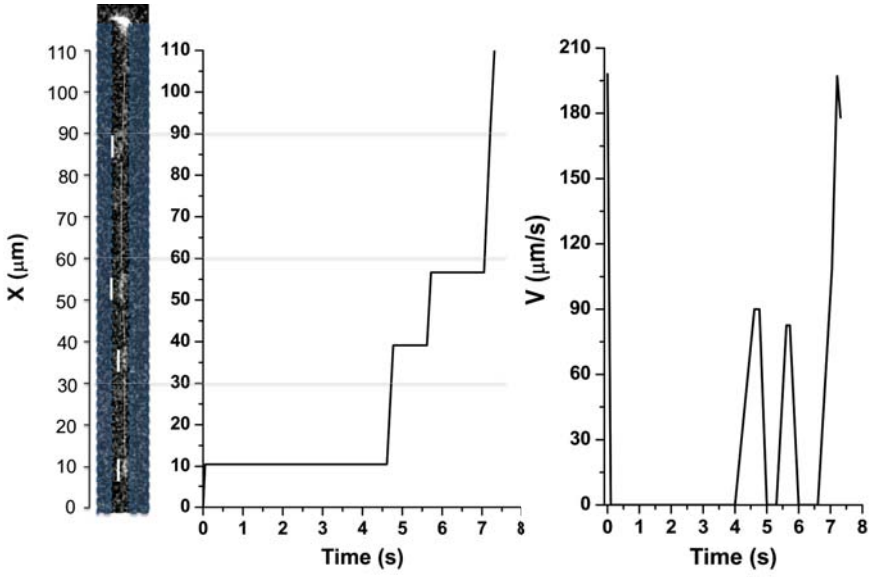

Figure 2.16: Representation of the trajectory of a single λ-DNA molecule under high electric field (DC 160 kV/m and AC 160 kV/m). The image of the molecule movement was build up by coupling 5 frames from a video acquisition. The channel is defined by the blue boxes that represent the fused silica walls. The first plot represents the position of the molecule by the time, where it is possible to see that the molecule experienced three stops. The second plot represents the velocity as function of time.

The results presented in this section indicate that the mobility of DNA molecules inside these nanoslits has a dependence on the electric field strength applied. Two different movement regimes, fluent and intermittent, were identified, which agree with the behaviour presented by Salieb-Beugelaar for DC fields (*29*). Thus, the results obtained with the AC field setup are comparable to those obtained with only DC fields.

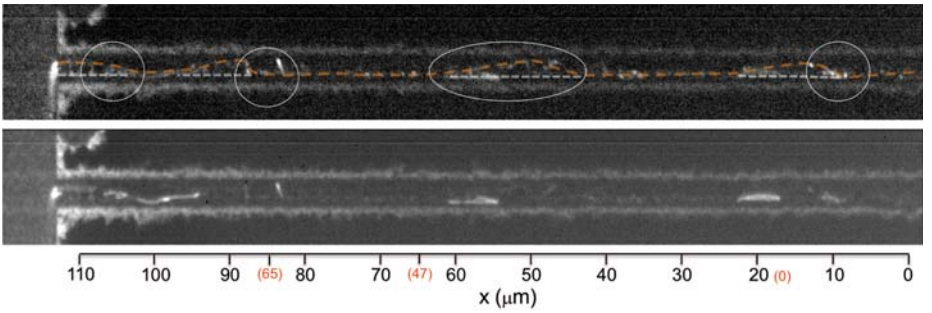

Figure 2.17: Preferential pathways observed after applying high fields, along the previous find preferential pathways, some molecules are trapped. Some of these locations correspond to the encircled areas from the Figure 2.15. In the scale bar the red values correlate with the scale bar used in Figure 2.15.

We also studied the movement of the molecule. Together with fluent movement it was found caterpillar movement. This last kind of movement is related to the entropic sieving behaviour and it also observed in gel electrophoresis experiments, indicating that the effective channel section has local variations. This variation of the effective section seems to be related to physical constrictions, comparable to ″gel-pores″ with relative size similar to R_g, in which the molecule is forced to uncoil to jump between these constrictions.

2.3.2.2. AC fields effect over ″go″ and ″overall″ DNA mobilities

In this section we report the mobility values obtained from applying different AC fields to λ-DNA molecules in the nanochannel. We applied DC fields from 8 to 200 kV/m of mean value and added AC amplitudes from 10 to 200 kV/m. To study the effects of varying the AC amplitude at fixed DC values, we report the "overall" and "go" mobility values (defined in section 2.2.4.).

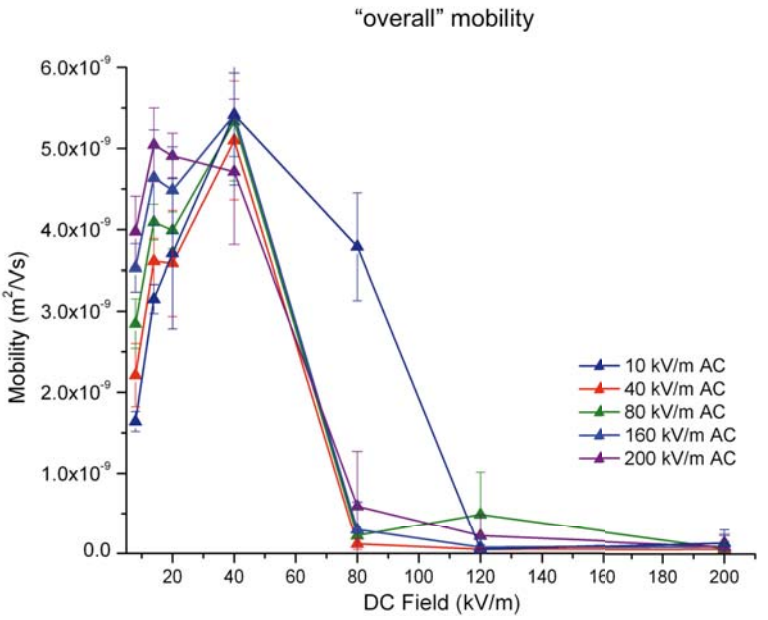

Figure 2.18: λ-DNA "overall" mobility versus the applied DC field at difference amplitudes of AC field (1kHz). The markers represent the means and error bars the standard deviation. The AC fields increase the mobility at DC fields up to 40kV/m. Above 40kV/m DC, the DNA molecules move in a stop-and-go manner with strongly reduced mobility as in the absence of AC fields.

Overall mobility values, calculated supposing a constant velocity for the molecule, are plotted in Figure 2.18. Each dot in the graph represents the mean value obtained for ten DNA molecules per experimental condition, and the error bars indicate the standard deviation. The mobility values obtained depend on the electric field strength. They increase with increasing DC values until a threshold of 40 kV/m. Over this threshold, the mobility abruptly decreases. This is well in agreement with the results presented by Salieb-Beugelaar (*29*), which attributed the changes in mobility to changes from fluent to intermittent movement. The obtained results of ″overall″ mobility behaviour indicate that the DNA mobility in nanoslits is related to the motion regimes (fluent and intermittent) and it is not significantly affected by the AC electric fields.

However, it appears a particular effect of the AC electric field when the molecules move in fluent manner. At DC electric fields below 40 kV/m (fluent regime), the molecule mobility increases with the increasing of the AC field. This effect disappears when high electric fields, over 40 kV/m, were applied. Thus, we perform a statistical study to understand if the effect of the AC amplitude is significant.

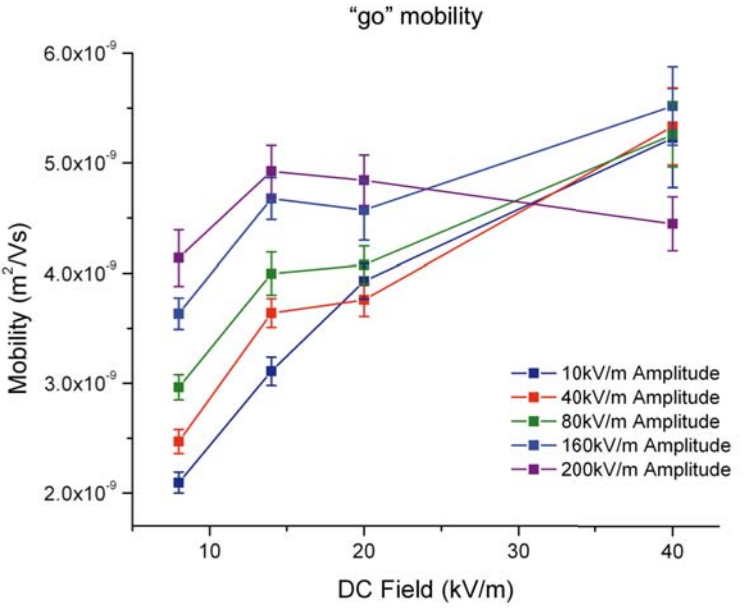

Figure 2.19: λ-DNA "go"mobility versus the applied DC field at difference amplitudes of an added 1kHz AC field. The markers represent the median and error bars the confidence interval, below 40 kV/m. The mobility can be seen to increase with increasing AC field strength. Each data point represents "go"median velocity determinations of 6-12 molecules.

We compared the "go" mobilities obtained for different AC field strengths at several values of DC field strengths. We used the Lilliefors test (*31*) to assess the normality of the mobility populations of each data set, which consist on 30 combinations of AC and DC fields. We found that not all the data set populations fitted into a normal distribution. For that reason, the data sets were compared by Kruskall-Wallis test (*32*),

which is a non-parametric method to compare the medians of two or more distributions. The statistical tests were performed by a MATLAB routine.

Figure 2.19 represents the evolution of "go" mobility median values against DC field strength for different AC amplitudes. In this case, the error bars represent the confidence interval (CI) of the median values, calculated using equation 15.

$$CI = Median \pm (1.58 \frac{IRQ}{\sqrt{n}}) \qquad \text{Equation 15.}$$

Where *IRQ* is the inter-percentile range of the "go" mobility population, which is a coefficient obtained from the difference between the 25th and the 75th percentiles. The *n* is the number of samples. In Figure 2.19 it is observed that in addition of the effect of the DC field value, the mobility of the λ-DNA molecules also increases significantly by increasing amplitude values.

The results of mobility comparison are summarized in Table 1. Chi-squared values obtained from the Kruskall-Wallis test were compared with the critical number of the chi-squared distribution (9.48, p=0.05) using 4 degrees of freedom. It is possible to see that all the values of chi-squared are higher than the critical value, indicating that for the same DC field there are differences in mobility when changing the AC signal amplitude. Only for the highest DC fields (200 kV/m) the significance is lower than the critical value. This table also shows that increasing the amplitude of the electric field increases the mobility of the molecule for all DC electric field strengths.

DC Field strenght (kV/m)	AC field strenght (kV/m) 10	40	80	160	200	Chi-squared
	Mobility: Median (*Standard Deviation*) (10^{-9} m^2/Vs)					
8	**2.09 (0.84)**	**2.47 (0.90)**	**2.96 (0.70)**	**3.63 (0.88)**	**4.13 (1.18)**	**338.1**
14	**3.11 (0.55)**	**3.64 (0.71)**	**3.99 (0.69)**	**4.67 (0.95)**	**4.92 (0.95)**	**164.1**
20	**3.93 (0.79)**	**3.76 (0.78)**	**4.07 (0.62)**	**4.57 (0.98)**	**4.84 (0.87)**	**77.78**
40	**5.23 (0.18)**	**5.33 (1.44)**	**5.26 (1.72)**	**5.52 (1.92)**	**4.45 (1.21)**	**18.6**
160	**3.55 (0.78)**	**0.61 (0.57)**	**0.93 (0.94)**	**0.45 (0.45)**	**0.13 (0.92)**	**28.7**
200	**0.46 (0.75)**	**0.26 (0.37)**	**0.49 (0.73)**	**0.47 (0.61)**	**0.61 (0.65)**	**7.78**

Table 1: In this table are summarised the values of median and the corresponding standard deviation, with the calculated chi-squared value of the distributions for each group of 5 amplitudes added on fixed electrical DC fields obtained from the Kruskall-Wallis test. The critical value for a chi-squared with 4 degrees of freedom is 9.48 for p=0.05. This reference value indicates that for low DC electric fields the 5 populations one for each AC amplitude are significantly different. The difference between populations is reduced with the DC electric field strength until 200 kV/m where the obtained value is less than the reference value.

The combination of the results obtained for "overall" and "go" mobilities suggest that the DNA kinetic-behaviour on the nanoslits does not depend on the homogeneities of the electric field. Our hypothesis, which relates the trapping phenomena with non-homogeneities of the electric field generated by the wall roughness, was tested by adding the AC component to the field, and was found that is in contradiction with the obtained results. Our results show that the AC amplitudes added do not affect the dependence of the ″overall″ mobility of the molecule with the DC field strength. Instead of decreasing it or generate trapping behaviour, it was found that the amplitude of the AC field increased the mobility of the molecule, that show an enriched behaviour of the electrokinetic phenomena of DNA molecules inside the nanochannels.

2.3.3. Comparison with gel electrophoresis

The results obtained under AC fields correlate well with the behaviour reported by Salieb-Beugelaar for only DC fields (*29*), thus a different trapping mechanism seems to be favoured against the dielectrophoresis. The results of trapping and caterpillar movement lead us to think that physical barriers are involved as it was detected a similar behaviour in gel electrophoresis by Äkerman et al. (*26*). In his work, authors related the occasional traps with physical barriers that generate the so called forked positions of the molecules. These forked positions also refer to the presence of physical barriers in which two ends of the same molecule pull in competition (see scheme in Figure 2.20).

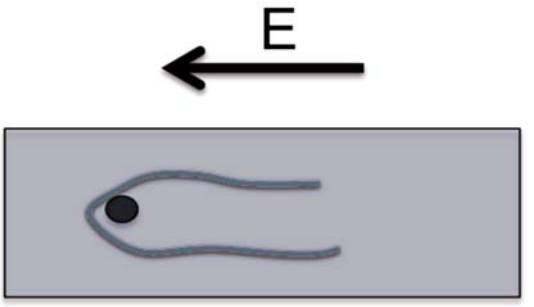

Figure 2.20: Scheme of the forked trapping position of a DNA molecule by a physical object.

A further indication in favour of physical trapping mechanisms in nanochannels is the fact that at high fields the DNA tended to become trapped at the encircled areas, which correspond to sudden, temporal changes at low fields (Figure 2.15). If through the pathway there is a corner or a change in direction, it is possible that the chain could not find the new direction, becoming this place a dead end. Following the reptation model for gel electrophoresis, the higher the angle of change in direction, the lower the probability that the molecules will select this pathway by Brownian motion of the chain.

This observation, therefore, reinforces the physical picture that the DNA encounters an energy landscape in the nanoslits that presents barriers to its movement. Because in the nanoslits the DNA cannot diffuse in the vertical direction, which is much smaller than their persistence length, two-dimensional biased reptations must occur. Caterpillar movement (Figure 2.13) has generally been observed during DNA electrophoresis in gels (*19, 26*) and in entangled polymers (*25*).

In addition, following the biased reptation model for DNA movement, as formulated by Slater and Noolandi (*17*), the stronger the applied field with respect to the thermal movement, the more the tube and the DNA in the tube will be lined up in the direction of the applied field. When, finally, the DNA is entirely aligned, the electrostatic force exerted on the entire DNA chain will contribute to the movement, and mobility will be maximal (*15, 33, 34*). Biased reptation will thus generally yield a mobility that increases with applied field until a maximal velocity is reached, such as the one we observed in the trajectory up to 40 kV/m. In this case, increasing the field strength will reduce the possibility of a change in direction, so the trapping at high applied fields will last longer.

This frequent long-lasting but reversible trapping strongly reduces the measured mobility at high fields as shown in Figure 2.18. Our data thus seem to be consistent with the physical trapping mechanism. Irreversible trapping at high fields in gels has been observed, and is ascribed to the formation of tight knots around gel strands. Reversible long-lasting trapping, however, has only been proposed for artificial matrices. The proposed matrices have local channel constrictions leading to physical trapping, which seems to be the most probable option on our nanoslits

In line with this model we can hypothesize that the addition of AC fields causes additional stretching and alignment of the DNA molecules in the direction of the field, increasing the DNA mobility as it was detected on results presented in section 2.3.2. In Figure 2.21, is presented the distribution of molecules lengths in function of the AC

field applied. These apparent lengths were measured from the video recordings by ImageJ software. The red bars indicate the apparent lengths under AC electric field of 10 kV/m, while orange bars indicate the apparent lengths at 200 kV/m. At high AC electric field, the distribution is larger appearing stretched molecules.

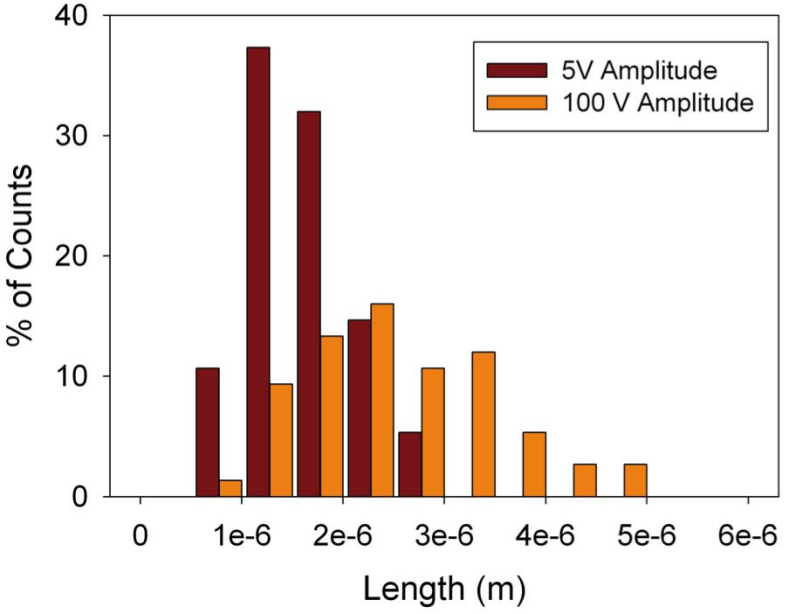

Figure 2.21: Representation of the calculated lengths of λ-DNA molecules under two different AC amplitudes added, 5V (10kV/m) and 100V (200kV/m), to low DC fields. It is possible to see how the higher AC field strength stretches the molecule to a mean value of 2 10^{-6} m and even to a maximum value of 5 10^{-6} m. Under this conditions and following the Biased reputation model this stretching could be the responsible of the increasing velocity effect produced with the AC field addition.

In gel electrophoresis, mobility increase is indeed generally observed when an AC field is added to a DC field in a method called biased sinusoidal field gel electrophoresis (BSFGE) (*35*). In BSFGE the protocol to apply the electric fields is essentially identical to the one we followed here, though the applied field strengths differ. The observations on single DNA molecules in a polymer solution or gel, under the effect of

AC fields, have also shown molecular stretching in the direction of the applied field (*36*). Both observations are consistent with our results that addition of AC fields increases the mobility by stretching the DNA molecules in the field direction.

2.3.4. Polyvinylpyrrolidone (PVP) as nanogel matrix

As shown in Figure 2.10, the silica walls of our nanoslits have a RMS roughness value of 1.2 ±0.4 nm. Because of the results obtained, we believe that this roughness cannot present significant obstacles to the DNA movement. As the roughness is produced by the polishing of the silica wafers, it is characterised by "valleys" instead of "mountains", which could interfere on the molecule movement.

However, the results of our experiments are consistent with the presence of physical barriers within the nanochannel. If these barriers are not coming from the roughness of the nanoslit walls, they might be created by the polyviylpyrrolidone (PVP) polymer, which was added to the solution in a concentration of 2.5% to prevent electroosmotic flow (EOF).

For DNA transport in nanochannels it has been reported the use of PVP 10 kDa in rather high concentrations of 2 to 5% (*28, 37, 38*), or other polymers such us 1% PVP MW 40 kDa or 0.1% POP-6 ('performance optimized polymer') (*39, 40*). Without addition of such polymers it is impossible to determine the mobility of the DNA with some degree of accuracy and is impossible to introduce the DNA molecules into the nanochannels because the electroosmotic flow in fused silica is against the DNA molecule travelling.

PVP is often used in free solution to achieve DNA separation, as the addition of long PVP chains (1 MDa, 2.5 μm in length) can entangle and retard DNA molecules and enable separation (*41, 42*). However, the 10 kDa PVP used in this work has an approximate chain length of only 25 nm. The addition of such short chains cannot cause entanglement, and indeed microchannel DNA separation is not observed even in

7% 10 kDa or 40 kDa PVP solutions (*43*). It is therefore not expected that PVP molecules in solution will create obstacles to DNA motion.

PVP, however, strongly adsorbs to the silica walls of the nanochannels by which it is thought to be why the electroosmotic flow is suppressed (*44, 45*). In nanochannels of 20 nm in height this adsorption can certainly cause local obstruction in view of its molecular length of 25 nm. Since the concentration of 2.5% is much higher than the concentration for saturated adsorption (0.02%), the average PVP layer thickness will be equal to the saturation value for 10 kDa PVP, which is about 4 nm (*41*). The two layers of 4 nm on the opposing channel faces will then reduce the effective channel height to 12 nm. The thickness of 4 nm is however an average thickness, representing the fact that adsorbed polymers partly are in actual contact with the surface in "trains", but also that "tails" and "loops" stick out into the channel and "bridges" may even bridge the nanochannel since the polymer length is larger than the channel height (Figure 2.22).

If a DNA molecule weaves itself through a loop, its local position will be fixed unless it dislodges the adsorbed PVP molecule. The PVP offers a resistance to the movement of the DNA. The attachment force of the PVP molecules adsorbed to the wall, however, is quite large compared to the electrical force on the DNA. From data of Cohen Stuart et al. it can be deduced that the heat of adsorption of a single PVP molecule of MW 10 kDa is $2 \cdot 10^{-19}$ J (*46*). A force of 400 pN is then needed to move this PVP molecule by 0.5 nm out of its bonding, compared to an electrical force exerted on the entire λ-DNA molecule of 750 pN at the maximal field strength of 200 kV/m. Bridges will resist less to being dislocated, since in that case a shorter part of the PVP chain is adsorbed.

In conclusion, the PVP molecules adsorbed in loops and bridges, in combination with the reduction in effective channel height, can in this way present a sufficiently rigid surface-bound gel-like matrix ('nanogel') that impedes the DNA movement and alters its movement direction in a way similar to a macroscopic gel. Indeed, the channel

roughness can be involved on the chaotic distribution of the polymer, which can generate the tails and coil at specific sections.

Figure 2.22: Schematic representation of DNA movement through the proposed "nanogel" formed by the wall-absroved PVP present in trains, loops, tails and bridges. This ultrathin gel presents obstacles to a DNA molecule, moving in under the influence of the electrical field and confined to the gel region by the nanochannel.

2.4. Conclusion

In this chapter we have shown that our results for DNA movement in nanoslits 20 nm in height are compatible with the movement in an obstacle-rich environment very similar to a gel or a concentrated polymer solution.

Both theoretical simulations and experimental results obtained by adding AC fields showed that the hypothesis pointing out to the generation of dielectrophoretic traps by the non-homogeneities of the nanochannel walls is not consistent.

Furthermore, the detection of preferential pathways on the nanoslit, the trapping of DNA molecules at fixed locations at high fields and the coincidence of this places with some direction changes on the 2D preferential pathways lead us to reinforce the physic barriers hypothesis. These effects are consistent with gel electrophoresis models.

It has been proposed that the presence of PVP (10 kDa) molecules in the buffer can reduce the effective height of the channel and cause a local obstruction. This means that PVP is a good candidate to be the responsible of this nanogel through movement.

The present investigation provides strong evidence for a new type of DNA sieving matrix, which is an ultra-thin layer of adsorbed polymer ('nanogel'). The strong bond between the polymer and the silica surface provides the enough rigidity of this gel while the DNA is forced to move through this matrix by the strong confinement of the nanochannel. This separation matrix can be of considerable practical value since its rigidity can be adjusted by the polymer adsorption energy and adsorbed polymer length. Further investigation would be necessary to validate the use of this separation technique.

References:

1. B. M. Olivera, P. Baine, N. Davidson, Electrophoresis of the nucleic acids. *Biopolymers* **2**, 245 (1964).
2. N. C. Stellwagen, C. Gelfi, P. G. Righetti, The free solution mobility of DNA. *Biopolymers* **42**, 687 (1997).
3. D. W. Schaefer, J. F. Joanny, P. Pincus, Dynamics of Semiflexible Polymers in Solution. *Macromolecules* **13**, 1280 (1980).
4. D. E. Smith, T. T. Perkins, S. Chu, Dynamical Scaling of DNA Diffusion Coefficients. *Macromolecules* **29**, 1372 (1996).
5. R. M. Jendrejack, D. C. Schwartz, M. D. Graham, J. J. de Pablo, Effect of confinement on DNA dynamics in microfluidic devices. *The Journal of Chemical Physics* **119**, 1165 (2003).
6. G. S. Manning, Limiting Laws and Counterion Condensation in Polyelectrolyte Solutions I. Colligative Properties. *The Journal of Chemical Physics* **51**, 924 (1969).
7. C. Desruisseaux, D. Long, G. Drouin, G. W. Slater, Electrophoresis of Composite Molecular Objects. 1. Relation between Friction, Charge, and Ionic Strength in Free Solution. *Macromolecules* **34**, 44 (2000).
8. L. Zheng, J. P. Brody, P. J. Burke, Electronic manipulation of DNA, proteins, and nanoparticles for potential circuit assembly. *Biosensors and Bioelectronics* **20**, 606 (2004).
9. J. Regtmeier, T. T. Duong, R. Eichhorn, D. Anselmetti *et al.*, Dielectrophoretic Manipulation of DNA: Separation and Polarizability. *Analytical Chemistry* **79**, 3925 (2007).
10. C.-F. Chou, J. O. Tegenfeldt, O. Bakajin, S. S. Chan *et al.*, Electrodeless Dielectrophoresis of Single- and Double-Stranded DNA. *Biophysical Journal* **83**, 2170 (2002).
11. A. G. Ogston, The spaces in a uniform random suspension of fibres. *Transactions of the Faraday Society* **54**, 1754 (1958).

12. A. Baumgartner, M. Muthukumar, A trapped polymer chain in random porous media. *The Journal of Chemical Physics* **87**, 3082 (1987).
13. M. Muthukumar, A. Baumgaertner, Effects of entropic barriers on polymer dynamics. *Macromolecules* **22**, 1937 (1989).
14. J. Rousseau, G. Drouin, G. W. Slater, Entropic Trapping of DNA During Gel Electrophoresis: Effect of Field Intensity and Gel Concentration. *Physical Review Letters* **79**, 1945 (1997).
15. L. S. Lerman, H. L. Frisch, Why does the electrophoretic mobility of DNA in gels vary with the length of the molecule? *Biopolymers* **21**, 995 (1982).
16. P. G. d. Gennes, Reptation of a Polymer Chain in the Presence of Fixed Obstacles. *The Journal of Chemical Physics* **55**, 572 (1971).
17. G. W. Slater, J. Noolandi, New Biased-Reptation Model For Charged Polymers. *Physical Review Letters* **55**, 1579 (1985).
18. G. B. Salieb-Beugelaar, K. D. Dorfman, A. v. d. Berg, J. C. T. Eijkel, Electrophoretic separation of DNA in gels and nanostructures. *Lab on a Chip* **9**, 2508 (2009).
19. J.-L. Viovy, Electrophoresis of DNA and other polyelectrolytes: Physical mechanisms. *Reviews of Modern Physics* **72**, 813 (2000).
20. G. W. Slater, C. Holm, M. V. Chubynsky, H. W. de Haan *et al.*, Modeling the separation of macromolecules: A review of current computer simulation methods. *Electrophoresis* **30**, 792 (2009).
21. K. D. Dorfman, DNA electrophoresis in microfabricated devices. *Reviews of Modern Physics* **82**, 2903 (2010).
22. J. Han, J. Fu, R. B. Schoch, Molecular sieving using nanofilters: Past, present and future. *Lab on a Chip* **8**, 23 (2008).
23. J. Fu, J. Yoo, J. Han, Molecular Sieving in Periodic Free-Energy Landscapes Created by Patterned Nanofilter Arrays. *Physical Review Letters* **97**, 018103 (2006).
24. R. Ogawa, H. Ogawa, A. Oki, S. Hashioka *et al.*, Fabrication of nano-pillar chips by a plasma etching technique for fast DNA separation. *Thin Solid Films* **515**, 5167 (2007).

25. A. E. Barron, D. S. Soane, H. W. Blanch, Capillary electrophoresis of DNA in uncross-linked polymer solutions. *Journal of Chromatography A* **652**, 3 (1993).

26. B. Åkerman, Cyclic migration of DNA in gels: DNA stretching and electrophoretic mobility. *Electrophoresis* **17**, 1027 (1996).

27. S. Pennathur, F. Baldessari, J. G. Santiago, M. G. Kattah *et al.*, Free-Solution Oligonucleotide Separation in Nanoscale Channels. *Analytical Chemistry* **79**, 8316 (2007).

28. J. D. Cross, E. A. Strychalski, H. G. Craighead, Size-dependent DNA mobility in nanochannels. *Journal of Applied Physics* **102**, 024701 (2007).

29. G. B. Salieb-Beugelaar, J. Teapal, J. v. Nieuwkasteele, D. Wijnperle *et al.*, Field-Dependent DNA Mobility in 20 nm High Nanoslits. *Nano Letters* **8**, 1785 (2008).

30. W. Reisner, J. P. Beech, N. B. Larsen, H. Flyvbjerg *et al.*, Nanoconfinement-Enhanced Conformational Response of Single DNA Molecules to Changes in Ionic Environment. *Physical Review Letters* **99**, 058302 (2007).

31. P. M. H. Abdi, in *Encyclopedia of Measurement and Statistic,* N. J. Salkind, Ed. (Thousand Oaks, CA, 2007), pp. 540-544.

32. W. H. Kruskal, W. A. Wallis, Use of Ranks in One-Criterion Variance Analysis. *Journal of the American Statistical Association* **47**, 583 (1952).

33. O. J. Lumpkin, P. Déjardin, B. H. Zimm, Theory of gel electrophoresis of DNA. *Biopolymers* **24**, 1573 (1985).

34. Gary W. Slater, Steve Guillouzic, Michel G. Gauthier, Jean-François *et al.*, Theory of DNA electrophoresis (sim 1999 -2002 ½). *Electrophoresis* **23**, 3791 (2002).

35. T. Shikata, T. Kotaka, Biased sinusoidal field gel electrophoresis for large DNA separation. *Macromolecules* **24**, 4868 (1991).

36. N. Kaji, M. Ueda, Y. Baba, Molecular Stretching of Long DNA in Agarose Gel Using Alternating Current Electric Fields. *Biophysical Journal* **82**, 335 (2002).

37. C. H. Reccius, J. T. Mannion, J. D. Cross, H. G. Craighead, Compression and Free Expansion of Single DNA Molecules in Nanochannels. *Physical Review Letters* **95**, 268101 (2005).

38. J. T. Mannion, C. H. Reccius, J. D. Cross, H. G. Craighead, Conformational Analysis of Single DNA Molecules Undergoing Entropically Induced Motion in Nanochannels. *Biophysical Journal* **90**, 4538 (2006).

39. C. H. Reccius, S. M. Stavis, J. T. Mannion, L. P. Walker *et al.*, Conformation, Length, and Speed Measurements of Electrodynamically Stretched DNA in Nanochannels. *Biophysical Journal* **95**, 273 (2008).

40. P.-K. Lin, K.-h. Lin, C.-C. Fu, K. C. Lee *et al.*, One-Dimensional Dynamics and Transport of DNA Molecules in a Quasi-Two-Dimensional Nanoslit. *Macromolecules* **42**, 1770 (2009).

41. Q. Gao, E. S. Yeung, A Matrix for DNA Separation: Genotyping and Sequencing Using Poly(vinylpyrrolidone) Solution in Uncoated Capillaries. *Analytical Chemistry* **70**, 1382 (1998).

42. P. O. Ekstrøm, J. Bjørheim, Evaluation of sieving matrices used to separate alleles by cycling temperature capillary electrophoresis. *Electrophoresis* **27**, 1878 (2006).

43. E. Minatti, D. P. Norwood, W. F. Reed, Surfactant/Polymer Assemblies. 2. Polyelectrolyte Properties. *Macromolecules* **31**, 2966 (1998).

44. M. A. Cohen Stuart, G. J. Fleer, B. H. Bijsterbosch, The adsorption of poly(vinyl pyrrolidone) onto silica. I. Adsorbed amount. *Journal of Colloid and Interface Science* **90**, 310 (1982).

45. S. Robinson, P. A. Williams, Inhibition of Protein Adsorption onto Silica by Polyvinylpyrrolidone. *Langmuir* **18**, 8743 (2002/11/01, 2002).

46. M. A. Cohen Stuart, G. J. Fleer, B. H. Bijsterbosch, Adsorption of poly(vinyl pyrrolidone) on silica. II. The fraction of bound segments, measured by a variety of techniques. *Journal of Colloid and Interface Science* **90**, 321 (1982).

Chapter 3 : Handling cells with dielectrophoresis

In this chapter we present a new size-sorting system based on dielectric barriers. Such barriers deform the electric field and create a dielectrophoretic deflection zone. The system uses hydrodynamic focussing to force the sample through the deflection zone. The presented design allow us to use the competition between DEP and dragging forces to separate cells according to their size, under flow conditions.

We first present theoretical simulations to explain how the dielectric barriers induce non-homogeneities in the electric field and thus produce a dielectric effect. The experimental results show the successful separation of latex particles 6 μm and 10 μm in size. Finally, we report the separation studies that warranty the separation between red blood cells and THP-1 cells.

3.1. Introduction

Handling cells is fundamental in many biological and biotechnological assays, such as cell screening, immunoassays, cell phenotyping and diagnostic assays. In the context of point of care (POC) and microfluidic devices, researchers work to scale down these assays. Such miniaturized devices present multiple advantages (i.e., using small volumes of sample and reagents, shorter analysis time...). Point of care systems usually need to perform several and consecutive steps or processes (*1*). These processes can be carried out in additive modules that tackle individual steps such as, for instance, the separation and quantification of cells.

Handling cells inside close set-ups such as microfluidic devices present some challenges, mainly related to the small scale dimensions (*2*). Standard cell manipulation techniques at the micro scale such as micropipettes and micromanipulators are only valid in open environments (*3*). Large centrifuges can process high amounts of sample (cents of mL) while small machines can process over tens of μL. The entire separation process takes about 5-10 minutes. This leads to typical processing sample rates of 100 μL/min when working with standard processes at the macroscale, which is very difficult to accomplish at the microscale.

Systems such as optical or magnetic tweezers allow manipulating cells inside microfluidic devices (*4, 5*) but require highly complex, large and expensive set-ups. Because of that, simpler approaches based on fluidic and pumping tools are an interesting alternative. However, to efficiently separate a specific cell population from the whole sample volume, additional forces are required. In this context, electric forces can be a useful approach because they specifically act over intrinsic properties of cells (*6*).

In the literature, there are many examples of the use of electric forces to distinguish, trap and separate cells (*6-9*). Electrical forces are able to discriminate cells under label free and contactless conditions.

The electrical forces in microfluidic devices can be classified into Electrophoresis (EP) and Dielectroforesis (DEP) as we explained in the introduction chapter. The electrophoresis forces are produced by the Coulomb effect over the net charge of a particle. In the case of cells, this charge is mainly produced by the negatively charged functional groups placed on the membrane (e.g., proteins). This charge is strongly dependent on the pH of the buffer solution. (*10, 11*)

There are some examples of handling cells inside microfluidic devices by electrophoresis under DC fields. For example, Li and Harrison transported RBCs, yeast cells and *E. Coli* using electrophoretic forces combined with electroosmotic flow, inside a commercial "double T" system (*12*). Using this device they could move erythrocytes along of the channel at velocities around 0.1 mm/s under an electric field of 10 kV/m. Ozkan et al. used these electrophoretic forces to develop trapping places in a device that combined electrical traps with optical tweezers (*4*).

Cabrera and co-workers designed a cell deflector, using large electrodes along a microfluidic channel (*13*). In this device, the electrophoretic forces generate the lateral deviation of bacteria by adding a velocity component to the trajectory of the sample flow, which was pressure driven. The bacteria was attracted to the positive electrode and consequently deviated. The system was used to detect differences in the cell charge and characterise changes in the bacteria membrane. They applied 2.6 V DC in a channel 1270 μm wide, meaning an electric field of 2 kV/m and generate an effective sample deviation under a flow rate of 4.8 μL/min (0.22 mm/s).

On the other hand, dielectrophoresis is based on the polarisability behaviour of cells related to the buffer where they are contained. Dielectrophoretic effects can be generated by DC electric fields when it is induced a non-homogeneity in the field. For this purpose, it has been reported the use of isolator barriers or special electrode geometries (*14-18*).

DC systems have, however, one important drawback: the need of using external and big electrodes to generate the high electric fields required. On the contrary, AC systems are easier to establish by microelectrodes embedded in the devices. For instance, coplanar microelectrodes are normally used in dielectrophoretic devices because they can generate the needed non-homogeneities in the field applied. Dielectrophoretic forces have become an interesting tool for micro systems and lab-on-a-chip devices for point of care solutions (POC) (*6, 9, 19*). The devices based in dielectrophoresis that produce effective cell separation under flow conditions can be grouped in two:

- Systems designed to trap target particles at specific places, also known as concentrators. These systems work in two phases, the trapping and the recovery phase. In the trapping phase, the whole sample is flown through the system and then the specific target cell or particle is trapped, so that the sample is filtered. Then, it comes the second phase, the recovery phase. (*20, 21*)

- Systems designed to generate continuous separation of cells. These are the systems in which we are interested. These systems separate a population from a complex sample in a continuous flow. There are many different options to design these systems, but it is essential that the separation is performed in a simple step, reducing the instrumentation setup just to a signal generator.

In 1997, Huang and co-workers presented one of the earliest continuous-flow DEP separation systems (*22*): the field flow fractionation system, known as FFF-DEP. In this system, particles levitate by DEP forces to equilibrium positions that reflect their dielectric properties. Such equilibrium positions are defined by the competition between dielectrophoreic and gravitational forces. Under a parabolic flow profile, different equilibrium positions will provide different velocities to the particles (Figure 3.1). In literature, we find multiple applications of this approach (*19, 23, 24*). Yang and co-workers used this system with two pumps, one as an infusion pump and the other one with a withdrawal setup which collected the sample at the end (*25*) for continuous

separation. They were able to separate T-lymphocites, Granulocytes and Monocytes with flow rates over 0.2 mL/min.

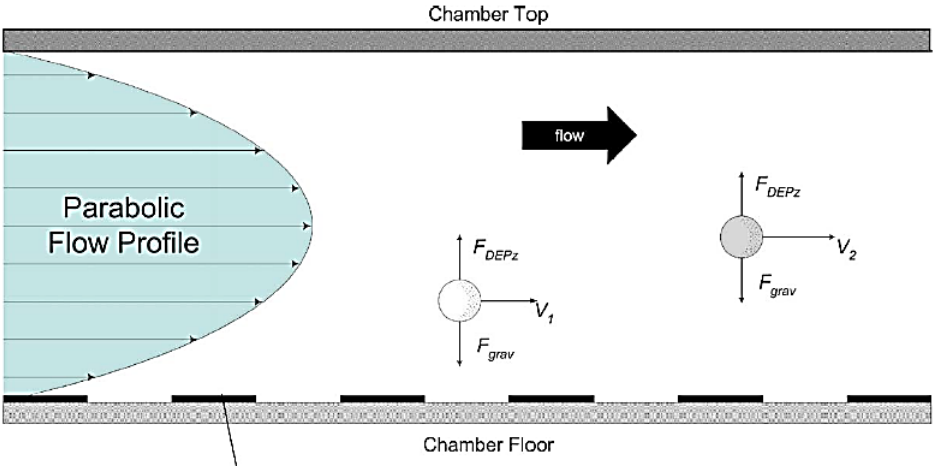

Figure 3.1: Schematic representation of the DEP-FFF principle. An array of electrodes on the lower surface of the channel is used to generate an inhomogeneous electric field. The frequencies and magnitudes of the field produced negative electrophoresis (F_{DEPz}) to force particles to levitate. The electric field strength decrease with the increasing height of the particles above the electrode plane, and dielectrophoresis forces decrease. In addition, a sedimentation force acts on each particle, F_{grav}. Particles are driven to equilibrium heights where the sedimentation and levitation forces are balanced. Different particles with different dielectric properties levitate at different heights, thus in the flow profile they travel along the channel with different velocities V_1 and V_2. Then, the particles are fractionated. (19)

Other option to produce the lateral displacement of cells is the use of electrodes, which are aligned in an angle with respect to the direction of the flow. The combination of the levitation process of FFF-DEP with a lateral displacement allows the local displacement of target particles. The equilibrium height of the cells determines the lateral displacement, which occurs on the edges of the electrode, being stronger for cells that are closer to the electrodes (Figure 3.2).

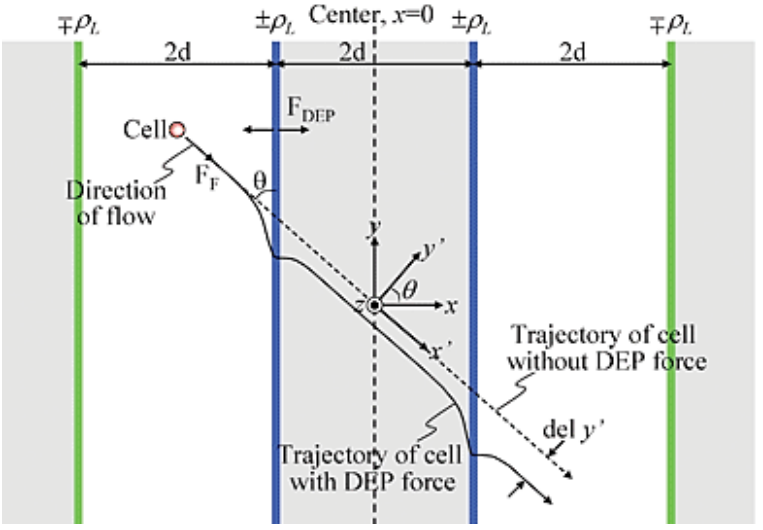

Figure 3.2: Working principle of the lateral-driven continuous DEP microseparator with an interdigitated electrode array. The new force vector acting on a cell has a y'-directional component. As a result, the cell is laterally diverted in the y'-direction (solid line) from its initial trajectory in the x'-direction (dashed line). (26).

In 2007, Cheng and co-workers used a smart distribution of electrodes that integrates different deviation processes to drive cells to specific places (Figure 3.3) (*27*). The system is based on negative DEP and the cells under this condition will be deviated along the electrode length. The pairs of electrodes work at different frequencies, thus, cells that are not in negative DEP conditions will cross the electrode and will conserve their trajectory.

Pommer et al. used a FFF-DEP device with angled electrodes to separate platelets from other cells according to their size, from diluted blood samples. The separation procedure was based on the competition between drag and DEP forces (*28*), allowing the platelet separation in a flow rate of 2.5 μL/min, using an AC electric field of 100 Vpp amplitude. A similar system was used by Kim et al. (*29*) to separate latex beads functionalised with specific antibodies.

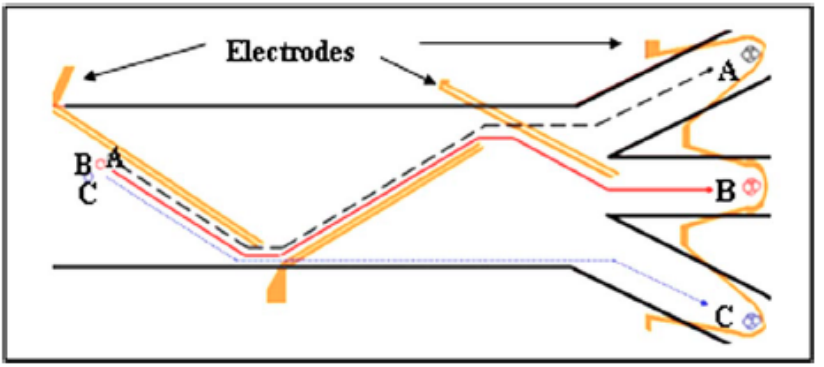

Figure 3.3: Schematic diagram of the sorting electrodes to separate particles A, B and C by negative DEP. The first pair of electrodes deflects all particles. The second pair only deflects A and B, so the particles C cross this electrodes. The third pair only deflects B. (27)

Han and co-workers presented in 2008 a lateral driven device that allows the separation of cells suspended in highly conductive medium working under physiological conditions (*26*). Compared to Pommer's design, the physiological conditions are an advantage because sample preparation is not required. In this case, high electric fields are limited because of high currents and bubble formation but they demonstrated the separation between red blood cells, B and T cells, Granulocytes and Monocytes (*30*).

Vahey and Voldman introduced the isodielectric separation concept (IDS) in 2008. This system combined a lateral displacement by twisted electrodes with a gradient conductivity of the medium(*31, 32*). The relation between the conductivity gradient and the dielectric properties of the cell defines in this case the lateral displacement. With this approach, the particles are deflected by the electrodes under negative DEP conditions, from high conductivity to low conductivity regions, until they reach the isodielectric point. At this point, the DEP force is null and particles are no longer deflected. They accomplished the separation of dead from living yeast cells in a channel 1 mm width and 20 μm height, with sample flow rates of 3 μL/min.

Chang and co-workers (*33*) developed a size separation system by using DEP forces to generate a virtual sieving pillar array following the scheme on Figure 3.4. The virtual pillar array was performed by using angled coplanar electrodes, which, by applying an electric field generate the virtual sieving structure by nDEP. The repletion force of those spots could be treated as the size of the virtual pillars, which is proportional to the particle size. They accomplished the effective separation of red blood cells and white blood cells (of 8.1 μm size), under 0.11 μL/min flow rates, meaning a linear velocity of 0.07 mm/s.

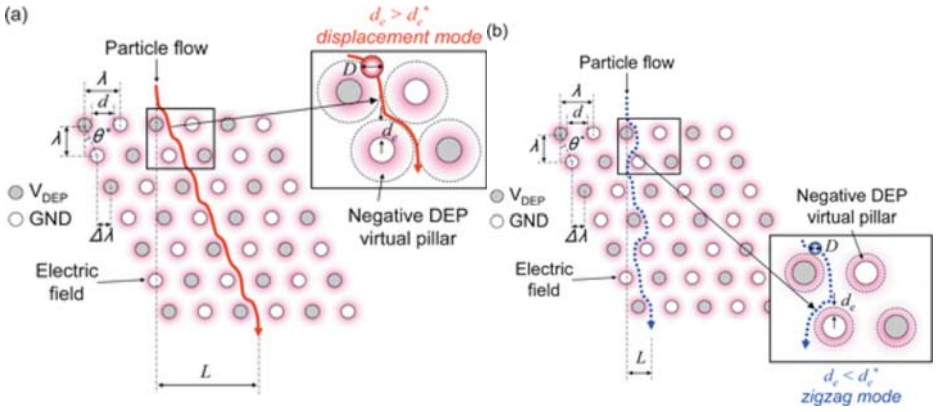

Figure 3.4: The scheme shows the working principle of the virtual pillar array. The DEP force generated by the electrodes is proportional to the cell particle: In case (a) for a big particle, the negative DEP repulse the particle from the pillar generating the lateral displacement of the particle. In (b), for a small particle, the negative DEP is then smaller than in (a), thus the particle experiences a zigzag movement. (33)

In addition to designs based on 2D coplanar electrodes, 3D electrode geometries have been also proposed. Cheng presented a traveling wave (tw) system using two electrode layers, one at the top and another at the bottom of one channel (*34*). Traveling waves use phased electric signals to increase the efficiency of the particle displacement

(Figure 3.5). This system deflects red blood cells in a flow rate of 4 μL/min, which corresponds to a linear velocity of 1.3 mm/s.

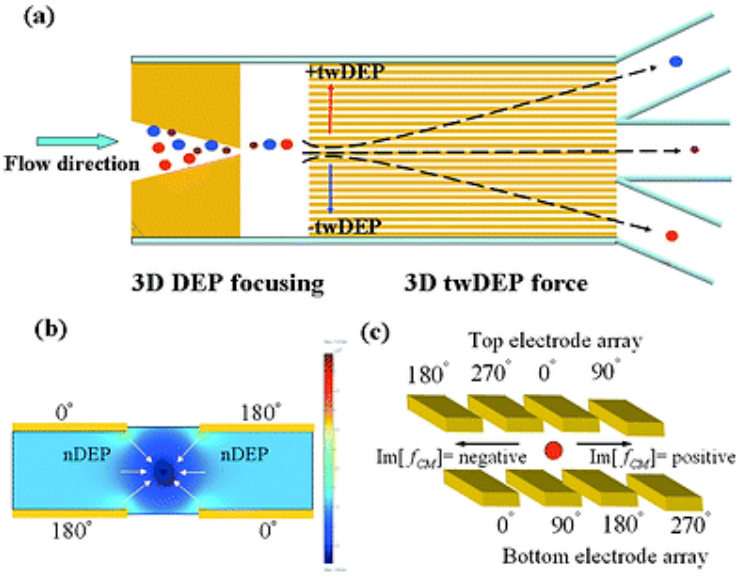

Figure 3.5: Schematic diagram of a 3D electrode design. (a) Top view of electrode structure. Particles experience different directions or velocities of twDEP, which transport them into relative outlets. (b) Side view of electrode structure depicting particles being repelled away from the electrode by nDEP to be focalised and (c) transported in different directions depending on the dielectric properties. (34)

Other microfluidic devices use dielectric features along the channel to deform the electric field and produce non-homogeneities (*6*). A very interesting example of these systems is the device implemented by Demierre, who used the so-called liquid electrode concept (Figure 3.6) (*35*). Braschler and co-workers in 2008 used the same concept in a multi-frequency system. The device was able to sort cells by the competition of two different electric fields applied simultaneously with different frequencies. The particle positions inside the channel were related to their dielectric characteristics. The performance of the system was demonstrated by the separation of a mixed yeast cell population more efficiently than other devices (*31*).

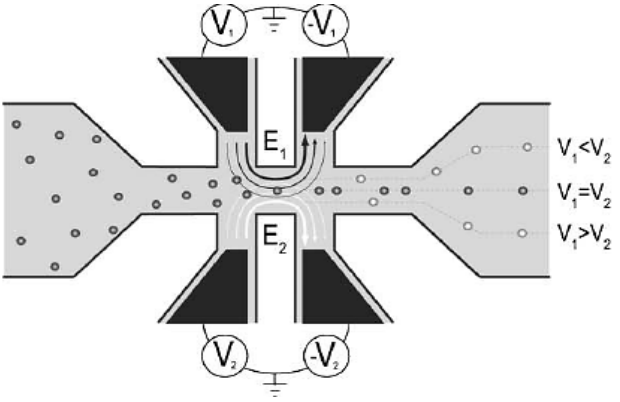

Figure 3.6: The scheme of four liquid electrode structure. The particles (flowing from the left to the right) are deflected by the forces produced by two electric fields, E_1 and E_2. The position of the particles can be shifted in the lateral direction by the adjusting the ratio V_1/V_2. (35)

In all the devices mentioned above, the velocity of the sample limits the particle separation under DEP mechanism in continuous flow, because DEP forces are relatively smaller in comparison with drag forces. In order to decrease the particle velocity in these devices, chips with high cross-section areas have been normally used.

Table 3.1 shows a summary of the geometrical characteristics of the devices presented in this section and the flow rates used. It is worth to notice the great widths used to reduce the sample linear velocity. The maximum linear velocity that could be deflected under physiological conditions was reported as 0.3 mm/s. This was done in a channel 25 mm in width, 0.4 mm in height and 38 cm in length, corresponding to a remarkable flow rate of 200 μL/min. Pommer et al. obtained the best separation performance thanks to the use high voltages (100 Vpp) in low conductivity buffers (*28*) to reduce the electric current. Thus, Pommer´s approach requires sample pre-treatment and high voltage sources, which are not good characteristics for Point of care solutions.

Table 3.1

	Height (µm)	Width (µm)	Length (µm)	Sample velocity	Sample flow	Sample	Force/ Electric potential	Buffer solution
Yang (2000)	420	25000	380000	0.3 mm/s	200 µL/min	T-lymphocite, Granulocytes, Monocyte	FFF – nDEP 4–5 Vpp	Physiological medium ~ 1.6 S/m
Cabrera (2001)	300	1270	40000	0.22 mm/s	4.8 µL/min	Bacteria characterisation	EP 2.6 V	Low condicitvity
Pommer (2008)	20	1750	2 times ~ 6500	6.6 mm/s	2.5 µL/min	Platelets (~2µm) vs RBCs and WBcs	nDEP 100 Vpp	LEC Buffer 50 mS/m
Han (2008)	100	1000	50000	0.1 mm/s	0.83 µL/min	RBCs vs WBCs	nDEP 5 Vpp	Physiological medium ~ 1.6 S/m
Vahey (2008)	20	1000	20000	2.5 mm/s	3 µL/min	Yeast cells	nDEP 20 Vpp	Conductivity gradient < 10 mS/m
Braschler (2008)	20	--	~140	0.9 mm/s	--	Yeast Cells	nDEP/pDEP 4 Vrms	Diluted PBS 60 mS/m
Chang (2008)	14.4	1700	2300	0.07 mm/s	0.11 µL/min	RBCs vs WBCs	Virtual pillar nDEP 10Vrms	Low conducitivity buffer 1 mS/m
Cheng (2009)	25	1000	13000	1.3 mm/s	4 µL/min	RBCs vs Bacteria	tw-DEP / nDEP 12 Vpp	Diluted PBS 1 mS/m
Han (2011)	30	1800	20000	0.3 mm/s	1.2 µL/min	RBCs, T-lymphocite, Granulocytes, Monocyte	nDEP 5.8 V amplitude	Low conductivity buffer 0.17 S/m

Table 3.1: Summary of the geometries used in the devices introduced here: channel section, length of the sorting zone, sample linear velocity and sample volume processed per unit of time. It also includes the type of sample used, the separation mechanism, the electric voltage applied and the buffer conductivities used. The blue boxes indicate 3D electric field performances.

In this chapter we will propose a system to distinguish cells by size under physiological media, meaning high conductivity buffer (~1.6 S/m), in a small device and using 3D barriers inside the channel. Such dielectric barriers will be obtained by using PDMS columns. The system proposed will be tested sorting red blood cells and monocytes (THP-1). The efficiency of the system will be evaluated and compared to those reported in lateral driven systems.

3.2. Theory approach

3.2.1. Shell model of cell

As explained in chapter 1, dielectrophoretic forces are proportional to the Clausius-Mossotti factor (CM), which, taking into account the complex permittivity of spherical particle (ε^*_p), is computed from equation 1. The CM factor takes values from -0.5 to 1 and its sign determines the direction of the dielectrophoresis force: negative (nDEP) or positive (pDEP).

$$K(\omega) = \frac{\varepsilon_p^* - \varepsilon_m^*}{\varepsilon_p^* + 2\varepsilon_m^*} \qquad \text{Equation 1.}$$

Cells are non-homogeneous objects and they can be modelled as multi-shell structured particles. A simple model for eukaryotic cells considers multiple layers that can be associated with the nucleus, the nucleic membrane, the cytoplasm and the cell membrane (Figure 3.7). The interfaces separating the dielectric layers can be described through Maxwell-Wagner relaxation processes.

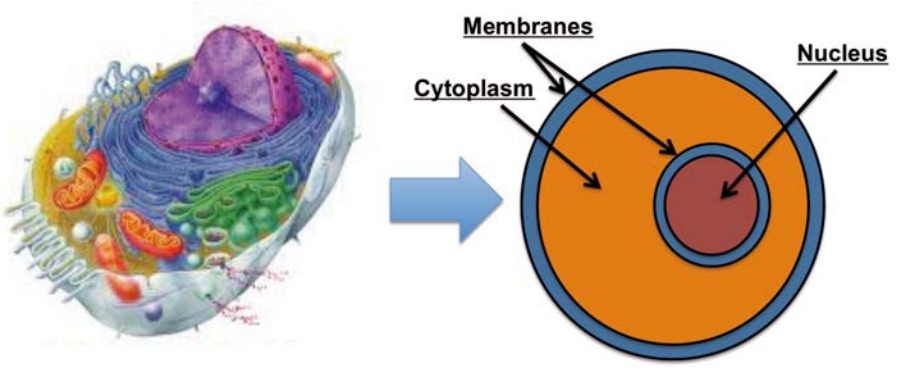

Figure 3.7: Schematic comparison between the structure of a living cell and the simplified model of a multishell structure.

According to the simplified model proposed by Huang et al. in 1992, both nucleated and non-nucleated cells can fit into a simple spherical multi-shell model by defining a complex permittivity (*36*). Following the scheme of Figure 3.8, the cell is represented as an aggrupation of several concentric layers. The complex permittivity for non-nucleated cells (Figure 3.8 left), as red blood cells (RBC), is given by equation 2:

$$\varepsilon_p^* = \varepsilon_{mem}^* \left[\gamma_{1,2}^3 + 2\left(\frac{\varepsilon_{cyt}^* - \varepsilon_{mem}^*}{\varepsilon_{cyt}^* + 2\varepsilon_{mem}^*} \right) \right] \Bigg/ \left[\gamma_{1,2}^3 - \left(\frac{\varepsilon_{cyt}^* - \varepsilon_{mem}^*}{\varepsilon_{cyt}^* + 2\varepsilon_{mem}^*} \right) \right] \qquad \text{Equation 2.}$$

Where $\gamma_{i,j}$ is the relation of the radius of each layer. $\gamma_{1,2} = a_1/a_2$.

In case of nucleated cells (Figure 3.8 right), the model can be extended including the complex permittivity of the cytoplasm (through equation 3),

$$\varepsilon_{cyt}^* = \varepsilon_{cyt}^* \left[\gamma_{2,3}^3 + 2\left(\frac{\varepsilon_{ncl}^* - \varepsilon_{cyt}^*}{\varepsilon_{ncl}^* + 2\varepsilon_{cyt}^*} \right) \right] \Bigg/ \left[\gamma_{2,3}^3 - \left(\frac{\varepsilon_{ncl}^* - \varepsilon_{cyt}^*}{\varepsilon_{ncl}^* + 2\varepsilon_{cyt}^*} \right) \right] \qquad \text{Equation 3.}$$

Where the factor $\gamma_{2,3} = a_2/a_3$.

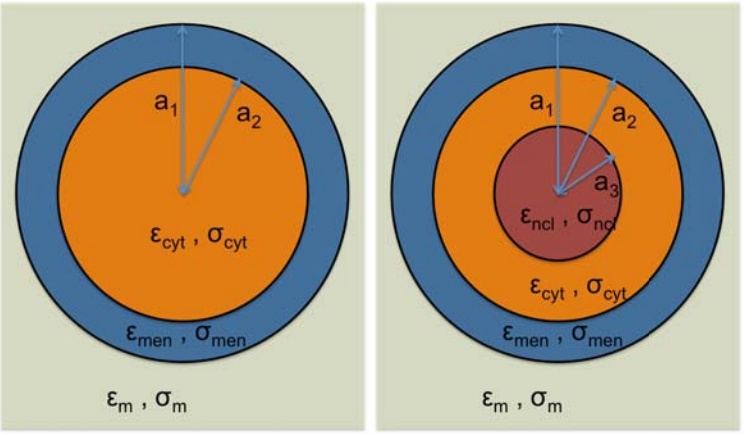

Figure 3.8: Schematic representation of the multishell model for a non-nucleated cell (left) and a nucleated cell (right).

The evolution of CM factor for different medium conductivities was calculated using a MATLAB script. The electrical parameters used were found in the literature (*37*). For the case of non-nucleated cells we used: $\sigma \sim 10^{-8}$ S/m and $\varepsilon \sim 9\varepsilon_0$ F/m for membranes, and $\sigma \sim 0.5$ S/m and $\varepsilon \sim 70\varepsilon_0$ F/m for cytoplasm. The membranes were considered to have 10 nm in width.

Figure 3.9 represents the evolution of the Claussius-Mossotti factor for a RBC. The transitions of the CM factor from positive (pDEP) to negative dielectrophoresis (nDEP) or vice versa mainly account for changes in cell polarisation. Under physiological conditions (i.e., buffer conductivity at 1.5 S/m), the cell is mainly in nDEP regime (Figure 3.9, blue line), whereas under low conductivity buffers, the CM presents two crossover frequencies (Figure 3.9, red and magenta lines).

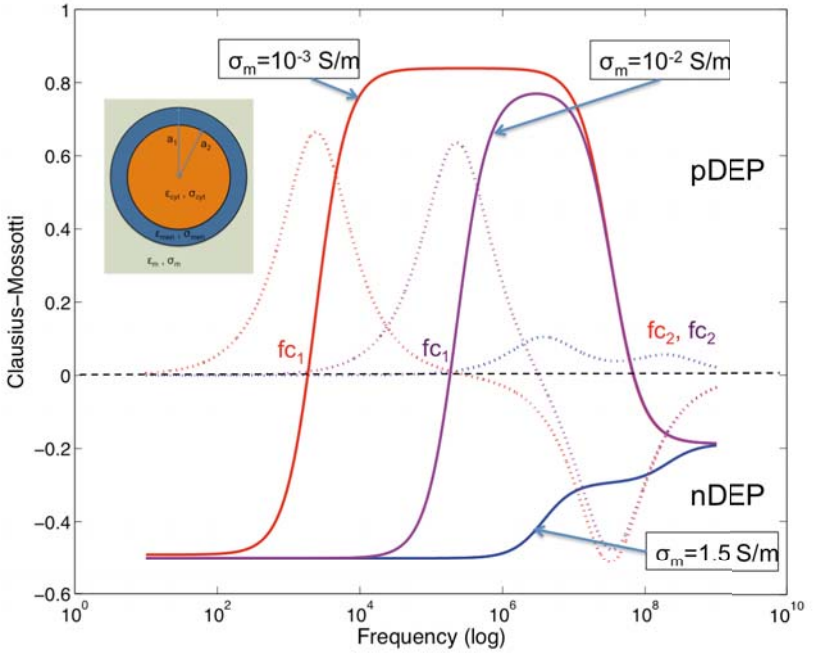

Figure 3.9: Representation of the Claussius Mossotti factor for a non-nucleated cell model. The solid lines represent the variation of the real part of the CM factor, and the dotted lines represent the evolution of the imaginary part of CM. The conductivity of the medium affects to the cutting frequencies that define the sign of the DEP force. The red line, for low conductivity values, show a bandwidth between 10^4Hz to 10^7 Hz where the cell is under positive DEP. Increasing the conductivity of the medium (magenta line) reduces this bandwidth. In high conductivity medium (blue line) the cell is under negative DEP for all frequencies.

Nucleated cells can be modelled using one or two shell layers for the nucleus. To the previous model we included another concentric layer: the nucleus size is considered as the 10% of the cell volume, with parameters σ ~0.1 S/m and ε ~$30\varepsilon_0$ F/m. Some models consider an extra shell for the nucleus membrane, but normally the nucleus is integrated in the same layer. Figure 3.10 shows the differences in the CM factor between a model of two layers for non-nucleated cells and a model of three layers for

nucleated cells. Such differences can be basically found at high frequencies (> 10^6 Hz).

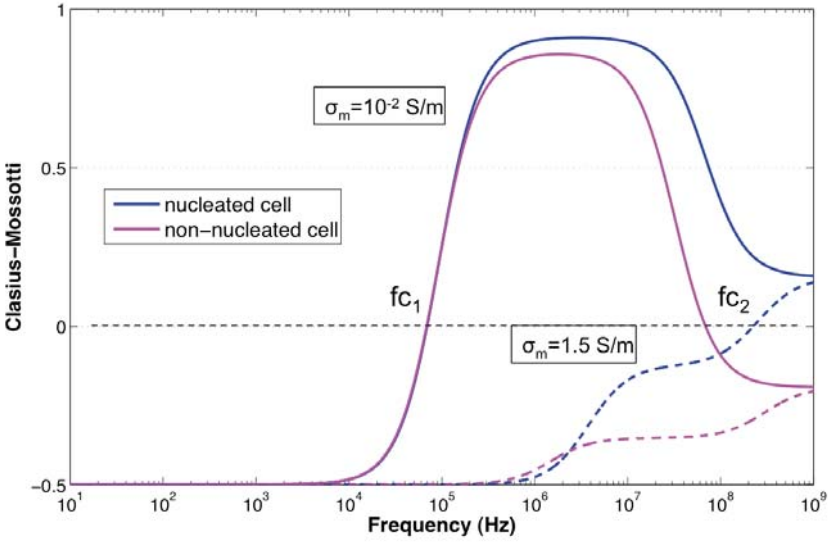

Figure 3.10: Representation of the evolution of the Claussius Mossotti factor, calculated assuming a multi-shell model for a non-nucleated cell (magenta line) and a nucleated cell (blue line). Solid lines indicate values for low conductivity buffers and dotted lines indicate the case of physiological medium.

Typically, cells present two different crossover frequencies:

- The first crossover frequency, f_{c1}, can be found between 10^3 Hz to 10^5 Hz, approximately. It is related with the interaction between the cell membrane and the surrounding medium. Different mechanisms explain this interaction. First, the presence of membrane proteins or other ionisable groups generate a fixed charge on the surface of the particle. Second, the electrical double layer generated around the cell, and the relaxation of the counterions and ionic diffusion related to the polarisability of the cell.

- The second crossover frequency, f_{c2}, is related to the dielectric properties and size of the cell cytoplasm and the nucleus. This crossover frequency is normally detected over 10^7 Hz (*9*).

Thus, the differences between CM factors for nucleated and non-nucleated cells are found in variations in the size of the nucleus, since the cell membrane characteristics are the same in both models.

Typically, there are two approaches to use DEP to separate cell populations. The first one consists on finding the frequency region of the applied field where the two cell populations present opposite signs in the magnitude of Re [$K(\omega)$] factor (*38*). However, when the electrical phenotypes of cell populations are similar, the crossover frequencies are close, meaning that even though the CM factors for both types have different signs, their magnitude is low. This makes the separation difficult.

The second approach uses the differences in the magnitude of the CM factor to find a separation region. For instance, in the example showed in Figure 3.10, the differences in CM between nucleated a non-nucleated model could be significant (e.g., -0.2 in front of -0.4 at 10^7 Hz), meaning that the force is lower for the nucleated cell model. The main limitation of this approach is that differences in size within the same cell population lead to different DEP forces, because their dependence on the particle radius. This dispersion in the force magnitude makes separation difficult when two cell populations have similar dielectric properties. FFF-DEP separation is based on this approach (*22*).

3.2.2. Force balance

Any particle in suspension moving at a velocity in relation to the fluid experiences a resistive force. In the case of small spherical particles moving in a viscous fluid, the drag force is expressed by equation 4, where f is the friction factor, η is the fluid viscosity and a is the radius of the spherical particle. The v is the fluid velocity while u is the particle velocity.

$$F_\eta = f(v-u) = 6\pi\eta a(v-u) \qquad \text{Equation 4.}$$

The DEP force is expressed by equation 5, where ε_m is the dielectric permittivity of the suspension media, and E is the electric field applied. It is important to note that in the drag force the cell radius contribute as a^1, while in the DEP force it contributes as a^3.

$$F_{DEP} = 2\varepsilon_m a^3 \,\mathrm{Re}[K(\omega)]\nabla\left|E\right|^2 \qquad \text{Equation 5.}$$

Then, the cell trajectory and velocity would be defined by the resultant of these two forces acting over the cell.

$$m\frac{du}{dt} = F_{DEP} + F_\eta \,; \quad \frac{du}{dt} + \frac{f}{m}u = \frac{F_{DEP}}{m} + \frac{fv}{m} \qquad \text{Equation 6.}$$

Solving the equation 6, considering a steady state and that the Claussius Mossotti factor is under the best condition for nDEP (-1/2), the particle velocity could be expressed by equation 7.

$$u_p = v - \frac{a^2\varepsilon_m \,\mathrm{Re}\left[CM\right]\nabla\left|E\right|^2}{6\eta} \qquad \text{Equation 7.}$$

Equation 7 expresses the competition between the fluid velocity and the effect of the non-homogeneity of the electric field. Taking into account that the fluid velocity is proportional to the cell radius, the force competition could be understood as a competition between cell velocity and cell size.

3.2.3. Other forces produced by the electric field

The electrokinetic effects generated by coplanar electrode geometries have been reported in several works (*37, 39-41*). In addition to the desired DEP effect, other effects associated to the electrode geometry appear such as AC electro-osmotic and electro-thermal effects.

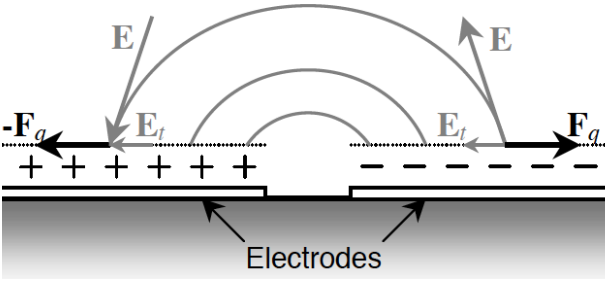

Figure 3.11: Schematic representation of the electro osmotic effect. The use of coplanar electrodes generates an inhomogeneity on the electric field (grey lines). The field distribution gives a tangential component of the field, E_t, near to the electrode surface, where there is a charge accumulation because of the double layer formation. This tangential component generates a charge motion on the electrode surface resulting in a bulk movement (37).

Under the influence of non-uniform AC fields there is a movement of the ion charges accumulated at the diffuse layer on the electrode interface. This is related with the tangential components of the field (see Figure 3.11). This ion movement generates a steady fluid motion on top of the electrodes by electro-osmotic flow (*37, 40, 41*).

At low frequencies the potential across the solution is zero, and at high frequencies the potential across the double layer and the induced charge are both zero. In consequence, the electroosmotic flow is maximal between 10^2 Hz to 10^5 Hz (*40*). The conductivity of the buffer also plays an important role: at high conductivities the diffusive part of the double layer is very thin, and the fluid velocity is very low (*37*).

The electro-osmotic flow will be avoided in our device. First, because we impose working frequencies of the electric field over 10^6 Hz. Second, because we work at high conductivity buffers (physiological conditions).

Another important phenomenon to be considered is the electro-thermal effect. It is produced by the power dissipation when electrical currents are applied. The variation on the temperature produced by Joule heating, mainly around the regions of maximum electric field, induce local variations in the permittivity and conductivity of the fluid generating an electro-thermal force, which produce a fluid motion (*37, 41*).

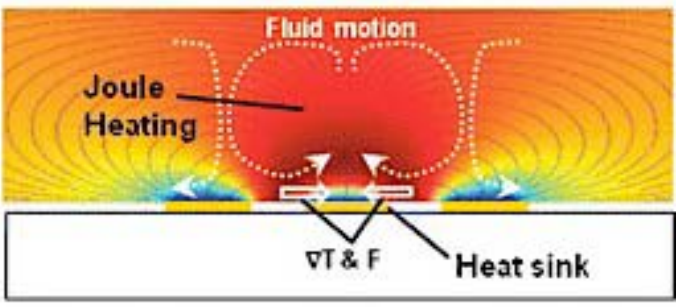

Figure 3.12: Representation of the electrothermal effect over coplanar electrodes (41).

The electro-thermal flow of the fluid at low frequencies normally causes a flow from high permittivity regions (low temperature) to low permittivity regions (high temperature) (*37, 39, 40*). Then, the fluid is directed out across the electrode, generating a convection flow movement, represented in Figure 3.12. In flow conditions, the variation of the local temperature is minimised by the continuous renovation of the fluid.

In general, we will consider that the electrokinetic forces in competition with the DEP force could be minimised by using frequencies over 10^6 Hz and high conductivity

buffers. Then, the drag force is the most important force in competition with the DEP forces in the system.

3.3. Experimental setup

3.3.1. Design of the device

The system design is presented in Figure 3.13. The sorting system consists of two different channels separated by a 30 μm wall. The upper channel is 300 μm in width, and it is the channel where the sample focussing is achieved (blue arrow indicates the sample flow). The bottom channel is 200 μm in width. The combination of the three flow rates warranties that the sample stream will cross totally the intersection zone (blue square), where the dielectric barriers were placed.

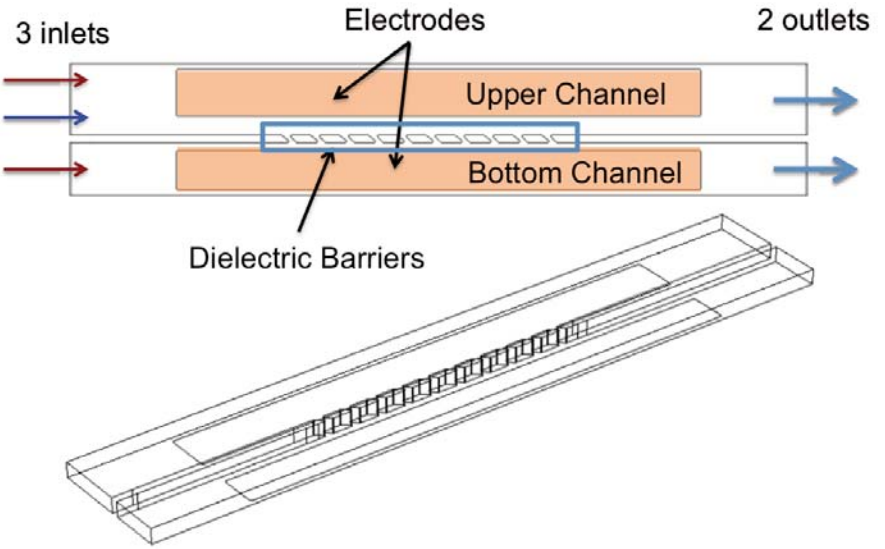

Figure 3.13: Structure designed to develop electrical barrier to deviate the trajectory of the particles in nDEP conditions. Two inlets were placed in the upper channel and one inlet in the bottom channel. The red arrows indicate the streams to focalise the sample across the barriers. The blue arrow indicates the sample inlet. At the end of the system each channel has an independent outlet.

At both sides of the dielectric barriers we placed two electrodes of 100 μm in width, separated 100 μm. The pillars used on the model were trapezoidal with a length 80 μm on its base, and 30 μm wide. The separation between pillars is 25 μm. The structure has 9 pillars, meaning a total length of the separation device of 1 mm.

3.3.2. Fabrication of the device

The microchannels of the microfluidic device were fabricated and developed by standard photolithography at the Nanotechnology platform of the Parc Cientific de Barcelona. The system consists in two layers: one layer with the micro channels fabricated in PDMS and another layer including the electrodes deposited over glass.

To fabricate the moulds for the microchannels, we used the negative photoresist SU-8 50 (microChemicals), which has a nominal thickness of 50 μm at a spin velocity of 2000 rpm. After spinning, solvent evaporation was done using a hotplate at 65º C for 5 minutes and then 20 minutes at 95º C. The UV exposure was performed at an intensity of 21 mW/cm^2. After the exposition, the photoresist was baked again to achieve the cross-linking of the exposed resist. To remove the non cross-linked photoresist we used a commercial SU8 developer solution, during 3 to 6 minutes.

In order to obtain structures with high features, over the limit of 50 μm, we considered two options:

- The first option was to spin the photoresist at lower velocities (i.e., 1500 rpm). Using this approach, we achieved microchannel heights of 60 μm.

- The second option was to spin twice to obtain two layers of photoresists over the glass substrate. The spin velocity was set to 3000 rpm, but we skipped the 10 seconds acceleration step, and the acceleration ramp was increased to 1000 rpm/s. This configuration led to a more aggressive spread cycle and then, the

thickness of each layer can be lower than 40 μm. After the deposition of each layer, the material was baked following the standard protocol in order to evaporate the solvents of both layers. Using this second protocol, heights of 70 μm were achieved.

The obtained SU-8 mould was then covered with Polydimethyl Siloxane (PDMS) (Sylgard 184) in viscous phase, and cured in the oven at 65ºC for 1 hour. The PDMS mixture was prepared by a combination of monomer and cross linker in a 10:1 proportion. After the curing time, the PDMS was de-moulded.

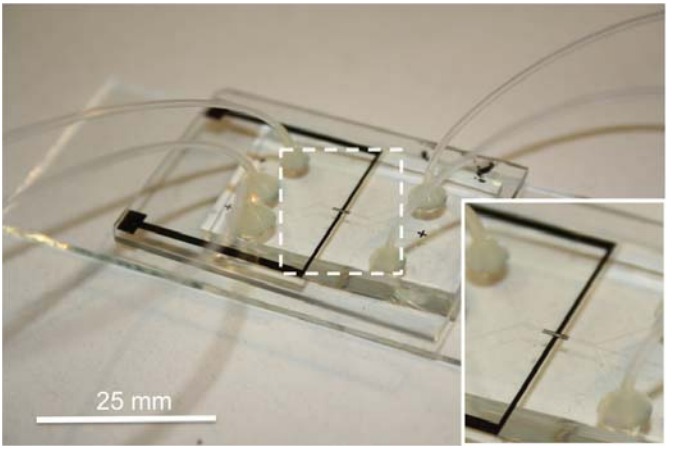

Figure 3.14: Image of the final prototype fabricated. In the upper glass layer, where the electrodes are located, are placed the three inlets and two outlets with their fluidic connections. The PDMS is placed between the two glass layers. The bottom layer is used to facilitate the alignment of the PDMS and the electrode layers. This last glass layer is introduced just for better handling of the device.

The electrodes were fabricated by using a reversal photoresist AZ-5214E. First, we deposited the photoresist at 4000 rpm for 30 seconds on a glass surface, followed by baking in a hotplate at 95º C during two minutes, UV exposure at 21 mW/cm^2 for 2.5 seconds and the post-bake at 120º C for 2 minutes. The resist is inverted by a flood

exposure of light at 28 mW/cm^2 for 10 seconds. Afterwards, a development process is done using a commercial AZ developer during 30 seconds.

The metal deposition was achieved by metal evaporation of 10 nm of titanium, to get good adhesion to the glass surface, and then 80 nm of gold. After deposition, lit-off is done with AZ remover. The PDMS channels and the glass substrate with the electrodes were then bounded by exposition to oxygen plasma. The final prototype used is presented in Figure 3.14.

3.3.3. Materials and methods

We used MilliQ water, from Millipore system, as a low conductivity buffer (0.4 mS/m) to prepare suspensions of latex particles 10 μm and 6 μm in size for the characterization. Then, we used Phosphate buffered saline (PBS) (Sigma-Aldrich,USA) as physiological buffer with high conductivity (1.6 S/m), to prepare suspensions of RBCs and monocytes of cell line THP-1, at concentrations of 10^7 cells/ml and 10^4 cells/ml, respectively. These cells have a mean diameter of 7 μm for RBCs, and 10-12 μm for THP-1.

The continuous flow of the buffers was pressure driven by programmable syringe pumps KDS100 (KDScientific) and, the electric field was generated with a function generator (TABOR Electronics). The electric field applied was a sinusoidal signal of 10 V_{pp} at different frequencies to warranty the nDEP conditions for the different conductivities used. For PBS buffer we used 10^6 Hz, while for low MilliQ water we used $2.5 \cdot 10^7$ Hz.

A Hamamatsu camera was used to track the evolution of the fluids and particles. The camera was fixed to an inverted Olympus IX71 microscope to get quantitative measurements. The separation efficiency was calculated by counting the number of particles deflected from the total particles flown into the barriers for 7 independent experiments.

3.4. Results and discussion

3.4.1. Simulation of the electric field distribution

Figure 3.15 represents the simulated electric field distribution of two coplanar electrodes, where the maximum of the field is located at the edges of the electrodes. The absolute minimum of the field is located at the top of the channel, far away from the electrodes.

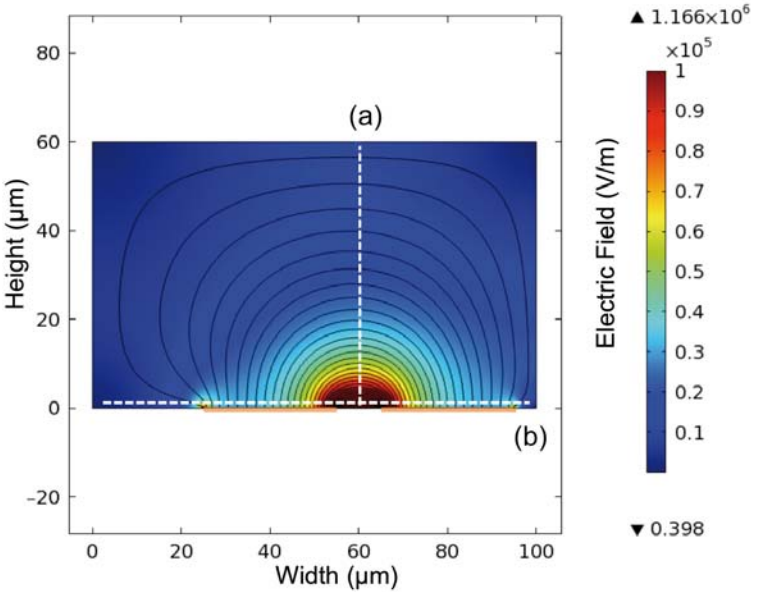

Figure 3.15: Representation of the magnitude distribution of the electric field when a 5V voltage is applied between two pair of electrodes 30 μm wide separated by 10 μm. The maximum of the electric field is placed between the electrodes.

The two plots in Figure 3.16 correspond to the magnitude of the electric field along lines (a) and (b) in Figure 3.15. Figure 3.16a shows the electric field evolution along the height of the channel at the inter-electrode space, which presents an exponential decay from the electrode plane. Figure 3.16b represents the electric field along the

electrodes. We can observe that local minima appear at the plane on the electrodes, at the interspace between the electrodes and in the middle of the electrode surface, while the maxima appear at the edges of the electrodes.

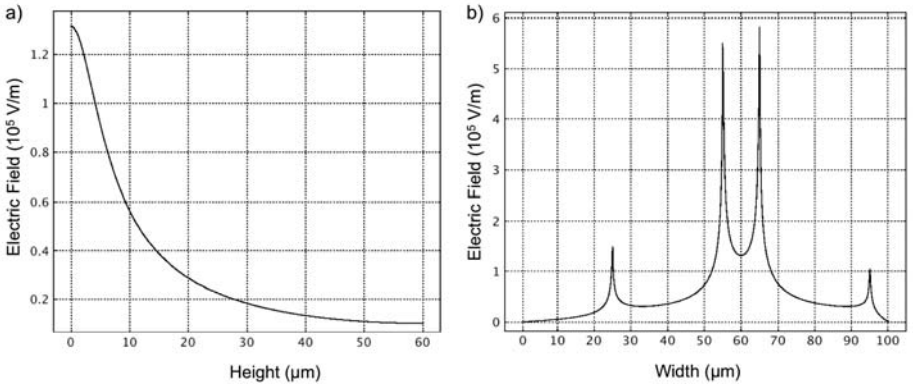

Figure 3.16: Evolution of the electric field strength of the distribution calculated in Figure 3.15 as a function to the height (a) and the lateral axis (b). Close to the electrodes the maximum of the fields were placed on the edges of the electrodes.

It is possible to produce a non-homogeneous electric field in a microfluidic device by using electric barriers (*15-18, 35*). The first advantage of these barriers in front of coplanar electrodes is that barriers produce additional maxima on the electric field distribution, not only at the edge of the electrodes. The second advantage is that this new maxima can be extended along the channel height (Figure 3.17a).

Figure 3.17 shows a simulation of the electric field distribution for ±5 V applied on two coplanar electrodes with and without a dielectric barrier between them. In this simulation the microchannel height is 60 μm and the electrode gap is 100 μm. The electrode dimensions are 10 μm (x) and 60 μm (y). The dielectric barriers were implemented using two columns of 20 μm diameter between the electrodes. In case A (without dielectric barriers) the maxima of electric field are located at the edges of the electrodes and their distribution seems to be homogenous between electrodes. In case B

(with dielectric barriers) a new maximum appears between the columns. This new local maxima of the electric field appears along all the height of the microchannel. This means that the DEP attraction or repulsion effect is also extended along the complete section of the device.

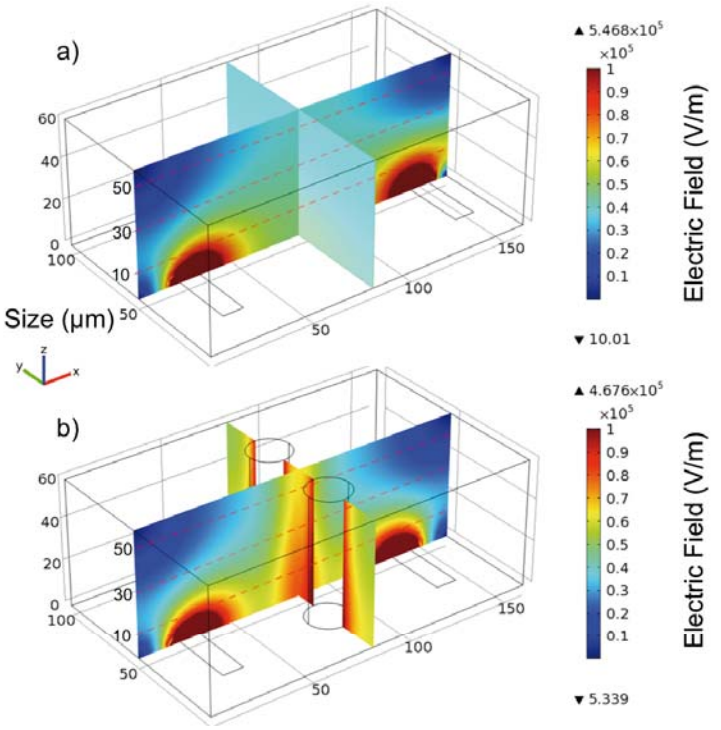

Figure 3.17: Electric field distribution of two electrodes separated 100 μm (a) and the same electrodes with a physical barrier in between (b). In the case (a) the maxima are located at the edges of the electrodes, while in (b) it appears another maximum at the barriers.

Figure 3.18 presents the evolution of the electric field strength at different (z) positions in cases A and B along the red dashed lines of the axial plane (z-x) shown in Figure 3.17. At z=10 μm, the maxima of the electric field are clearly located at the edges of the electrodes (orange stripes) for both cases. In case B, it appears a new maximum between the columns (blue stripes). If we extend this comparison at different heights of

the channel, then we found that the local maximum around the columns is maintained for all the (z) positions.

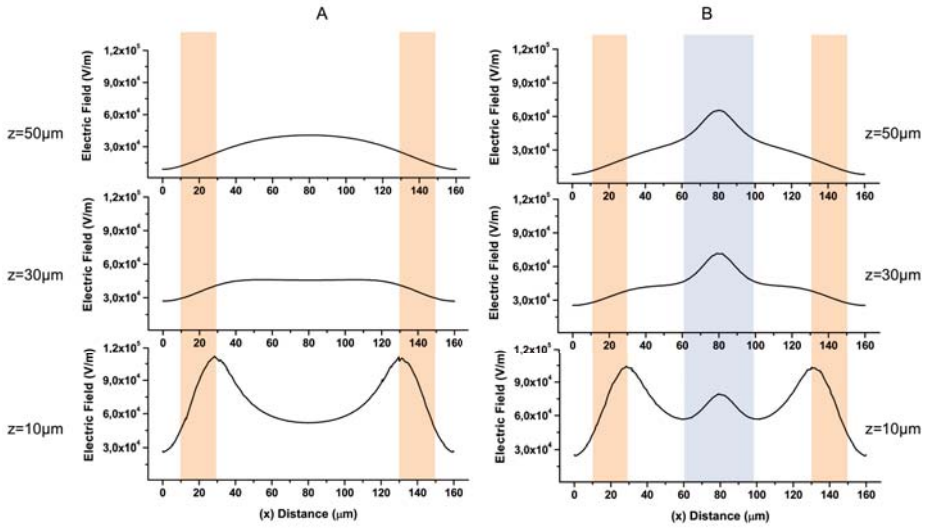

Figure 3.18: Electric field strength at different z positions following the dotted line in Figure 3.17, comparing the case A and case B (with dielectric barriers). The orange colour rectangles represent the position of the electrodes in the 'y' direction and the blue stripes mark the position of the pillar barriers.

Thus, dielectric barriers are a good approach to generate local constrictions in the electric field and, in terms of DEP phenomena, to produce non-homogeneities in the field along the whole section of the microfluidic device. These dielectric traps allow us to use channels over 50 µm in height with the warranty that dielectrophoretic forces will influence all the possible particle trajectories.

3.4.2. Device operation

Figure 3.19 represents the different operation modes of the device. Figure 3.19A shows the effective focalisation of the sample (in blue) by COMSOL simulation. In this simulation the velocity considered for the upper focussing flow is 10 times bigger than the other flow rates (sample and bottom focussing flow), which are set at 1 mm/s.

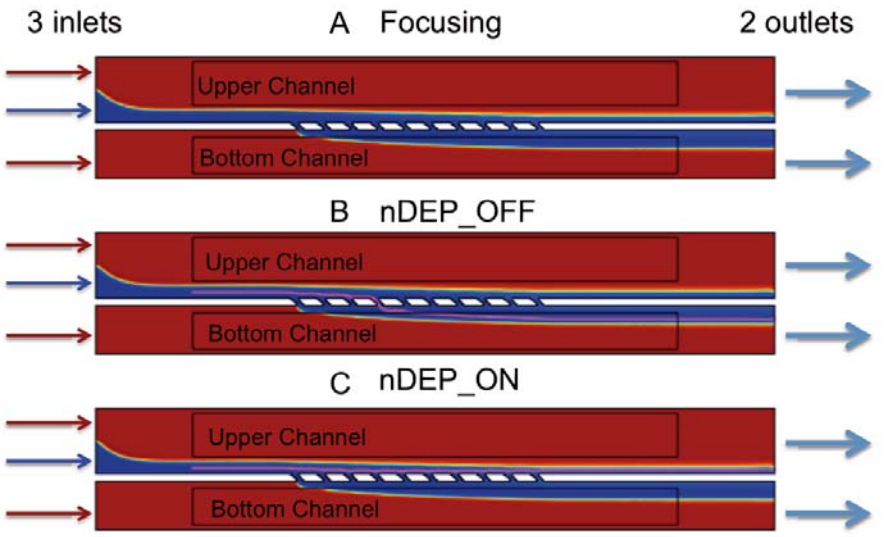

Figure 3.19: Representation of the 2D simulations of the working process of the system designed. The fluid focussing forces the sample stream to move from the upper channel to the bottom channel across the pillar array (A). At the same fluid conditions and the electric field turned off (nDEP_OFF) the trajectory of a 2 μm particle is shown in magenta (B). The particle will cross the pillar array to the bottom channel. When the electric field is applied (C), the pillar array becomes an electric barrier, the trajectory of the particle is deviated and it remains in the upper cannel.

To demonstrate the effect of the DEP forces in the device, we simulated the trajectory of a small particle of 2 μm radius, shown in Figure 3.19 (B and C) by a magenta line, overlapped to the focalisation. In Figure 3.19B (nDEP_OFF), the particle trajectory is only influenced by the drag force and follows the flow direction of the blue stream, travelling to the bottom outlet at a velocity equal to that of the fluid Equation 7).

When the electric field is activated, Figure 3.19C (nDEP_ON), the DEP force competes with the drag force. The DEP effect was simulated by calculating the electric field distribution $\nabla|E|^2$ ($\nabla E \cdot E = 2 \cdot (E \cdot \nabla E)$) after applying a voltage of $\pm 10/\sqrt{2}$ V between the two electrodes. The DEP force was calculated considering a CM factor of -0.5 (i.e.,

nDEP regime). In this case, the pillars generate an electric barrier under nDEP conditions, which blocks the flow of particles from the upper channel to the bottom channel. Thus, the particles remain in the upper channel.

Considering the cell model described in section 3.2.1, we could use the differences in the CM factor between non-nucleated and nucleated cells to separate RBCs from Monocytes. At 10^7 Hz, CM factor takes the value of 0.45 for non-nucleated and 0.2 for nucleated cells. However, it does not mean that the DEP force is lower for THP-1 cells, because the dielectric forces have an stronger dependence (power of 2) on the particle size than CM factor. In fact, DEP forces will be higher for THP-1 cells.

3.4.3. Fluidic characterisation

The particle deflection requires the sample stream to flow along the two main channels and through the pillar separation region. To this end, we used two focussing flow streams to focalise the sample stream near the pillars. In order to demonstrate that the fluidic system works as expected and the pillars do not disturb the normal behaviour of the fluidic system, a fluidic characterisation was performed without any electric field applied.

We injected coloured ink through the sample inlet. Figure 3.20 shows a picture of the distribution of the coloured fluid (sample) in the system for several flow rate configurations. The width of the sample stream can be calculated according equation 8 (*42*):

$$w_s = w_{ch} \frac{Q_s}{Q_{f1} + Q_s + Q_{f2}} \qquad \text{Equation 8.}$$

where the w_s is the section of the sample stream in a channel of width $w_{ch,}$, Q_s is the flow rate of the sample stream, Q_{f1} is the flow rate of the upper focalisation stream and Q_{f2} is the bottom focalisation stream. In the experimental procedure Q_s and Q_{f2} were fixed at the same velocity.

Figure 3.20a, shows the distribution of the three streams using the same flow rate in the three inlets (e.g., $Q_s = Q_{f2} = Q_{f1} = 6$ μL/min). The three streams occupy approximately 1/3 of the total section of the channel. Thus, at the end of the intersection zone, where the two channels become independent again, the blue liquid is equally distributed in both outlet channels.

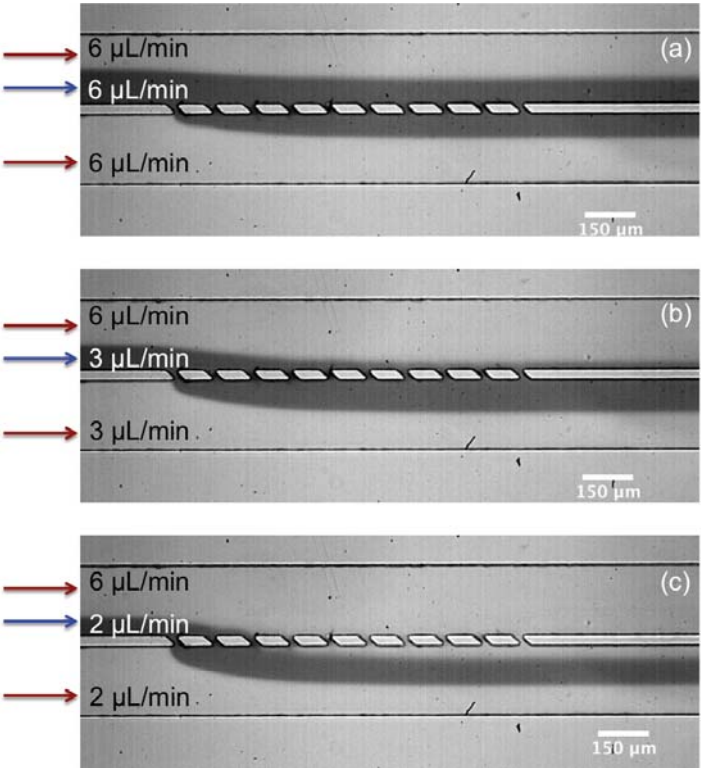

Figure 3.20: Images of the distribution of the three inlets at the intersection of the upper and bottom channel through the pillar array under different flow rate conditions. When the three inlets have the same flow rate (a), the distribution of the three streams is equal along the 400 μm wide channel (the sample stream in colour is divided in two equal parts at the outlet). In case (b), the sample flow and the bottom focalisation stream together are equal to the upper focussing flow rate, and the sample stream crosses the pillar structure. In the case (c) the upper focussing rate crosses the pillar structure, because is greater than the sample flow and the bottom focussing rate together.

In Figure 3.20b the flow rates follow the condition of $Q_s+Q_{f2}=Q_{f1}$ and the width of the blue ink is 1/4 of the total section of the channel, meaning that the Q_s remains at the bottom outlet channel after the intersection. This case allows the sample stream to cross the pillars. Whenever the ratio between Q_{f1} and $Q_{f2}+Q_s$ is bigger than a factor two, then the sample stream will always switch to the bottom channel after the pillar region, as shown in Figure 3.20c.

The dielectric barriers do not affect the normal focalisation of the streams, which only depends on the total section of both channels, w_{ch}, expressed by the equation 8. Thus, this equation was used to calculate the flow conditions for systems in devices with non-symmetric channels.

3.4.3. Separation by size using latex beads

We first tested the separation system using latex beads of different sizes. We used latex particles of 10 μm and 6 μm in diameter (Polyscience Inc,), and a device with an upper channel of 300 μm in width and a bottom channel 200 μm in width. The total height of the channel was 50 μm.

Latex particles were diluted in MilliQ water with a measured conductivity of 0.4 mS/m. Under this buffer, latex beads were in nDEP for frequencies above 10^5 Hz. The electric field frequency was fixed at $2.5\cdot10^7$ Hz to avoid electro-osmotic effects. The fluidic conditions were 0.6 μL/min both for the sample and the secondary focussing stream. The primary or upper focussing stream flow rate was 0.8 μL/min. Under those fluidic conditions a fraction of the sample stream remains at the top channel, even after the pillar intersection region. These flow rates were translated into a particle linear velocity of 1.3 mm/s. The separation results are represented in Figure 3.21.

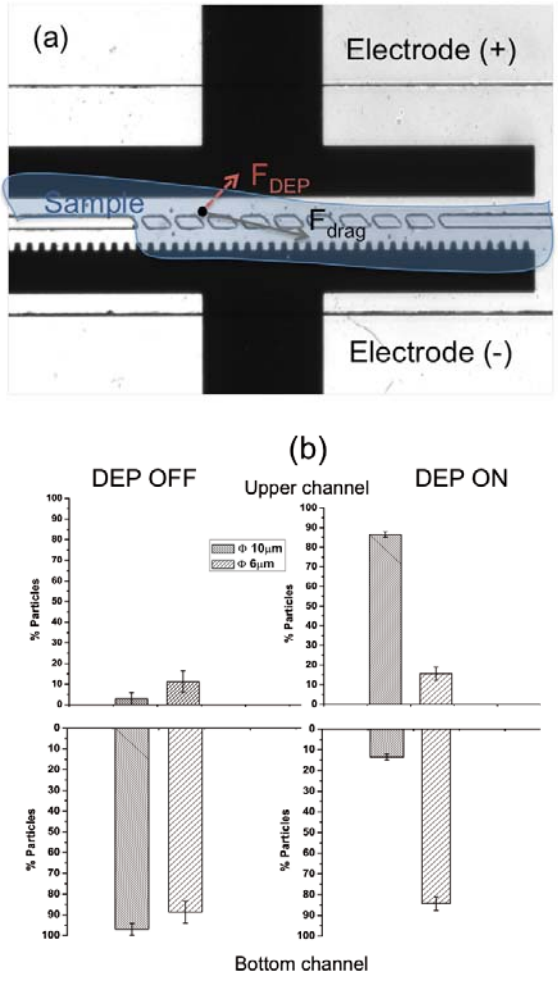

Figure 3.21: Separation results of the deflector system under fluidic conditions of 0.6 μL/min for the sample (in blue in (a)) and the bottom focalisation stream, and 0.8 μL/min for the upper stream. When the DEP is off the samples only experience the drag force, when the electric field is on it also acts the DEP force. The competition between forces will define the trajectory of the particles. In (b) it is plotted the results of the separation. In the case of DEP-off, the particles mainly crossed from the upper channel to the bottom channel, by effect of the dragging force. In the case of DEP-on, only the big particles experienced a DEP force able to be deflected, and mainly remain on the upper channel, while the smaller particles cross through to the bottom channel as in the case of DEP-off.

Figure 3.21a shows an image of the real system used in this experiment. In this picture, the blue cloud indicates the sample distribution for these fluidic conditions. The force diagram indicates the drag force (grey solid arrow), which is always acting over particles, and the DEP force (red dotted arrow), which is only acting when the electric field is applied.

In Figure 3.21b it is represented the distribution of particles when the electric field is off (without DEP forces) and when it is on. Without DEP forces, both large and small particles crossed the intersection zone. About 10% of the small particles remained in the upper channel after the intersection region, while for the 10 μm particles the result obtained is only 3%. The electric field applied has lower effects on small particles than on larger ones. The ratio of small particles between the two outlets with DEP signal OFF is very similar to the case with the electric field ON, meaning that the applied fields have no effect onto these particles. However, the amount of deflected 10 μm beads that remains on the top channel increases up to 90%. The experiments demonstrated that under the same fluidic and electric conditions the size of the particle could trigger a change in its trajectory.

This separation of the 90 % of the particles is significant in front of the efficiencies reported by Chang et al. using their system with polystyrene particles with a linear velocity of 0.2 mm/s (*33*), because our efficiency was achieved at linear velocity of 1 mm/s. This efficiency, obtained with latex particles, demonstrates that our single frequency system can be competitive to separate particles by size in a smaller device and higher linear velocities (Table) than the lateral driven setup (*26*).

3.4.4. Cell separation by size using RBCs and THP-1

First, we used RBC cells (small cells in our sorting example) under physiological conditions, with PBS 1x of a measured conductivity of 1.6 S/m. As it was demonstrated in section 3.2.1., the RBCs, as non-nucleated cells, are in nDEP under

high conductivity buffer (Figure 3.9). The results of the separation of the RBCs were used to find the maximum flow velocity at which the DEP forces are able to deflect the cell trajectory. Then, those results were compared with the fluidic conditions obtained for similar separation efficiency for the large cells (i.e., THP-1 cell line also diluted in PBS 1x). This comparison allows us to find a flow rate regime where we could separate one cell population from the other. In these experiments we used a microfluidic system with an upper channel of 300 μm wide and a bottom channel 200 μm in width. The total height of the channel was 50 μm.

Using a RBCs dilution, we first set a flow rate of 0.2 μL/min for the sample and for the bottom focalisation streams. Then, a flow rate of 0.5 μL/min in the upper stream is able to focalise the sample and force the cells to cross the pillar zone. Afterwards, the velocity of the upper focalisation flow was increased up to 0.8 μL/min. For this high velocity, the number of cells that cross the electrical barriers was quite large and the deflection efficiency was low. Then, we reduced the focalisation flow rate to 0.6 μL/min and the efficiency of the separation increased. Under these fluidic conditions, the sample stream was totally forced to cross the pillar array to the bottom channel.

Without any electric field applied, in DEP OFF conditions, most of RBC cells crossed the pillar region from the upper channel to the bottom channel pushed by the hydrodynamic forces, (Figure 3.22). Comparing with the 6 μm size latex beads (Figure 3.21), the number of RBC cells that remained in the upper channel only decreased by 5%. This is due to the more restricted focalisation conditions used in this experiment.

When an electric field is applied, DEP ON, a large number of RBCs was deflected along the pillar region, as expected. In this case, about 90% of cells were deflected and forced to stay in the top channel, similar to the 6 μm latex particles.

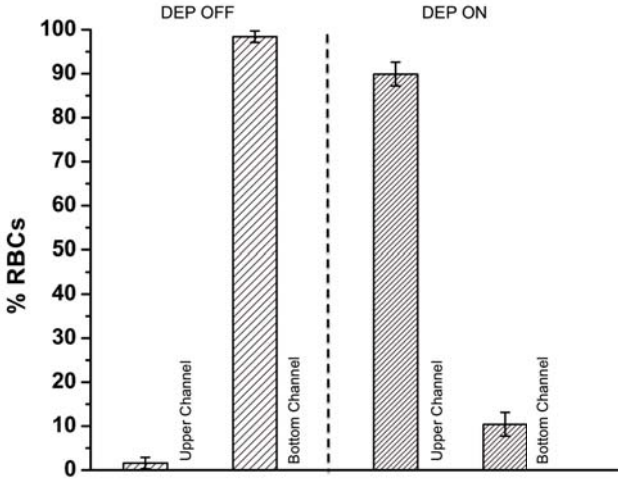

Figure 3.22: Deflection efficiency of RBCs by the system when an electric field of 10 V_{pp} and 10^6 Hz was applied. The flow ratios were 0.2 μL/min for the sample stream and for the bottom focalisation inlet. The Primary focalisation flow rate was fixed in 0.6 μL/min. The process was carried out in a device with channels of 300 μm and 200 μm wide and 50 μm high.

In the case of Monocyte cells (large cells in our binary separation experiment), the focalisation flow rate for the upper focalisation flow was first set to 0.6 μL/min. The limit of the separation was found at 0.3 μL/min for the sample stream, then the upper focussing stream was fixed at 1 μL/min. Figure 3.23 shows the deflection efficiency of Monocyte cell line THP-1 under focalisation rates of 1 μL/min for the upper focalisation stream and 0.3 μL/min for the sample flow and the bottom focalisation stream. This configuration induces a median velocity of 1 mm/s. The deflection efficiency for THP-1 cells is 87%, which is slightly lower than the one obtained with RBCs and comparable to the results obtained for the 10 μm latex beads.

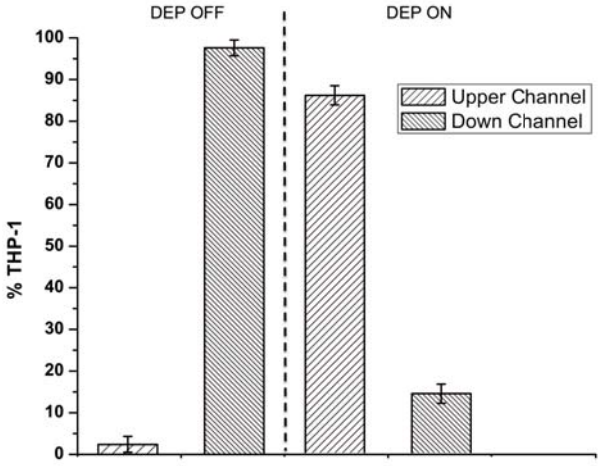

Figure 3.23: Results of deflection obtained by the system over the cell line THP-1, using a flow rate of 0.3 μL/min for sample flow stream and for the secondary focussing flow. The primary focalisation stream was fixed at 1 μL/min. The electric field applied for activate the DEP was an electric field of 10 V_{pp} at 10^6 Hz. In these experiments we used a microfluidic system with an upper channel of 300 μm wide and a bottom channel 200 μm in width. The total height of the channel was 50 μm.

The electrical deflection of the RBCs were achieved at focussing conditions that could be translated in a linear velocity of 0.6 mm/s, while the THP-1 could be deflected at higher velocity conditions, of 1 mm/s. The deflection limits of these two cell types are compared in Table 3.2, which indicates the accomplishment of the electrical deflection at different flow rates. As summary, we could affirm that this system allows the separation of these two cells in a sorting device length of 1 mm with a volume processing capacity of 0.3 μL/min.

Concerning the efficiency and sample velocity, these results were similar to those reported by Han et al. (*26*). In their work, they presented white blood cells separation from RBCs with a good efficiency of 80-93% at 0.83 μL/min. However, our device presented an effective cell deflection with smaller dimensions, supporting higher linear velocities (1 mm/s) than their device (0.1 mm/s) (Table 3.1.)

	0.1 μL/min	0.2 μL/min	0.3 μL/min	0.4 μL/min
RBCs	✔	✔	✖	✖
THP-1	✔	✔	✔	✖

Table 3.2: This table indicates the accomplishment of the cell deflection by √, while an × indicates that the cell deflection is not produced. The table compared the deflection limit for different cells at different flow rates. The red box indicates the optimal conditions to separate red blood cells (RBCs) from THP-1 in our device.

Other devices based on cell levitation by DEP (*30, 43*) show a sample processing velocity close to 1 μL/min (or 60-70 μL/h) which, according to their channels dimensions, lead to linear velocities of 0.01 mm/s, meaning one order of magnitude less than our device. The FFF-DEP system presented by Yang et al. in 2000 (*25*) is the system with the highest sorting capabilities (200 μL/min), while it is the biggest in dimensions (25 mm in width and 0.4 mm in height with a length of 38 cm). Thus, the dielectric barriers designed in our case are a good solution to increase linear velocities.

The sample processing limitation (low flow rates) can be solved with other strategies as for example the system reported by Cheng and co-workers (*34*) that uses two layers of coplanar electrodes and twDEP obtaining flow rates of 10 μL/min under pDEP conditions. The system presented by Baschler et al. (*44*) showed very good performance of separation and characterisation with smaller dimensions than our device, combining nDEP and pDEP by a multi frequency system. However, the use of pDEP force generally requires low conductivity buffers which require sample treatment and non physiological buffers. The pillar structure of our device demonstrates good efficiency deflecting cells in nDEP conditions, allowing to work with physiological buffers.

3.5. Conclusion

The device presented in this chapter is able to deflect cells in physiological buffer, using negative dielectrophoresis and continuous flow. The dielectric pillars approach allows an effective electric barrier generation between two connected channels. The system was able to deviate the cell trajectory using DEP forces with the same order of magnitude than the drag forces, under relatively high linear cell velocities.

The section and size of the system is smaller compared to other systems found in the literature that present similar performance in terms of linear velocities. Although, the sample volume processed per unit time is below 1 μL/m, it can be easily improved by increasing the height of the channel preserving the small dimensions of the system, since the dielectric barriers have demonstrated an excellent performance, influencing in all the channel height.

References:

1. J. El-Ali, P. K. Sorger, K. F. Jensen, Cells on chips. *Nature* **442**, 403 (2006).
2. J. Nilsson, M. Evander, B. Hammarström, T. Laurell, Review of cell and particle trapping in microfluidic systems. *Analytica Chimica Acta* **649**, 141 (2009).
3. H. Thielecke, I. Impidjati, H. Zimmermann, G. Fuhr, Gentle cell handling with an ultra-slow instrument: creep-manipulation of cells. *Microsystem Technologies* **11**, 1230 (2005).
4. M. Ozkan, T. Pisanic, J. Scheel, C. Barlow *et al.*, Electro-Optical Platform for the Manipulation of Live Cells. *Langmuir* **19**, 1532 (2003/03/01, 2002).
5. M. Ozkan, M. Wang, C. Ozkan, R. Flynn *et al.*, Optical Manipulation of Objects and Biological Cells in Microfluidic Devices. *Biomedical Microdevices* **5**, 61 (2003).
6. J. Voldman, Electrical forces for microscale cell mnaipulation. *Annual Review of Biomedical Engineering* **8**, 425 (2006).
7. L. Kremser, D. Blaas, E. Kenndler, Capillary electrophoresis of biological particles: Viruses, bacteria, and eukaryotic cells. *Electrophoresis* **25**, 2282 (2004).
8. C. Zhang, K. Khoshmanesh, A. Mitchell, K. Kalantar-zadeh, Dielectrophoresis for manipulation of micro/nano particles in microfluidic systems. *Analytical and Bioanalytical Chemistry* **396**, 401 (2009).
9. R. Pethig, Dielectrophoresis: Status of the theory, technology, and applications. *Biomicrofluidics* **4**, 022811 (2010).
10. Adrienne R. Minerick, Agnes E. Ostafin, H.-C. Chang, Electrokinetic transport of red blood cells in microcapillaries. *Electrophoresis* **23**, 2165 (2002).
11. J. N. Mehrishi, J. Bauer, Electrophoresis of cells and the biological relevance of surface charge. *Electrophoresis* **23**, 1984 (2002).

12. P. C. H. Li, D. J. Harrison, Transport, Manipulation, and Reaction of Biological Cells On-Chip Using Electrokinetic Effects. *Analytical Chemistry* **69**, 1564 (1997/04/01, 1997).
13. C. R. Cabrera, P. Yager, Continuous concentration of bacteria in a microfluidic flow cell using electrokinetic techniques. *Electrophoresis* **22**, 355 (2001).
14. S. Choi, J.-K. Park, Microfluidic system for dielectrophoretic separation based on a trapezoidal electrode array. *Lab on a Chip* **5**, 1161 (2005).
15. B. H. Lapizco-Encinas, M. Rito-Palomares, Dielectrophoresis for the manipulation of nanobioparticles. *Electrophoresis* **28**, 4521 (2007).
16. Y. Kang, D. Li, S. Kalams, J. Eid, DC-Dielectrophoretic separation of biological cells by size. *Biomedical Microdevices* **10**, 243 (2008).
17. J. L. Baylon-Cardiel, B. H. Lapizco-Encinas, C. Reyes-Betanzo, A. V. Chavez-Santoscoy *et al.*, Prediction of trapping zones in an insulator-based dielectrophoretic device. *Lab on a Chip* **9**, 2896 (2009).
18. N. G. Weiss, P. V. Jones, P. Mahanti, K. P. Chen *et al.*, Dielectrophoretic mobility determination in DC insulator-based dielectrophoresis. *Electrophoresis* **32**, 2292 (2011).
19. P. R. C. Gascoyne, J. V. Vykoukal, Dielectrophoresis-based sample handling in general-purpose programmable diagnostic instruments. *Proceedings of the IEEE* **92**, 22 (2004).
20. R. Pethig, Y. Huang, X. B. Wang, J. P. H. Burt, Positive and negative dielectrophoretic collection of colloidal particles using interdigitated castellated microelectrodes. *Journal of Physics D: Applied Physics* **25**, 881 (1992).
21. H. Morgan, M. P. Hughes, N. G. Green, Separation of Submicron Bioparticles by Dielectrophoresis. *Biophysical Journal* **77**, 516 (1999).
22. Y. Huang, X. B. Wang, F. F. Becker, P. R. Gascoyne, Introducing dielectrophoresis as a new force field for field-flow fractionation. *Biophys. J.* **73**, 1118 (August 1, 1997, 1997).

23. P. R. C. Gascoyne, J. Vykoukal, Particle separation by dielectrophoresis. *Electrophoresis* **23**, 1973 (2002).

24. P. R. C. Gascoyne, Dielectrophoretic-Field Flow Fractionation Analysis of Dielectric, Density, and Deformability Characteristics of Cells and Particles. *Analytical Chemistry* **81**, 8878 (2009).

25. J. Yang, Y. Huang, X.-B. Wang, F. F. Becker *et al.*, Differential Analysis of Human Leukocytes by Dielectrophoretic Field-Flow-Fractionation. *Biophysical Journal* **78**, 2680 (2000).

26. K.-H. Han, A. B. Frazier, Lateral-driven continuous dielectrophoretic microseparators for blood cells suspended in a highly conductive medium. *Lab on a Chip* **8**, 1079 (2008).

27. I. F. Cheng, H.-C. Chang, D. Hou, H.-C. Chang, An integrated dielectrophoretic chip for continuous bioparticle filtering, focusing, sorting, trapping, and detecting. *Biomicrofluidics* **1**, 021503 (2007).

28. M. S. Pommer, Y. Zhang, N. Keerthi, D. Chen *et al.*, Dielectrophoretic separation of platelets from diluted whole blood in microfluidic channels. *Electrophoresis* **29**, 1213 (2008).

29. U. Kim, J. Qian, S. A. Kenrick, P. S. Daugherty *et al.*, Multitarget Dielectrophoresis Activated Cell Sorter. *Analytical Chemistry* **80**, 8656 (2008/11/15, 2008).

30. S.-I. Han, S.-M. Lee, Y.-D. Joo, K.-H. Han, Lateral dielectrophoretic microseparators to measure the size distribution of blood cells. *Lab on a Chip* **11**, 3864 (2011).

31. M. D. Vahey, J. Voldman, An Equilibrium Method for Continuous-Flow Cell Sorting Using Dielectrophoresis. *Analytical Chemistry* **80**, 3135 (2008).

32. M. D. Vahey, J. Voldman, High-Throughput Cell and Particle Characterization Using Isodielectric Separation. *Analytical Chemistry* **81**, 2446 (2009).

33. S. Chang, Y.-H. Cho, A continuous size-dependent particle separator using a negative dielectrophoretic virtual pillar array. *Lab on a Chip* **8**, 1930 (2008).

34. I. F. Cheng, V. E. Froude, Y. Zhu, H.-C. Chang *et al.*, A continuous high-throughput bioparticle sorter based on 3D traveling-wave dielectrophoresis. *Lab on a Chip* **9**, 3193 (2009).

35. N. Demierre, T. Braschler, P. Linderholm, U. Seger *et al.*, Characterization and optimization of liquid electrodes for lateral dielectrophoresis. *Lab on a Chip* **7**, 355 (2007).

36. Y. Huang, R. Holzel, R. Pethig, B. W. Xiao, Differences in the AC electrodynamics of viable and non-viable yeast cells determined through combined dielectrophoresis and electrorotation studies. *Physics in Medicine and Biology* **37**, 1499 (1992).

37. H. Morgan, N. G. Green, AC Electrokinetics: colloids and nanoparticles. *Herts: Research Studies Press*, (2003).

38. G. H. Markx, Y. Huang, X.-F. Zhou, R. Pethig, Dielectrophoretic characterization and separation of micro-organisms. *Microbiology* **140**, 585 (March 1, 1994, 1994).

39. Ramos A, Morgan H., Green N. G., Castellanos A., AC electrokinetics: a review of forces in microelectrode structures. *1998 AC electrokinetics: a review of forces in microelectrode structures J. Phys. D: Appl. Phys. 31 2338-53* **31**, 2338 (1998).

40. M. Castellarnau, Development of microdevices for cell handling and characterisation. Applications to the study of electrical properties of cells. *PhD Thesis*, (2008).

41. J. Oh, R. Hart, J. Capurro, H. Noh, Comprehensive analysis of particle motion under non-uniform AC electric fields in a microchannel. *Lab on a Chip* **9**, 62 (2009).

42. R. R. Trujillo, High speed microfluidic devices for particle counting on a chip. (2008).

43. Y. Li, C. Dalton, H. J. Crabtree, G. Nilsson *et al.*, Continuous dielectrophoretic cell separation microfluidic device. *Lab on a Chip* **7**, 239 (2007).

44. T. Braschler, N. Demierre, E. Nascimento, T. Silva *et al.*, Continuous separation of cells by balanced dielectrophoretic forces at multiple frequencies. *Lab on a Chip* **8**, 280 (2008).

Chapter 4 : Impedance microcytometer analysis

In this chapter we present a custom-made electronic instrumentation able to count particles and cells by impedance detection. This system is an analogical device with high reliability, very cheap and small. We also present a simple approach to validate the electrical counting based on the synchronisation of electrical and optical signals. We are able to track red blood cells over time and compare their position and shape with the evolution of the resulting electronic transition.

The system is used to count and size blood cells by analysing the amplitude of the obtained electrical signal.

4.1. Introduction

The development of cell counters and cell analysers is very important to understand fundamental processes of the cell, to diagnose and to monitor diseases. Commercial flow cytometers provide this information by detecting changes in cell volume, membrane surface morphology, cell structure or differences in protein composition. For that reason flow cytometers are widely used in hospitals and laboratories to perform these kind of studies (*1*).

The main sensing principles are based on light sensing and electric sensing in the macro-scaled (commercial) systems. The light sensing principle use either scatter sensing, when the cell disturbs a focussed light stream, or fluorescent detection. The perturbations produced in electric fields can also be used to detect cell transitions. In 1956, W.H. Coulter developed the first electrical flow-cytometer using two separated reservoirs with electrolyte solutions connected by a small orifice. He sensed the pass of particles through the orifice by resistive detection using a DC voltage (*2*). Two electrodes placed at both sides of the orifice carried out the electric measurement. When a particle crosses the orifice, displacing the electrolyte, the resistance between the electrodes is altered and measured as a current pulse. Each pulse corresponds to the transition of a particle, and the amplitude of this pulse is proportional to the amount of the fluid displaced, thus the particle volume. The principal application of Coulter counters is in haematology, for blood cell counting and sizing.

The performance of the Coulter detection system depends on the relation between the diameter of the orifice and the particle size. The use of a small orifice increases the sensitivity for small particles, but it restricts the detection of big particles. Some commercial strategies are based in the use of exchangeable orifices with different diameter according to the needed detection limit and particle size.

The miniaturisation of commercial flow cytometers using new microfluidic technologies could provide smaller and cheaper systems with smaller detection areas

and improved detection ratios. Then, these micro flow cytometers appear to be a solution to be integrated in a lab on a chip (LOC) systems, opening a possibility for portable and faster systems.

In the literature, one can find many attempts to design flow cytometers that use microfabrication technologies. Some reviews summarize several detection options. Huh et al. and Zhang et al. (*3, 4*) offer a nice introduction to several approaches from the point of view of the detection strategy (electronic, photonics, etc..). In particular, several groups have focused in the miniaturisation of the electronic detection. There are many examples that report designs that have proved feasible the use of impedance detection methods at the micro scale. Sun and Morgan have recently published a nice review of microcytometers based on impedance detection strategies (*5*).

4.1.1. Micro flow cytometers using DC (micro coulter counters)

There are some examples of miniaturisation of the traditional Coulter counter detection by microtechnologies (MEMS). These systems combine a fixed aperture with impedance pulse detection, normally using a DC electric field. Satake and collaborators, for example, presented in 2002 a miniaturised Coulter counter (*6*), with an orifice of ~80 μm in width and 45 μm in height (Figure 4.1). The detection system applied a DC electric field between electrodes with large areas and measured changes in resistivity by an amplifier with an oscilloscope. They reported the counting of red blood cells (RBC).

Saleh and Sohn reported in 2003 a device with very high sensitivity by using a small aperture consisting in a pore of 3 μm in width by 200 nm in height. They were able to count single DNA molecule transitions (*7*) using low voltages and a four electrode architecture for impedance measurements.

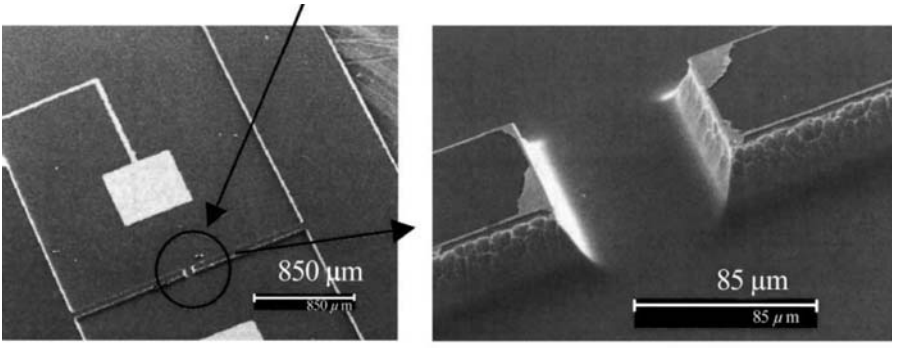

Figure 4.1: Image of the sensor device fabricated by Satake and collaborators. These pictures show the structure of the device with an aperture between two chambers and the electrodes. (6)

In order to increase the throughput of this kind of systems and decrease the time of sample processing, Zhe et al. developed a four aperture system to multiplex the sensing capabilities by four parallel channel apertures (*8*). The system from Zhe et al. used the same ground electrode and four active electrodes placed at each aperture.

4.1.2. Micro flow cytometers using AC (impedance micro flow cytometers)

The measurements using AC electric fields allow the utilisation of smaller sensing areas and the possibility of developing systems for single cell analysis (*5, 9*). Under AC fields, the electrode area and the measurement frequency must be well controlled to avoid the double layer capacitance [2] related to the electrode polarisation. The measurement of the particle transitions results in a modulated signal.

The first example of counting particles by impedance measurements was the system proposed by Gawad et al. in 2001 (*10*). The sensing strategy was based on a Wheatstone bridge to transform the impedance changes into a voltage signal. They used the Wheatstone bridge to compare two pairs of electrodes to avoid the drift of the impedance measurements in liquid conditions. The demodulation system used by Gawad was a lock-in amplifier.

[2] See theoretical considerations in Chapter 1, section 1.4.2.

Multichannel lock-in instrumentation leads to the use of two frequencies simultaneously. The Gawad´s architecture was used to count and differentiate RBC's from polystyrene beads and ghosts cells by Cheung et al. (*11*). The same instrumentation was used by Morgan and Green to work synchronously with fluorescence detection (*12*). Nieuwenhuis et al. used a trans impedance amplifier, while the signal obtained was demodulated by a commercial lock-in amplifier at a single frequency (*13*).

The use of lock-in detection systems raises some issues concerning system integration and cost. Indeed, these commercial instruments imply an increase in the complexity and dimension of the detection system, which goes against the idea of miniaturization exposed previously. Moreover, in the case of highly integrated systems or low cost systems, simpler detection schemes may be advisable. In this direction, few groups have developed alternative low-cost instrumentation schemes, and have designed smaller and compact instruments. De Bisschop presented a specific electronic instrumentation based on a digital signal processing programmable device (*14*). Bisschop used a four electrodes gating system to transduce resistance to voltage. The results were adapted by a low pass filter and instrument amplifier, and then he used an analogic to digital converter to drive the modulated signal to the DSP module.

Zheng et al. (*15*) also used the four electrode architecture with a small aperture to detect cell transitions, and a low pass filter and instrumentation amplifier to adapt the signal. In this case, Zheng used instrumentation based on a true RMS to DC converter to demodulate the signal. These two examples of instrumentation perform the signal demodulation by digital systems as DSP or AC/DC converters.

We focused our work in developing a new and compact instrumentation system, which would be a low cost alternative to lock-in detection schemes or digital signal processing. The goal of our design is to be incorporated in a compact and small microcytometer. The instrumentation that we propose will be able to detect and count

cells using a single frequency system.

4.1.3. Optical synchronised device

In addition to the electrical instrumentation, and related to high detection ratios, it is important to use a validation system of the electric transitions to study and analyse the results. Holmes et al. used an image acquisition system based on a confocal microscope synchronised to their lock-in amplifier (*12, 16*). The combination of an electrical system with the optical detection of specific labels was used by Holmes et al. to perform a bead-based immunoassay (*16*). This system was also used by Benazzi et al. to detect and differentiate between two kinds of phytoplanktonic species, which had intrinsic fluorescence properties (*17*).

Similarly, we decided to develop an optical detection system to analyse the electrical signal correlating the cell positions over the electrodes with the transition pulses obtained.

4.2. Bandwidth definition

As explained in Chapter 1, when an electrode is immersed in a conductive liquid, the charged surface of the electrodes attracts the free ions of the electrolyte. Thus, the so called Stern layer is formed on the metal surface by the accumulation of ions. When charge is accumulated at the interface between the electrode and the electrolyte, the system behaves as a capacitor with a non-uniform charge density (*18*).

The total impedance between two electrodes could be modelled as a *RC* series system, where the *capacitance* is given by the electrolyte-electrode interface capacitance C_I, and the resistance comes from the conductivity of the solution, as it is shown in Figure 4.2.

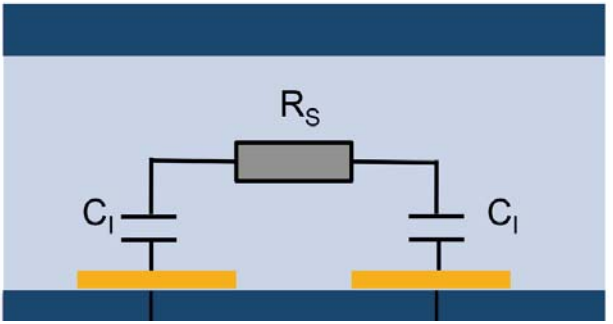

Figure 4.2: Schematic representation of the circuit modelling the double layer capacitance and the RC circuit with the interface capacitance C_I and the resistance of the bulk solution R_s.

The interfacial capacitance (C_I), can be expressed as the serial combination of two capacitances. First, the Helmholtz capacitance (C_H), which corresponds to the Stern layer, and second, the Gouy-Chapman capacitance (C_G), which corresponds to the diffuse layer, (see equation 1). We can define the total impedance, Z_I as the impedance of the system at frequency *f*. The constant *i* is the imaginary constant ($\sqrt{-1}$). As Z_I is inversely proportional to the electrode surface area, its value can be significant at the micro scale.

$$\frac{1}{C_I} = \frac{1}{C_H} + \frac{1}{C_G} \quad ; Z_I = \frac{1}{i2\pi f C_I} \qquad \text{Equation 1.}$$

In addition, parasitic impedances also affect the measurement. When using parallel and coplanar electrodes the stray capacitance can be calculated following the Olthius et al. determination (*19*). Thus, the parasitic capacitance C_p can be calculated by equation 2:

$$C_p = \frac{\varepsilon_0 \varepsilon_r}{2} \frac{K\left[\left(1-k^2\right)^{1/2}\right]}{K(k)} \quad \text{Where } k = \frac{s}{s+2w} \qquad \text{Equation 2. (19)}$$

Where *K(k)* is the complete elliptic integral of the first kind, *k* is a factor which depends on the geometry of the relevant dimension of the electrodes, *s* is the distance between the electrodes and *w* is the width of the electrodes. This model assumes that the electrodes have the same size. C_p is the capacitance per unit length. The total capacitance is then the added contribution for all the faced length of the interdigitated electrodes (*Cp*l*).

The resistance of the electrolyte solution R_s can be calculated from Equation 3 (*20, 21*).

$$R_s = \alpha \frac{L_e}{\sigma w_s h_s} \qquad \text{Equation 3}$$

Where L_e is the length of the sensing surface, including the width of the electrodes, σ is the conductivity of the fluid and w_s and h_s are the width and height of the channel. The geometrical factor α is necessary to take in account the effect of using coplanar electrodes instead of facing electrodes. This geometrical factor is adjusted using experimental data and take values from 0.9 to 1.7 (*21*).

4.2.1. Bandwidth simulation of an impedance microfluidic sensor

Using this simple model, we calculated the expected impedance of a conductive solution confined in a channel with a cross-section of 45 μm wide and 20 μm high and excited by electrodes, 30 μm wide separated 30 μm.

To calculate the expected resistance of the fluid under this geometry, we considered a solution conductivity of σ=1.6 S/m (equivalent to an isotonic buffered solution), and a geometrical factor of α=1.4, which is recommended for this electrode size (*21*). This results in a resistance $R_S \approx$90k Ω calculated from Equation 3.

For the double layer capacitance, we first estimated the Helmholtz capacitance, which

the nominal value for Helmholtz distance, d_{HP}, of 5 Ä (*22*), and an effective electrode area of 1350 μm^2 (30 μm from electrode wide and 45 μm from the channel width).

$$C_H = \varepsilon_r \varepsilon_0 \frac{A_e}{d_{oHP}} \qquad \text{Equation 4.}$$

then C_H calculated is ~189 pF.

Using the electrode area, the diffuse layer length value (λ_D), which for PBS buffer solution (1.6 S/m) is around 0.7 nm (*22*) and equation 5, C_G is calculated as ~1500 pF. Thus, the total interface capacity C_I can be estimated as ~160 pF.

$$C_G = \varepsilon_0 \varepsilon_r \frac{A}{\lambda_D} \cosh\left(\frac{zcV_0}{2V_t}\right) \qquad \text{Equation 5.}$$

The stray capacitance was then calculated from Equation 2 using a relative permittivity of 3.8 for glass and 4 for PDMS. Then, the parasitic capacitance value C_p, for a faced length of 1 cm, is ~0.45 pF.

The impedance spectra sensed by the theoretical system considered is shown in Figure 4.3, with values of R_s= 90 kΩ, C_I= 160 pF, C_s= 0.45 nF. The frequency evolution of the impedance shows a capacitance contribution at low frequencies (below 10^4 Hz), which correlates with a decrease in the impedance module and the negative slope and -90º value of the impedance phase. At mid frequencies, between 10^4 and 10^7 Hz, the impedance shows a resistance contribution and the phase reaches its maximal values. At high frequencies, above 10^6 Hz, the impedance returns to a capacitive behaviour.

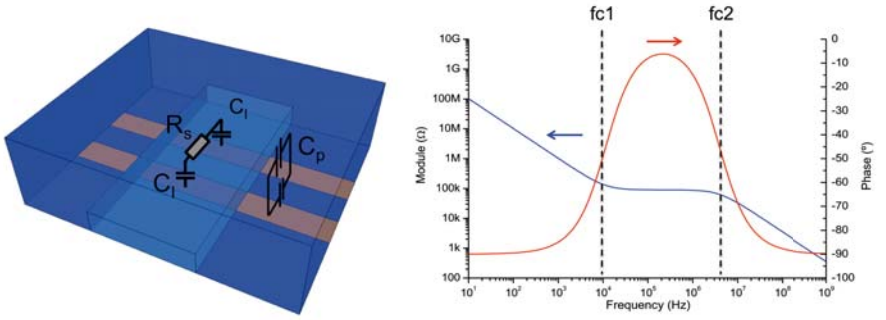

Figure 4.3: Schematic representation of the equivalent circuit of the proposed system. The circuit include the interface capacitance C_l (160 pF), the stray capacitance due to the encapsulation of the electrodes C_p (0.45 pF), and the resistive value from the fluid resistance R_s (90 kΩ). The graph represents the impedance response of the circuit modelled. The impedance module (blue line) and the phase (red line) are plotted as a function of the frequency.

This model shows the effect of the intrinsic capacitances in a microfluidic system. The frequency window where it is possible to sense the resistance R_s is reduced to a bandwidth between 10^4 Hz and 10^7 Hz. The first cut-off frequency, *fc1*, is placed around 10^4 Hz and it depends on C_I and R_s values. The second cut-off frequency, *fc2*, is above 10^6 Hz, and it depends mainly on $C_{p,}$ and R_s values. As the values of C_I, C_p and R_s are defined by the electrodes and channel geometry, the sensing bandwidth of these devices has a strong geometrical dependency.

4.2.2. Electrode characterisation

In this section, the behaviour of a real system was compared to the model of Figure 4.3. The experimental response of the micro fluidic system was studied using an impedance analyser (Agilent 4294A). The device dimensions were the same as the ones used in the modelling: electrodes of 30 μm width separated 30 μm and a channel section 45 μm in width and 20 μm in height. As liquid interface, 1x PBS with a conductivity (σ) of 1.6 S/m was used. This buffer conductivity was measured by a Corning-441 conductivity detector.

Figure 4.4 compares both the theoretical and the experimental impedance responses. It can be seen that the experimental results are comparable to the ideal response of the theoretical circuit. In both cases it is possible to observe the negative slopes due to the intrinsic capacitance of the system. However, in the experimental curves, the low frequency response is not due to a pure capacitance element, as phase values are close to -80º. Moreover, for the bandwidth frequencies, from 10^4 to 10^7 Hz, the experimental curve does not show a perfect plateau and the maximum phase value is lower than in the theoretical model, -10º. These phase values indicate the non-ideal resistive response of the system. The maximum phase value was achieved at frequencies close to 10^5 Hz, at this frequency the impedance module value is around ~100 kΩ. This impedance value is comparable to the theoretical value of R_s≈90 kΩ.

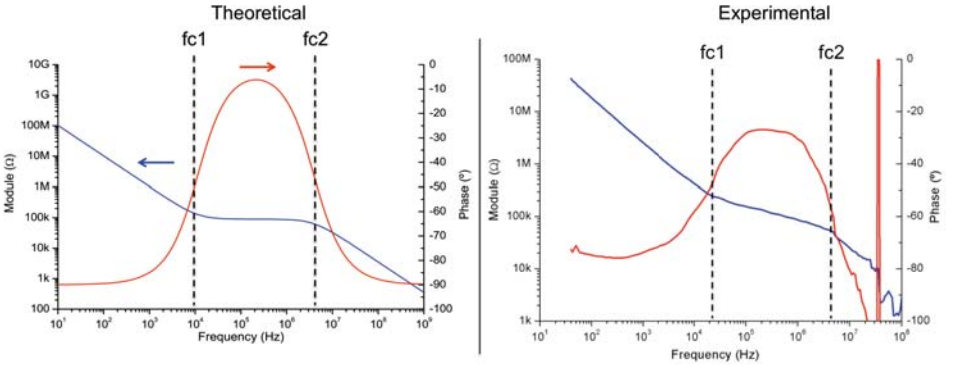

Figure 4.4: Comparison of the impedance response of the theoretical model (left) and the experimental device (right). The impedance module (blue line) and the phase (red line) are plotted as a function of the frequency. The response of the experimental data is similar to the theoretical model. The main differences are the non-ideal capacity response of the double layer interface, and the non-real resistance between the fc1and fc2 by the absence of the plateau on the module response, and phase below -20º, indicating that the impedance response of the media is mainly a complex impedance response.

The experimental behaviour of the system at high frequencies (~10^7) is much similar to the theoretical model, as it appears a second cut-off frequency with a phase close to -90º and a negative slope of the impedance module.

Then, we could conclude that the model presented, is a good approximation to the real impedance system by two electrodes. The frequency bandwidth between 10^4 Hz and 10^6 Hz is the frequency range where the impedance of solution can be sensed. This frequency bandwidth depends on the device geometry. However, the variation expected for the different electrodes and channels used in this thesis are very low.

As explained in Chapter 1, cells can be modelled as complex electric systems. H.P. Schwan studied the electrical properties of cells and tissues, and their electrical impedance. (*23, 24*). Following Schwan work, it is assumed that for frequencies below 10^6 Hz, the cell membrane behaves as a full electric capacitor and no electrical currents flows through the cell. On the other hand, for frequencies higher than 10^4 Hz, we will have electrode double layer effect. Then, we should work at frequencies between 10^4 and 10^6 Hz (we chose 1.2 10^5 Hz (120 kHz)). Within this range, when cells cross the sensing area of the device, the impedance increases locally because they displace the conductive liquid. As a consequence, as in the Coulter systems, the increment of the impedance should be proportional to the cell volume.

4.3. Materials and Methods

4.3.1. Microfluidic device

To achieve an effective counting, individual cells have to arrive to the sensing area one by one. One of the systems used to perform such a cell alignment is the hydrodynamic focussing, which has already being used in microcytometers (*13, 20, 21, 25, 26*). Other interesting examples to generate particle alignment in micro cytometers are the use of dielectrophoresis (*12*) or physical constrictions, as in the case of a Coulter counter.

4.3.2. Channel and electrode fabrication

The microcytometer system was build up by standard photolithography in the Nanotechnology platform at the Parc Científic de Barcelona. The micro fluidic

prototype consists of two layers, one layer with the microchannels made in Polydimethylsiloxane (PDMS) by cast moulding, and the other layer with the electrodes made in glass.

The mould to produce the PDMS microchannels was fabricated with either SU8-10 to obtain channels of 10 μm or less in height, or SU8-50 to obtain channel heights of 20 μm. The spinning velocities were set following photoresist datasheets (MicroChem). After spinning, solvents were evaporated by a using hotplate: 2 minutes at 65º C and 5 minutes at 95º C for SU8-10 and 5 minutes at 65º C and 20 minutes at 95º C for SU8-50. The UV exposure was performed at an intensity of 21 mW/cm^2, 5 seconds for SU-8 10 and 10 seconds for SU-8 50. After the exposure, the photoresists were then baked again to achieve the cross-linking of the exposed resist. This last bake needs 1 minute at 65º C and 5 minutes at 95º C. In order to remove the non cross-linked photoresists we used a commercial SU8 developer solution. The developing process is done by immersion of the substrate during 3 to 6 minutes.

The obtained SU-8 mould is then covered with PDMS (Sylgard 184) in viscous phase, and it is cured in the oven at 65ºC for 1 hour. The PDMS mixture is prepared by a combination of a monomer solution and a cross linker in a 10:1 proportion. After curing, the PDMS covering the SU-8 mould is de-moulded obtaining then the open conformation of the microchannel.

The electrodes were fabricated by using the reversal photoresist AZ-5214E, which is a photoresist especially well suited for lit-off processes. First, we deposited the photoresist at 4000 rpm for 30 seconds on a glass surface. Then, we baked it in a hotplate at 95º C during two minutes, following by UV exposure at 21 mW/cm^2 for 2.5 seconds and a post-bake at 120º C for 2 minutes. The resist was inverted by a flood exposure of light at 28 mW/cm^2 for 10 seconds. Afterwards, a development process was done using a commercial AZ developer during 30 seconds.

The metal deposition was achieved by metal evaporation of 10 nm of titanium, to get good adhesion to the glass surface, and then 80 nm of gold. After deposition, the lit-off of the photoresist was done with AZ remover.

The final implementation of the device was achieved by the physical bonding of the glass with the electrodes and the PDMS replica, by oxygen plasma exposure. In Figure 4.5 we show the final implementation of the micro cytometer developed.

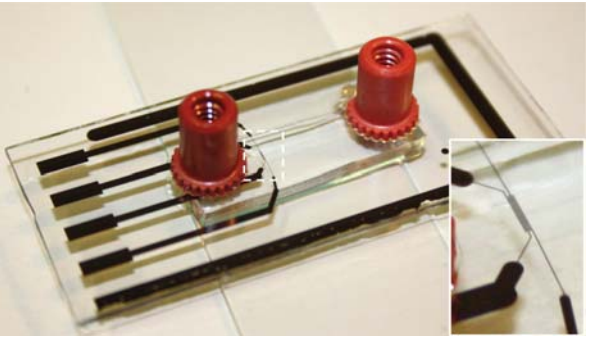

Figure 4.5: Image of the microcytometer developed to characterise the demodulation instrumentation. In the zoom out in the lateral inset shows a magnification of the sensing area.

4.3.3. Electronic instrumentation

4.3.3.1. Wheatstone bridge

In this section, the Wheatstone bridge architecture implemented to convert the impedance changes to a detectable voltage is detailed. To minimise the drift effects in impedance measurements in fluid we implemented two pairs of electrodes following the proposed design by Gawad et al. (*10*), see Figure 4.6.

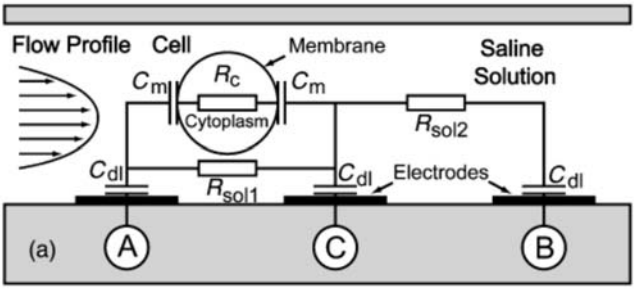

Figure 4.6: Schematic diagram showing the impedance model of three electrode architecture that form two pairs of electrodes. This system was proposed by Gawad in 2001.(10)

The two sensing zones were built up using three electrodes, with the middle electrode as the common grounded electrode. The resulting two sensing volumes were located at different branches of the bridge, as shown in Figure 4.7. The Wheatstone bridge also includes an instrumentation amplifier with a gain of 100 times and two resistors Rp1 and Rp2 to form the branches of the Wheatstone bridge.

The resistors Rp1 and Rp2 were designed with a potentiometer (0-20 kΩ) and standard resistor (40 kΩ) to have an impedance range that allows the equilibrium conditions between both branches of the bridge. The resistor values were chosen to match the measured impedance between a pair of electrodes in the frequency range of operation (around 100 kΩ in the range 10^5-10^6 Hz).

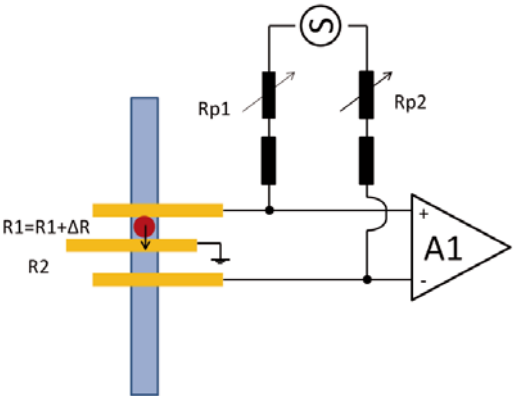

Figure 4.7: This figure represents the layout of the Wheatstone bridge with the connections to the electrodes in the microfluidic channel. A1 is the instrumentation amplifier with a 100 times gain. The resistors Rp1 and Rp2 were designed with a potentiometer (0-20 kΩ) and standard resistors (40 kΩ) to have an impedance range that allows better equilibrium conditions between both branches of the bridge. The blue box represents the micro fluidic channels, the yellow boxes represent the electrodes and the red circle represents the particle.

As we showed in the previous section, the response of the system is not fully resistive. The presence of capacitance effects will make difficult the bridge equilibrium, since only resistive elements are used to equilibrate the impedance differences between the two pairs of electrodes. In Figure 4.8, it is plotted the experimental impedance response for two pair of contiguous electrodes 20 μm wide and separated by 10 μm in a channel section of 20 μm by 20 μm approximately, when the channel is filled with PBS. These electrode pairs will be connected to $A1^+$ with the common ground, and the common ground with $A1^-$, as shown in Figure 4.7. The response of these electrodes shows differences in the phases with values below -50º, indicating that the perfect equilibrium position of the bridge is very difficult to accomplish. However, as it will be shown later on, this does not limit at all the performance of the device.

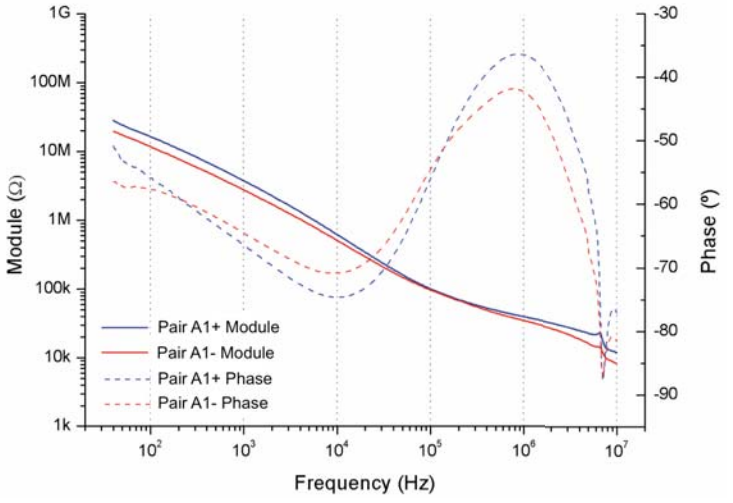

Figure 4.8: Response of two pairs of electrodes with the channel filled with PBS with a conductivity of 1.6 S/m. Red and blue lines represent module and phase impedance responses, respectively. Solid and dashed lines account for the two different pairs of electrodes. The differences between the two pair of electrodes from the same device detected results in imperfections and a noisy signal. Obtained from a device with a cross-section of channel of 20μm width by 20μm height and electrodes of 20μm width separated 10μm.

4.3.3.2. Demodulation system

In this section we present the electronic instrumentation to transform the signal produced by the cell crossing the sensing area into an easily detectable signal. The electronic instrumentation was designed following the standard architecture of a signal demodulator.

Under ideal conditions, in which the bridge would be completely balanced and no particle is on the sensing area, the output of the instrument amplifier A1 (Figure 4.7) should be 0 V. Therefore, when a particle crosses the first pair of electrodes the voltage would increase due to the higher particle impedance. When the particle crosses the second pair of electrodes the same effect will occur, with 180º phase shift because of

the negative input on the amplifier. The rising times of the modulation and the total time of the transition depend directly on the velocity of the sample.

A simulation example of the modulation expected is shown in Figure 4.9, for a particle with a size comparable to the electrode dimensions and separation. This signal was simulated using a base sinus of 120 kHz, which was modulated in amplitude by a square signal with 2 kHz frequency and 1 ms duration, representing the cell transition. The relevant information describing the particle transition dynamics corresponds to the envelope of the electric signal. The developed circuit chosen here for signal processing is therefore a standard architecture for amplitude demodulation: one rectifier and the extraction of the envelope by a low-pass filter. A further high-pass filter to remove any signal offset and a final amplification were also added to the basic setup, as shown in Figure 4.10.

The filters used were Sallen-key architectures. The low-pass filter is a fourth order filter with 10 kHz cut-off frequency and a quality factor of 0.5. The high-pass filter is a second order filter with 7 Hz cut-off frequency and a quality factor of 0.5.

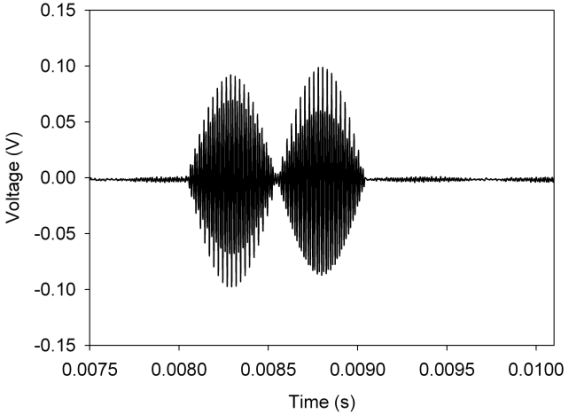

Figure 4.9: Theoretical transition due to the change on the impedance as a result of the flow of particles over the electrodes connected to the Wheatstone bridge. The transition is based on the sinus modulation effect of a particle.

This architecture was initially implemented using SPICE simulation software to validate the electronic design. Figure 4.10 shows the effect of the rectifier and the low-pass filter, which give the envelope of the signal, and the effect of the high-pass filter.

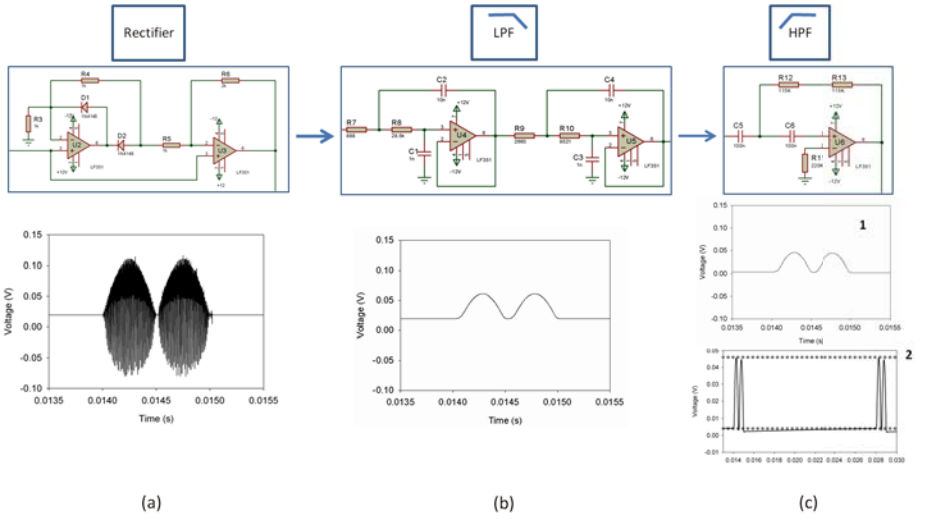

Figure 4.10: Representation of each module of the demodulator system, and the response of the SPICE model when the signal plotted in Figure 3 was applied. It shows how the rectifier (a) follows a low amplitude and fast signal, the next step of low pass filter (b) gives the envelope of the rectified signal, and finally the signal is centred on zero by the high pass filter (c), this last step results in a slight deformation of the signal (c-2).

The high and low pass filters affect the signal morphology. The low pass filter reduces the amplitude of the signal because of the removal of some of the frequency components. The high-pass filter is constantly setting the mean value of the signal to zero and this generates an effect on rising time after each transition and a secondary peak deformation. The high-pass filter deformation is highlighted in the inset (c-2) in Figure 4.10, by including the dotted straight line. The main role of the high-pass filter is to reduce the offset signals.

After the SPICE study, the electronics was implemented and the design was validated using a programmable function generator (TABOR Electronics. WW5061). The signal represented in Figure 4.9 was generated by a LabVIEW program and loaded as an arbitrary form using the function generator. The signal was applied to the electronic filters implemented and the demodulation process was tested by the acquisition of the signal after each demodulation step by a National Instruments acquisition board. The results of rectification (a), low-pass filter (b) and high-pass filter (c) are displayed in Figure 4.11. As can be seen, the instrumentation developed displays a response in complete agreement with the SPICE model simulated before.

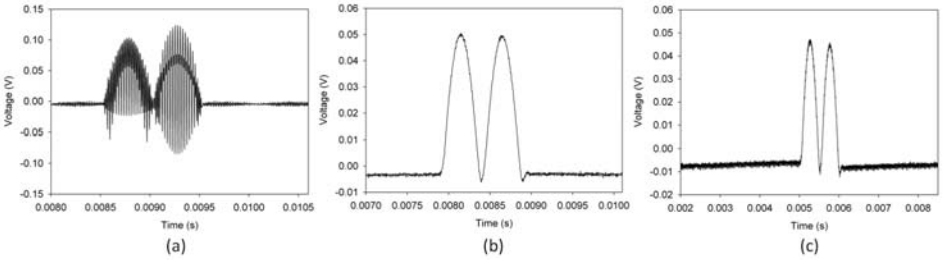

Figure 4.11: Response of individual modules of the real electronic circuit when an ideal signal as the one in Figure 4.9 was applied using a programmable signal generator. Note that the signals are identical to the SPICE model, the rectifier (a), the envelope of the signal obtained by the low pass filter (b), and the small deformation generated by the high pass filter (c).

4.3.4. Detection Software

As explained before, a cell crossing the sensing area generates a positive electrical transition detectable by the electrical instrumentation. The instrumentation was designed to detect these individual transitions by a simple electric comparator, which gives a count when the output signal crosses an established voltage threshold.

In order to establish the best threshold conditions, the instrumentation was characterised. The electric evolution of the signal obtained by the electronics was digitalised and saved by an acquisition board (National Instruments, NI-6265). The

images of the cell crossing the electrodes were obtained by a high-speed camera (Photron Fastcam 1024 PCI) installed on a microscope Olympus IX-71.

The amplitude of a transition was defined by the maximum value of the transition in absolute value. As the transitions have two crossing points of the threshold, the transition time was defined as the time from the first rising transition to the second recovery point. The signals obtained for the transitions have been studied in different terms: morphology, amplitude and transition time and compared to the cell position respect to the electrodes.

To achieve the synchronisation between the optical and the electrical signals, a two electrical channel acquisition controlled by a LabVIEW program was developed. The first channel acquired the electrical signal obtained from the demodulator instrumentation, and the second channel saved the status signal obtained from the camera. A MATLAB program finally presented the synchronisation of the electrical signal and the images. The program includes a detection system of the electrical transitions by a threshold method.

4.5. Results and Discussion

The results presented on this section were obtained by using microfluidic systems which differ slightly in their dimensions. The samples used were red blood cells (RBC) from donated whole blood and monocytes from THP-1 cell line (ATCC). The cells were diluted in PBS (Sigma-Aldrich) of a measured conductivity of 1.6 S/m. The flows were pressure driven by using a syringe pump, Kds ScienceElectronics. All the cell transitions shown in this chapter were obtained using the same electronic instrumentation, presented before.

4.5.1. Study of RBCs electrical transitions

The device used in this section is a single channel with a constriction 10 μm wide by 10 μm high. This constriction was defined by the size of the RBC ~7 μm to ensure that

the cells travel one by one. The cell detection was performed in the constriction using coplanar electrodes 20 μm wide separated by 10 μm. The RBC's were diluted in 1xPBS.

Figure 4.12 shows several signals corresponding to particle transitions recorded with two different configurations of the Wheatstone bridge. In both cases, the sample flow rate was kept constant at 0.1 μL/min, resulting in a theoretical mean velocity of the cell in the constriction of 31.9 μm/ms or an equivalent particle time transition of approximately 4 ms. In order to obtain a better understanding of the detection of the cell transition, the signal was acquired at the end of the Wheatstone bridge (first column in Figure 4.12) and after the demodulation process (second column in Figure 4.12). The acquired demodulated signals were then compared to the mathematical result obtained from MATLAB software, which simulated the electronic filters and superposed in the last column in Figure 4.12. In this last column, the resulting MATLAB transition is represented by green traces. In both cases (different bridge equilibriums) the signals are equivalent, indicating that the electronics is working as expected. This result makes evident that the differences in transition morphologies are produced by the differences on the bridge equilibrium position.

The signal represented in Figure 4.12 differs from the ideal one shown in Figure 4.9, because the cell transition over the second pair of electrodes appears as a reduction of amplitude, instead of a peak. These type of signals are obtained when the variation of impedance due to the particle is lower than the impedance base difference between branches. In this case, the bridge is not perfectly balanced and then the presence of the particle is acting to equilibrate the bridge instead of causing disequilibrium. This fact is confirmed in Figure 4.12 (b) by a transition signal displaying a double peak as the theoretical one in Figure 4.9. The signal in Figure 4.12 (b) has been obtained by fine tuning the potentiometers position, resulting in a better equilibration of the bridge and a low noise output signal, around 240 mV peak to peak. In these conditions, some of the particles generated a second peak. It is also important to note that the amplitudes

between case (a) and (b) are significantly different, 0.5 V for case (a), and close to 1 V for case (b).

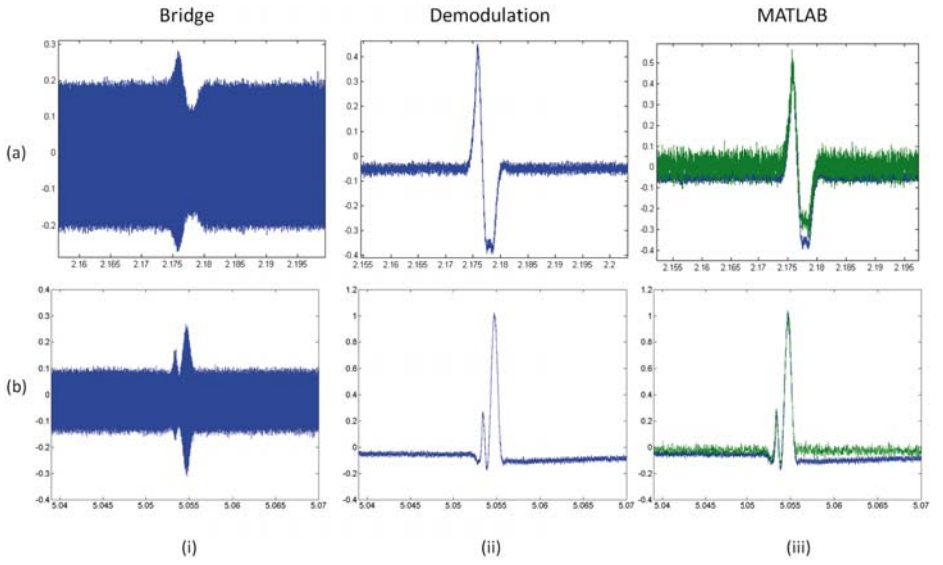

Figure 4.12: Study of different morphologies of recorded signals when the equilibrium of the bridge was changed. Two bridge configurations are considered in (a) and (b). The blue plotted signals are the main signals recorded from the electronic circuit when a RBC cross the sensing area, the bridge signal (i) are recorded from the output of the amplifier of the bridge, A1 in Figure 1. The demodulation signals (ii) are recorded after all demodulation process. The MATLAB plots (iii) are the comparison between the demodulation signal from the electronic system (blue) and the signal obtained with a MATLAB simulation of the filters using the bridge signal (green). On the case (a) was plotted a cell transition when the bridge was equilibrated to obtain a base out signal of 400mV peak to peak, in case (b) the bridge was fixed and equilibrated to 240mV peak to peak, showing the two peaks.

As it was discussed in section 4.3.3.1, the variation of the bridge equilibrium generates different transition morphologies. As it will be shown, this does not constitute any problem for counting. However, the size determination should be achieved by the relative amplitude comparison under equal bridge conditions.

4.5.2 RBCs electronic and optical signals synchronisation

This section presents the optical system used to validate the electrical transitions detected. A fast microscope camera was synchronised with the electrical signal acquisition. The optical instrumentation allows us to record live images of cells travelling across the electrode array in parallel to the electronic acquisition. An external trigger was used to synchronise the two separate signals at once. A common starting time point was set as explained in section 4.3.4. Thus, it was possible to identify the images corresponding to each electrical transition by knowing the frame rate of each acquisition system.

The synchronisation system was tested using RBCs diluted in 1xPBS. The electrical signal was obtained simultaneously from the output of the Wheatstone bridge and from the output of the demodulation system. The validation was performed for a bridge equilibrium setup resulting in a 200 mV peak to peak signal. The flux velocity was fixed at 0.5 μL/min with a transition time of 1 ms. Figure 4.13 shows six images of a cell crossing the sensing zone at specific positions of the electrode array. The sensing electrodes which formed the bridge are the three first electrodes from the left. The time of each image is shown. Below the images, the signal recorded from the bridge is plotted in blue, and the final demodulation in green. The red numbered bars indicates the synchronised times of acquisition with the numbered images.

When a RBC crossed the first pair of electrodes, it increased the amplitude of the difference between the two branches of the bridge, generating the positive lobule of the transition. This positive lobule had a maximum value when the particle was just in the middle of the pair of electrodes. In image 4 from Figure 4.13, the cell is placed at the next pair of electrodes. In this case, the impedance increasing effect is translated into a subtraction of the amplitude, because the pair is connected to the negative input of the amplifier. The maximum of the last negative lobule reaches the maximum value between the electrodes. When the cell leaves the sensing area the electrical transition is over.

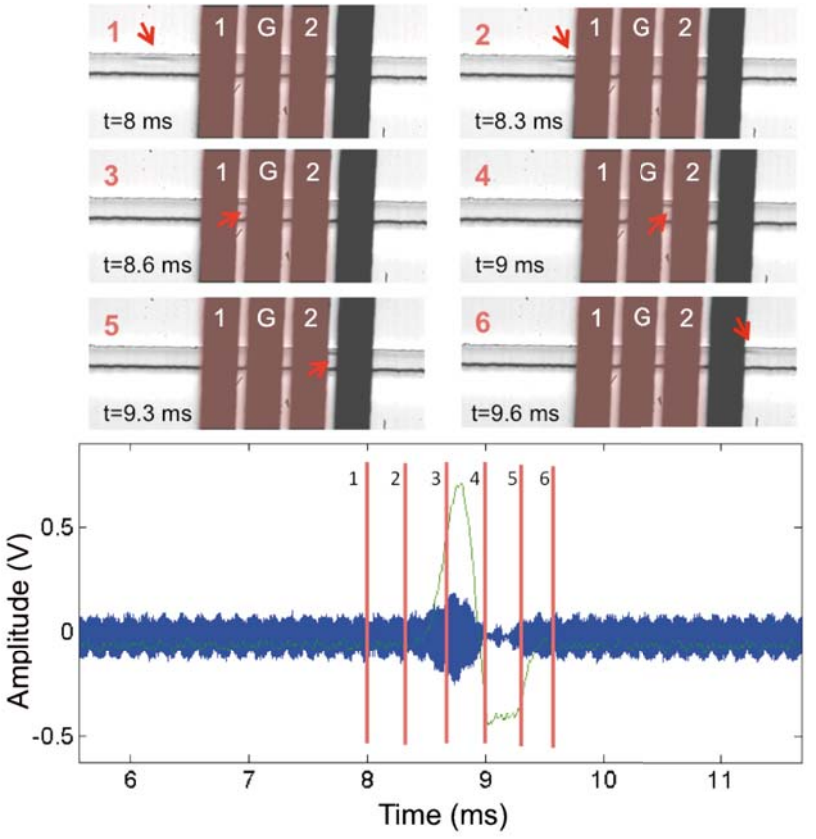

Figure 4.13: Representation of the synchronisation of an optical acquisition of a cell crossing the sensing electrodes and the signals recorded from the electronic circuit (the blue one from the bridge and the green one from the final output of the demodulation process). The images were taken at different stages: outside of the sensing zone (1,6), close of the electrode array (2,5); start and end of the transition, inside the electrode array: first pair of electrodes (3) and second pair (4). The red bars on the signal plot represented the time points corresponding to the numbered image of the particle.

Using this synchronisation system more than 200 transitions were validated, and the reliability of the electrical recording system was shown to be above 95%. These particles were registered on the video and at the same time detected and counted using MATLAB. The remaining 5% of transitions were detected by the threshold system, but the cells were not visible in the optical images. These errors were attributed to the finite

focal distance of the optical system and the fact that the cell was travelling in a different plane, thus was invisible to the camera. This statement is supported by the lower amplitude of the transitions detected by the electrical signal, meaning that the cells were travelling far away from the electrodes where the microscope was focused.

Finally, the optical system also allowed us to demonstrate the capability to detect particles at high speed (0.3 ms transition time). This fact is illustrated in Figure 4.14, which shows two RBC's consecutively travelling with a flow rate of 2 µl/min, meaning a theoretical transition time of 0.3 ms over the 72 µm length of the electrode array. In the figure, these two transitions were detected during this time period, illustrating the possibility of counting up to 3000 particles/second.

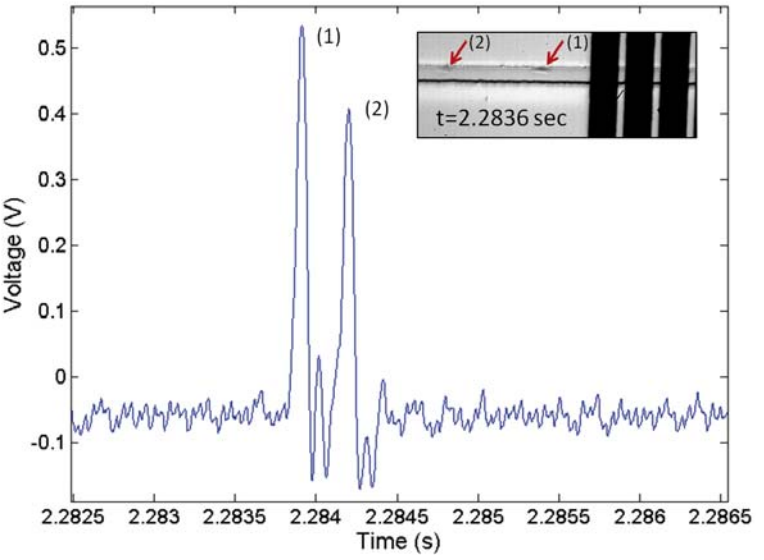

Figure 4.14: Representation of the electronic signal recorded at the end of the demodulation process of the RBC's travelling in the channel with a flow rate of 2 µl/m, meaning a time transition of 0.3 ms, when the bridge was balanced by 300 mV peak to peak. Two cells were recorded crossing the sensing zone consecutively. The inset shows an image from the channel some time before the cells crossed the electrode array, resulting in the detection of the two cells.

4.5.3. Counting rate and sizing capabilities. RBCs and THP-1

To demonstrate the sizing capabilities of the electronic instrumentation we performed experiments using a mixed dilution of the red blood cells (RBCs) with larger cells (white blood cells, THP-1 monocytes). The channel constriction dimensions were 20 μm by 20 μm and the electrode dimensions were 20 μm wide separated by 10 μm.

The mixed cell buffer was diluted in 1xPBS with a cell ratio of 1 WBC to 100 RBCs. The RBCs have a disk like shape, so they can be represented as small cylinders with a base diameter of 6-8 μm and heights of 2-2.5 μm. In this chapter we used the immortal monocyte cell line THP-1. This cells in normal conditions have a stable distribution of sizes centred at ~12μm.

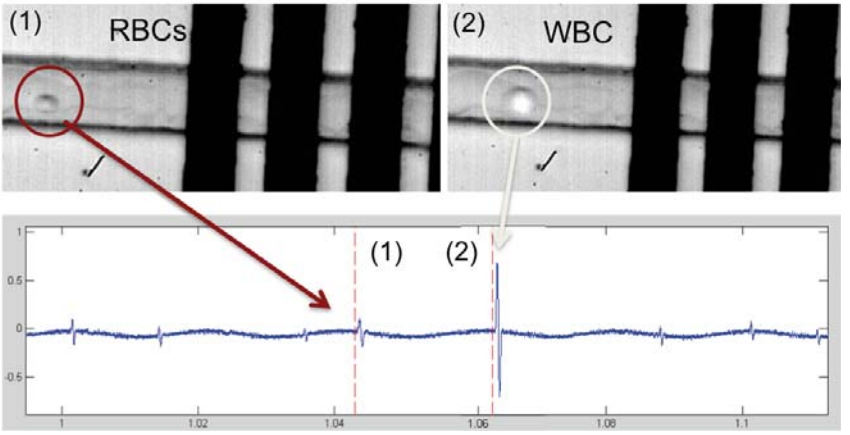

Figure 4.15: Representation of the electrical signal obtained by the demodulation system. The synchronisation system allows correlating the electrical signal with real images of the cells that produce the electrical transition. The red dashed lines indicate the time points at which the images were taken. In this figure it is possible to correlate the transition produced by a red blood cell (1), with low amplitude, while the transition (2) was correlated with a Monocyte transition, with an important increasing in amplitude.

In Figure 4.15 is possible to see the electric acquisition obtained by the synchronisation system, coupling the image acquisition and the electrical signal. In the electrical signal,

it is possible to see the difference in amplitude between the transitions of small cells (RBCs, (1)) and the transitions produced by big cells (WBCs, (2)). The difference between the signals seems significant, as the amplitude of the RBCs electrical transitions is less than 0.01 V of amplitude, and the amplitude of the monocyte electrical transitions is above 0.5 V of amplitude.

4.5.3.1. Counting rate

First, the system was tested to demonstrate the capability to detect particles at high speed (0.2 ms transition time). Figure 4.16 shows the scatter plot of a single acquisition of 8.8 seconds of the sample travelling at high flow rate. The scatter plot represents the detected transitions correlating their amplitude with their transition time.

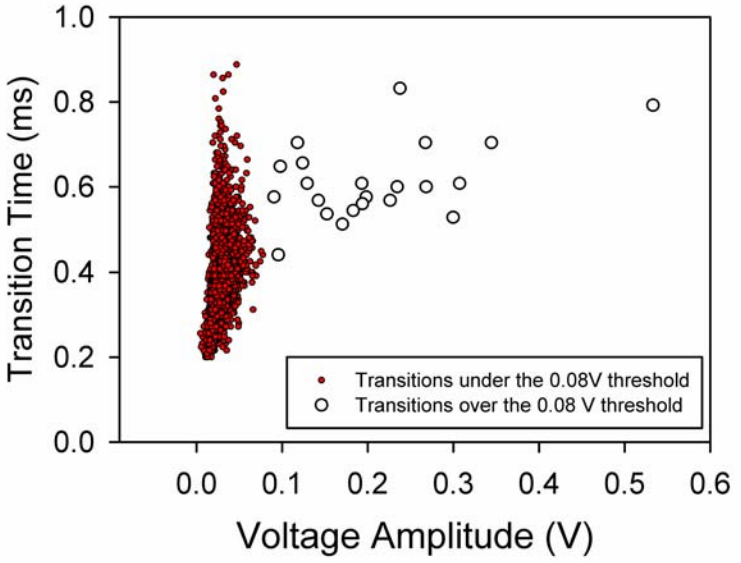

Figure 4.16: Scatter plot representation of the 4767 transition acquired in a lapse time of 8.8 seconds. This acquisition done at high velocity of sample flow, demonstrated a detecting rate of 542 cells/second. In this acquisition we used two thresholds to distinguish between the two cell types used. The low threshold defining a cell transition was fixed at 0.01 V while the threshold for WBC was fixed at 0.08 V.

In this case two threshold levels were used to differentiate between RBCs and WBCs. The main threshold to detect cell transition was set at 0.01 V. The second threshold value was fixed at 0.08 V. Transitions between 0.01 and 0.08 V were attributed to RBCs and transitions over 0.08 V were attributed to WBCs. The total cells detected were 4767 in 8.8 seconds, which means a real sample rate of 542 cells/second. The lowest transition time obtained was 0.2 ms, which could be translated in a potential sample rate of 5000 particles/second for an ideal sample disposition, without overlapping.

4.5.3.2. Sizing capabilities

Figure 4.17 shows the results of the three consecutive acquisitions of 8.8 seconds. Again, the separation between cell types was achieved by setting two thresholds. The lower threshold defines the cell detection, which is placed at 0.01 V. The separation threshold between RBCs and WBCs is fixed at 0.1 V. At the bottom of Figure 4.17 is represented the projection of the transition distribution as a function of the voltage in a histogram. This histogram shows two different distributions corresponding to the two cell types. We counted 5114 cells from the sample mixture, of which 28 transitions have an amplitude over 0.1 V. The relation between the cell population is close to 0.5%, which is in agreement with the relation of populations within the cell mixture.

The amplitudes obtained for RBC and WBCs detected simultaneously electrically and optically, for fixed bridge equilibrium conditions, were compared to extract the amplitude-cell volume relationship. The studied transitions were selected from five independent acquisitions. This selection ensures that the position of the cell from the electrodes was similar, so the amplitudes are comparable, thus reducing any variation produced by other positions.

The cell volume was calculated taking into account their morphology as acquired with the optical microscopy system. RBCs were modelled as disks and their diameter was estimated from the camera images using image processing software (ImageJ). Their

thickness was taken from the literature (2.5 μm). On the other hand, the WBC's were considered as spheres with a diameter measured from the images.

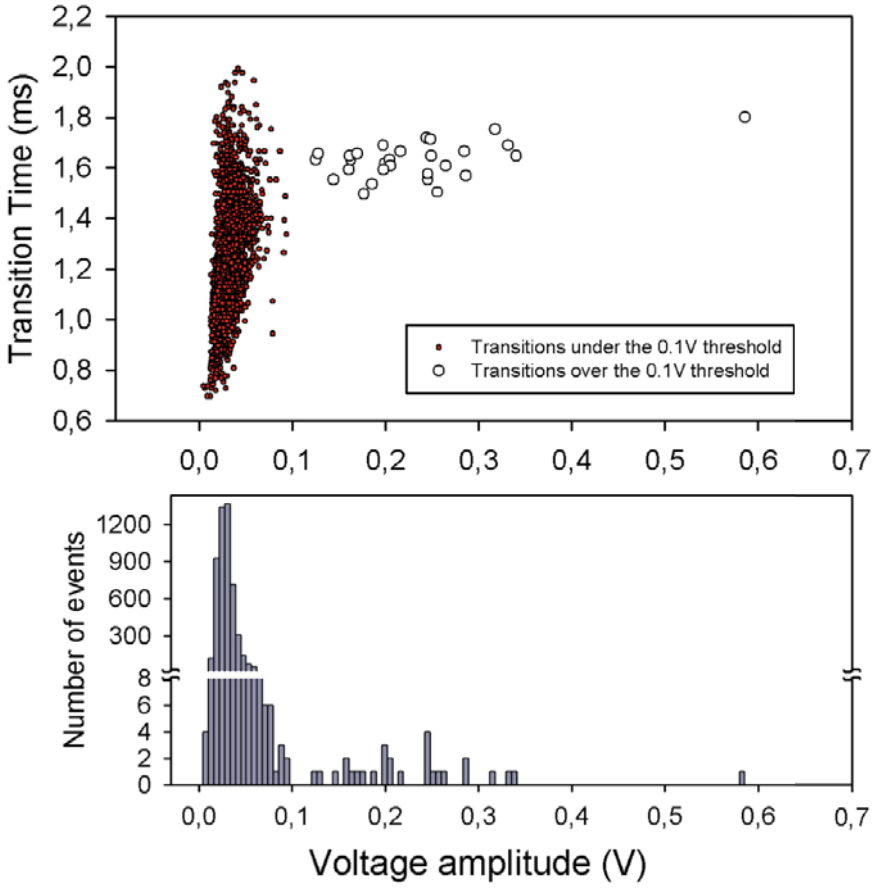

Figure 4.17: Scatter plot and histogram of transitions detected in three consecutive acquisitions of 8,8 seconds (25,4 seconds) under the same hydrodynamic conditions. The cell threshold was fixed at 0.01 V, and the separation cell threshold was fixed at 0.1 V. The histogram is obtained by the projection of the transition amplitude.

In Figure 4.18 we show an almost linear relationship between the amplitude of the electric transitions and the volume calculated for each cell, thus indicating the

capability of the device for sizing applications. The population of the RBCs selected had transitions below 0.1 V. The transitions selected for WBCs (10 transitions) have a mean value of 0.25 V, which correlates with the mean value of the population represented in Figure 4.17. Figure 4.18 present lower deviations for both cell types than Figure 4.17, due to the restriction of the cell position from electrodes in Figure 10. It is worth noticing the presence of some (n=2) anomalous large cells from the cultured THP-1, with significant differences in amplitude and volume.

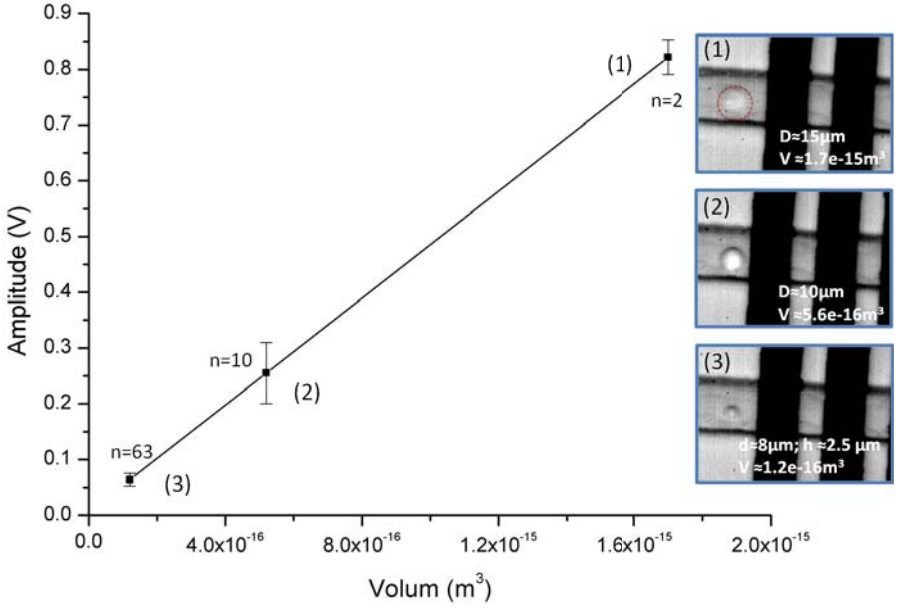

Figure 4.18: Relationship between the electronic amplitude of the recorded signals and the cell volume obtained in a device with a 20 by 20 µm section channel. It is possible to see how under the same bridge conditions the amplitude of the transitions has a linear dependence with the cell volume. The insets show images of the cells close to the electrodes. For the WBC (1 and 2) the volume was calculated as spheres with a diameter measured by image processing software. The volume of the RBC (3) was calculated as a cylinder with a diameter as measured and assuming a high of 2.5 µm.

2.5. Conclusions

The main objective of this chapter was to develop an instrumentation system able to detect the effects of biological samples over an established electric field in a lab on a chip environment. The system was implemented and tested using real samples. The electrical transitions obtained were compared with the SPICE simulations. Differences between simulated and experimental signals were found and attributed to the non-ideal impedance response of the system of electrodes in liquid environment. The transitions obtained were then validated by a synchronisation system, which allow us to correlate the cell position with the evolution of the electrical transitions. We could identify the transition morphology with the cell position, thus all the morphologies were validated and the bridge equilibrium was identified as the main contribution to the morphology differences.

The system was able to differentiate between cell types. It was possible to define two different thresholds one to detect a cell transition, and the second to detect the bigger cell size population. The system was tested using high velocities with this mixed population to evaluate its counting rate capability. Really fast transitions were detected by the electronic instrumentation, below the millisecond scale, the faster transition was of 0.2 ms. These fast electrical transitions had a validated morphology and the threshold level was validated by synchronised video recordings. The electronics demonstrated the possibility of count up to 5000 cells/second for an ideal sample distribution.

The relation between the amplitude and the cell volume was studied using the synchronisation system. The cell transitions selected, can be identified and in addition we are sure that those cells were flowing at the same relative position, because they were at similar focus distance. Under these conditions, we selected 63 transitions for RBCs and 10 transitions for WBCs and 2 transitions for anomalous WBCs. It was detected that the relative amplitude of the electrical transitions is proportional to the cell volume as expected.

Finally, the presented instrumentation is small and cheap. Moreover it has demonstrated very powerful features comparable to existing technologies based on commercial systems.

References:

1. H. M. Shapiro, *Practical flow cytometry*. Practical flow cytometry, Third edition (Wiley Liss, New York, ed. Third edition, 1995).
2. W. H. Coulter, U. S. P. a. T. Office, Ed. (United States, 1953), vol. 2,656,508.
3. D. Huh, W. Gu, Y. Kamotani, J. B. Grotberg *et al.*, Microfluidics for flow cytometric analysis of cells and particles. *Physiological Measurement* **26**, R73 (2005).
4. H. Zhang, C. Chon, X. Pan, D. Li, Methods for counting particles in microfluidic applications. *Microfluidics and Nanofluidics* **7**, 739 (2009).
5. T. Sun, H. Morgan, Single-cell microfluidic impedance cytometry: a review. *Microfluidics and Nanofluidics* **8**, 423 (2010).
6. D. Satake, H. Ebi, N. Oku, K. Matsuda *et al.*, A sensor for blood cell counter using MEMS technology. *Sensors and Actuators B-Chemical* **83**, 77 (2002).
7. O. A. Saleh, L. L. Sohn, An artificial nanopore for molecular sensing. *Nano Letters* **3**, 37 (2003).
8. J. Zhe, et al., A micromachined high throughput Coulter counter for bioparticle detection and counting. *Journal of Micromechanics and Microengineering* **17**, 304 (2007).
9. H. Morgan, T. Sun, D. Holmes, S. Gawad *et al.*, Single cell dielectric spectroscopy. *Journal of Physics D-Applied Physics* **40**, 61 (2007).
10. S. Gawad, L. Schild, P. Renaud, Micromachined impedance spectroscopy flow cytometer for cell analysis and particle sizing. *Lab on a Chip* **1**, 76 (2001).
11. K. Cheung, S. Gawad, P. Renaud, Impedance spectroscopy flow cytometry: On-chip label-free cell differentiation. *Cytometry Part A* **65A**, 124 (2005).
12. H. Morgan, D. Holmes, N. G. Green, High speed simultaneous single particle impedance and fluorescence analysis on a chip. *Current Applied Physics* **6**, 367 (2006).

13. J. H. Nieuwenhuis, F. Kohl, J. Bastemeijer, P. M. Sarro *et al.*, Integrated Coulter counter based on 2-dimensional liquid aperture control. *Sensors and Actuators B: Chemical* **102**, 44 (2004).

14. F. R. E. De Bisschop, in *Instrumentation and Measurement Technology Conference, 2006. IMTC 2006. Proceedings of the IEEE*. (2006), pp. 525-529.

15. S. Zheng, Y.-C. Tai, in *Microtechnologies in Medicine and Biology, 2006 International Conference on*. (2006), pp. 16-19.

16. D. Holmes, J. K. She, P. L. Roach, H. Morgan, Bead-based immunoassays using a micro-chip flow cytometer. *Lab on a Chip* **7**, 1048 (2007).

17. G. Benazzi, D. Holmes, T. Sun, M. C. Mowlem *et al.*, Discrimination and analysis of phytoplankton using a microfluidic cytometer. *IET Nanobiotechnology* **1**, 94 (2007).

18. H. Morgan, N. G. Green, AC Electrokinetics: colloids and nanoparticles. *Herts: Research Studies Press*, (2003).

19. W. Olthuis, W. Streekstra, P. Bergveld, Theoretical and experimental determination of cell constants of planar-interdigitated electrolyte conductivity sensors. *Sensors and Actuators B: Chemical* **24**, 252 (1995).

20. R. Rodriguez-Trujillo, C. A. Mills, J. Samitier, G. Gomila, Low cost micro-Coulter counter with hydrodynamic focusing. *Microfluidics and Nanofluidics* **3**, 171 (2007).

21. R. Rodriguez-Trujillo, O. Castillo-Fernandez, M. Garrido, M. Arundell *et al.*, High-speed particle detection in a micro-Coulter counter with two-dimensional adjustable aperture. *Biosensors and Bioelectronics* **24**, 290 (2008).

22. D. Brokholder, Stanford University (1998).

23. H. P. Schwan, in *Engineering in Medicine and Biology Society, 1990., Proceedings of the Twelfth Annual International Conference of the IEEE*. (1990), pp. 11-11.

24. H. P. Schwan, in *Engineering in Medicine and Biology Society, 1994. Engineering Advances: New Opportunities for Biomedical Engineers.*

Proceedings of the 16th Annual International Conference of the IEEE. (1994), pp. A70-A71 vol.1.

25. N. Watkins, B. M. Venkatesan, M. Toner, W. Rodriguez *et al.*, A robust electrical microcytometer with 3-dimensional hydrofocusing. *Lab on a Chip* **9**, (2009).

26. C. Bernabini, D. Holmes, H. Morgan, Micro-impedance cytometry for detection and analysis of micron-sized particles and bacteria. *Lab on a Chip* **11**, 407 (2011).

Chapter 5 Microcytometer with hydrodynamic focussing

We used the effect of the hydrodynamic focussing by laminar flow to increase the performance of a coplanar electrode system in cell counting. First, we demonstrate that the hydrodynamic focussing increases the sensitivity of the counting system, while providing a useful method to align the cells. Second, we use the hydrodynamic focussing to increase the resolution and detection efficiency in order to evaluate the cell density of a red blood cell population.

5.1. Introduction

As mentioned in previously chapters, the coplanar geometry of electrodes has an important drawback, which is the non-homogeneous electric field distribution inside the channel (see figure 6, chapter 3). In the literature, one can find some alternatives to solve this drawback such as the use of dielectric barriers. These barriers can generate sensing areas where the electric field generated by coplanar electrodes is homogenous (*1*). This approach has been used by Valero and colleagues in microcytometers applications (*2*).

The hydrodynamic focussing consists on using the laminar flow properties to control the dimensions of a main stream within a channel. The section occupied by this main stream is a function of the ratio between the flow rates of the other streams that circulate within the same channel. This focussing, when combining samples with high conductivity with focussing streams of very low conductivity produces the confinement of the electric fields. This confinement produces an effective reduction of the sensing channel section.

The focalisation of the sample stream to generate particle alignment is often used in flow cytometers (*3*). Nieuwenhuis et al. included this alignment system in a microcytometer with the objective of generating enough order and alignment to assure the counting process (*4*). In our laboratory, we have experience in using this principle (*5*) and we also demonstrated the confinement of the electric field by the hydrodynamic focussing (*6*). This confinement of the electric response was used to increase the sensitivity of systems to count CD4+ T cells by Watkins et al. (*7*) and to count *E. Coli* bacteria by Bernabini et al. (*8*). In this work, we also demonstrate the versatility of the lateral and vertical focussing effect to increase the sensing capabilities of a microcytomer.

In this chapter we will show the capabilities of hydrodynamic focusing to enhance particle detection, mainly in two aspects, the sensitivity and the resolution. To this end,

we studied the detection of small particles (< 5 μm) in large section channels and the detection of red blood cells (RBCs) using coplanar electrodes.

5.2. Materials and Methods

The microfluidic devices were fabricated by standard photolithography techniques[3]. The vertical focussing effect was achieved by adding a vertical focusing flow, using an extra inlet on the central chamber. In Figure 5.1, it is represented the final system used. The prototype A was developed to perform lateral and vertical focussing in the adjustable aperture experiment, while prototype B was developed to perform vertical focussing in the red blood cell experiment.

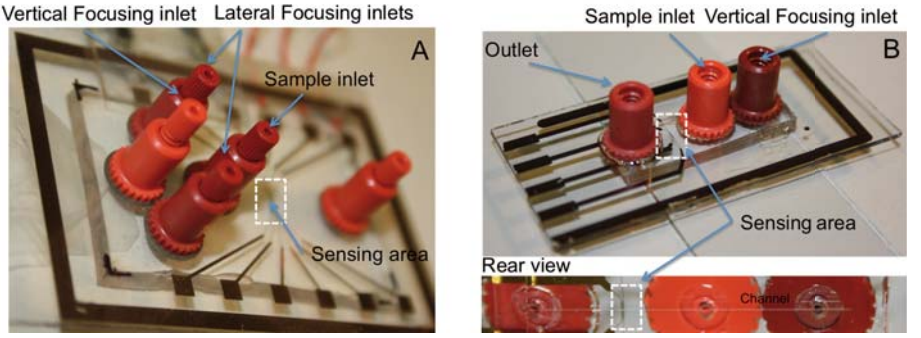

Figure 5.1: Image of the prototypes used. The prototype A is a 2D-focussing system with two lateral focusing inlets and one vertical inlet, to perform an adjustable aperture. Prototype B is a 1D vertical focusing system, developed to achieve a vertical focusing to force cells to travel close to the electrodes.

[3] See materials and methods section in chapter 4, section 4.3.

5.3. Two-dimensional hydrodynamic focussing system to create an adjustable aperture. Application to Yeast cells detection

5.3.1. Introduction

The first prototype of cytometer proposed in Figure 5.1 allows us to demonstrate that the hydrodynamic focussing can create an adjustable aperture. This is used to align cells by creating a focused flow with a cross-section of dimensions similar to the cell (Figure 5.2). When non-conductive solutions are used as focusing streams, the hydrodynamic focusing reduces the effective section of the conductive media by increasing the relation $R_0/\Delta R$. In this equation R_0 is the impedance of the liquid between the sensing electrodes (i.e. without the cell) and ΔR is the increment of the impedance due to the particle. Because of the reduced section, the effects of cell blocking the current lines is more significant in the focusing case than in the non-focusing case, thus enhancing the system sensitivity.

This system can provide the detection of samples with particles of different sizes without the need of changing the channel geometry. As a prove of concept, we demonstrated the successful detection of small yeast cells 5 μm in size within a channel with a section 100 μm wide by 43 μm high.

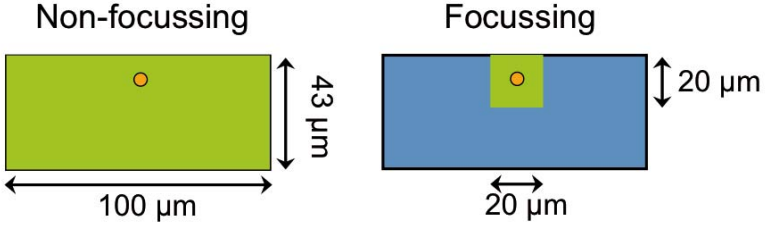

Figure 5.2: Schematic image of a small cell in front a big section channel (100 μm by 43 μm), under no focusing conditions (left). The volume ratio of the cell in front the conductive buffer is small. Under focusing conditions (right) the cross section of the conductive media is comparable to the cell size.

4.3.2. Methods

In this section we used the set up represented in Figure 5.3. We build up a device with channels 100 μm wide and 43 μm high for the yeast cell detection experiments (section 4.3.3.1) and a device with channels 180 μm wide and 65 μm high for the 20 μm polystyrene particle experiment (section 4.3.3.2). The electrodes are coplanar with dimensions 40 μm in width and separated 40 μm. The hydrodynamic focusing was achieved by using three focusing streams, two lateral inlets (Figure 5.3a) and one vertical inlet (represented in (Figure 5.3a) and (b)). This device geometry results in a 2D constriction of the section of the sample stream.

The sample flow (Q_S) is the sample flow rate, (Q_V) is the vertical focussing flow and (Q_{L1}, Q_{L2}) the lateral focusing flows. The relation between central flows (Q_S, Q_V) and the lateral flows (Q_{L1}, Q_{L2}) controls the width (w_s) of the aperture. The relation between the sample flow (Q_S) and the vertical focusing flow (Q_V) controls the vertical size (h_s) of the adaptable aperture of the micro-Coulter counter (Figure 5.3b).

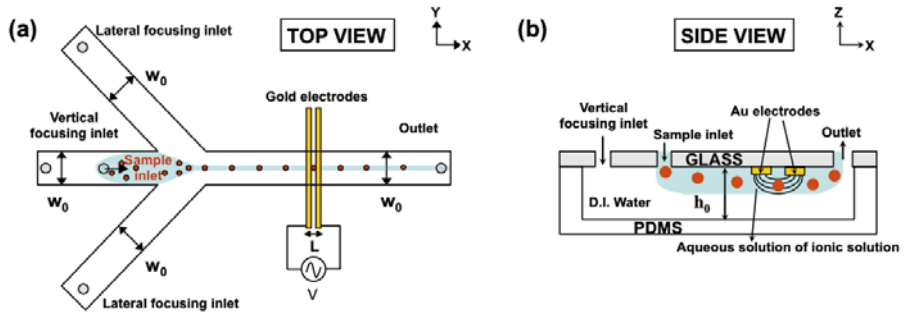

Figure 5.3: Scheme of a microcytometer with hydrodynamic focusing. (a) top view and (b) side view of a section cut along the central channel.

4.3.2. Characterisation of focusing

The 2D fluid focusing capabilities of the device have been characterised by means of confocal microscopy (Leica SP2) measurements. In these experiments, all inlets were

filled with deionised water and the sample input flow was dyed with a fluorescent marker (Fluorescein) in a concentration of approximately 0.5 mg/ml.

The flux rate in the lateral focusing channels was fixed to 10 µL/min (Q_{L1}=Q_{L2}=10 µl/min) for all the experiments, and the sample flow and the vertical focusing flow were equal and varied from 20 to 1 µL/min, which resulted in different focalisation conditions. In Figure 5.4, we show confocal microscopy images of a section transversal to the direction of the flux in the outlet channel for four different focalisation conditions.

To estimate the lateral and vertical sizes of the cross-sectional area of the focalized region, we can use the following simple relationships (*5*):

$$h_S = h_0 \frac{Q_S}{Q_S + Q_V} \qquad \text{Equation 1}$$

$$w_S = w_0 \frac{Q_S + Q_V}{Q_S + Q_V + Q_L} \qquad \text{Equation 2}$$

Where Q_L=Q_{L1}+Q_{L2} is the total lateral flux, and h_0 and w_0 are the physical height and width of the channel (see Figure 5.3). The focalized sample height h_s is approximately the half of the total height h_0 for all images in Figure 5.4 as it can be derived from Equation 1.

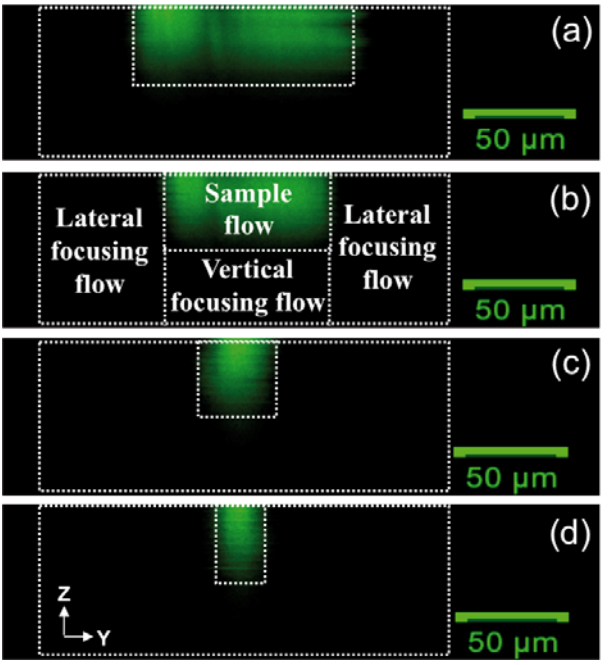

Figure 5.4: Confocal microscopy images of a transversal section of the channel where the focusing is achieved. The flow rates of the lateral channels are 10 µL/min for all the images. While the fluxes Q_S and Q_V were fixed at: 20 µL/min (a), 10 µL/min (b), 2 µL/min (c) and 1 µL/min (d). (6)

The electrical characterisation of the hydrodynamic focusing was done by using in the sample inlet a NaCl solution with a conductivity of 0.15 S/m, while in the focusing inlets (two lateral and vertical) we used deionised water with a measured conductivity of 0.4 mS/m. Figure 5.5 shows the measured resistance as a function of the total central flux rate Q_{CT} (Q_S+Q_V) when different focalisation conditions were set. Each of the curves corresponds to a given vertical focalization condition. The squares represent the case in which no vertical focusing (Q_V = 0) is applied. The measured resistance (symbols) obtained by a commercial impedance analyser (Agilent 4294A) were compared to an estimated value R_S (lines) calculated with equation 3 for the conductive stream section. h_s and w_s were calculated by equations 1 and 2.

$$R_S = \alpha \frac{L}{\sigma h_S w_S}$$ Equation 3

Where L is the distance between electrodes, σ is the conductivity of the stream and α is a geometrical factor adjusted (*6*)

As it can be seen in Figure 5.5, for a given width of the focused sample flow, a higher degree of vertical confinement implies a higher value of the measured resistance. On the other hand, for a fixed degree of vertical confinement, a reduction in the width of the focused flow implies also an increase in the electrical resistance.

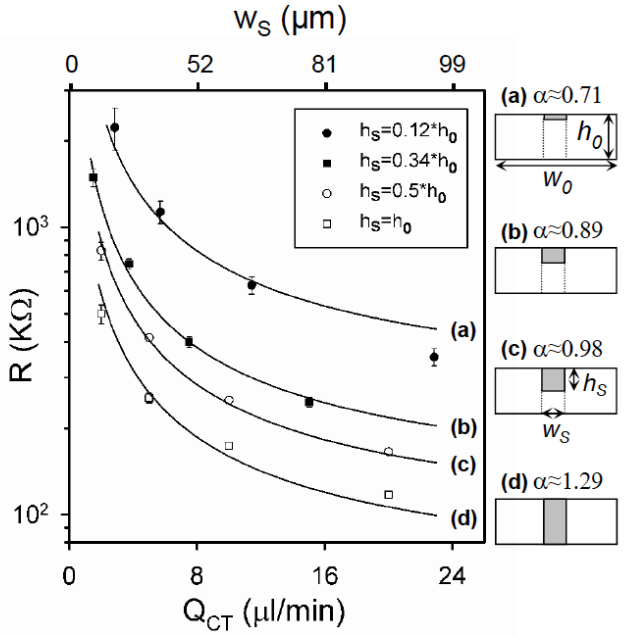

Figure 5.5: Electrical resistance measured between two electrodes by its dependency with the total central flow $Q_{CT}=Q_S+Q_V$. The experimental measurements (symbols) are compared to the expected behaviour derived from using equation 3. (6)

4.3.3. Results and discussion

4.3.3.1. Increase sensitivity

We used 20 μm polystyrene particles to demonstrate that the hydrodynamic focusing increase the sensitivity of a microcytometer with coplanar electrodes. The focusing condition corresponds to an aperture 32 μm high and 25 μm wide, while the non-focused condition implies an aperture 180 μm wide and 65 μm high.

The effect of the confinement produced by the focusing can be shown in a more direct way by comparing the response of our device with two-dimensional hydrodynamic focusing and with only one-dimensional hydrodynamic focusing. Figure 5.6 shows the statistical distribution of the amplitudes of the detected peaks for the 1D and 2D-focusing experiments.

Distributions in Figure 5.6 were fitted to normal curves (solid lines). The means of the distributions are 2.8 and 4.4 V for the 1D and the 2D-focusing cases, respectively. This shows that when particles are detected in the 2D-focusing device, they give rise to signals of higher amplitude (magnified by a factor of 1.6 for the focusing condition chosen) with respect to particles detected in a 1D-focusing experiment. Watkins et al. (*7*) got similar results with a device also using coplanar electrodes with a commercial lock-in amplifier.

This result is a consequence of the fact that the resistive response of the device was confined to the sample fluid volume, which was smaller in the case of the 2D-focused experiments than in the 1D case.

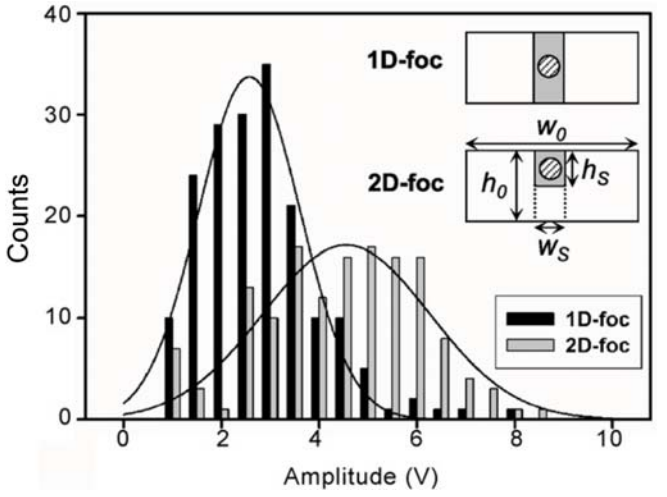

Figure 5.6: Comparison of the histograms for one and two-dimensional (for the case hs = 0.5 h) hydrodynamic focusing transition amplitudes. The calculated means for the distributions are 2.8 and 4.4 V, respectively. They have been fitted to normal distributions (solid lines).

These results demonstrate that we can confine the sample flux in the lateral and vertical directions to the desired size by applying the appropriate flux focusing conditions. This two-dimensional focusing gives an exceptional versatility to our device, because we can adapt the cross-sectional area of the sample flow to the size of the particles to be analysed, thus being able of detecting particles with a broad range of sizes with the same device.

4.3.3.2. Detection of *Yeast cells*

Yeast cells (*Saccharomyces cerevisiae*) were incubated for 72 h at 30ºC in Sabouraud Broth, and then washed and suspended in an aqueous solution of NaCl 27 g/l with a measured conductivity of 2.87 S/m. The focusing inlets were filled with deionised water with a measured conductivity of 0.4 mS/m. The flow rates and geometry used in this section allow an effective cross-sectional area of the sample stream of 20 μm by 20 μm.

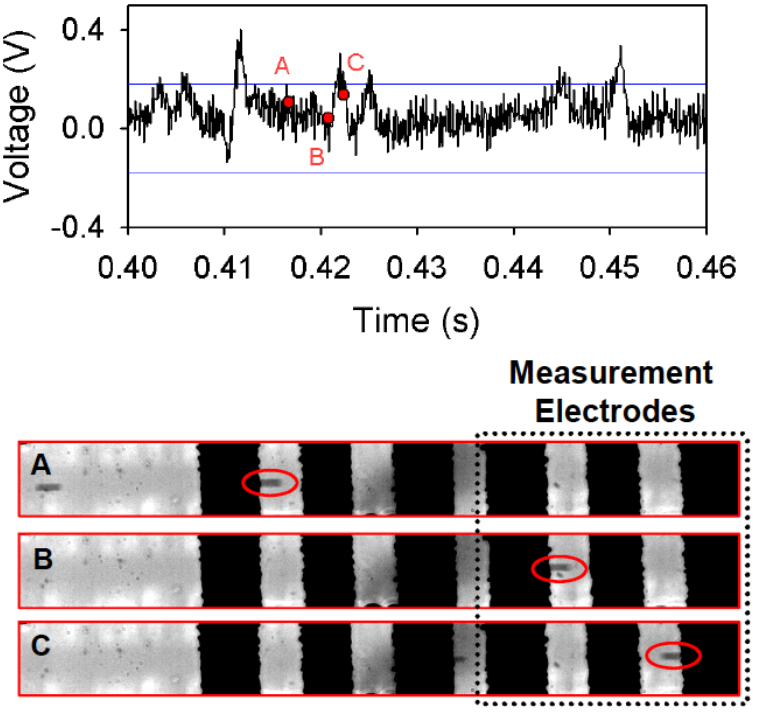

Figure 5.7: Synchronised electrical and optical measurements of the crossing of yeast cells. On the top view there is represented the electrical acquisition signal corresponding to the transitions of seven cells during 60ms. The horizontal blue line indicates the threshold used for automatic detection. The bottom view is the synchronised images of three instants in the evolution of the position of a cell. These images instant are represented as red dots on the electrical signal.

The results are shown in Figure 5.7. The top plot presents 60 ms of the voltage acquisition. Cells transitions correspond to the seven spikes observed in the signal over the small background noise. The passage of the all seven cells was verified using the simultaneously recorded video images. The bottom picture at Figure 5.7 shows three images where one focused cell flows from the left to the right at the time points A-C, indicated on the electrical signal and optical images. In this case the transition times were around 3ms, which was consistent with flow rate conditions.

The detection and counting of particles with a size equivalent to the 5% of the total section of the channel was demonstrated. This means that the system is able to confine the electrical signal by focusing. When the confinement of the conductive stream is close to the cell size, the particle is able to generate a significant increment on the impedance of the fluid, resulting on an electrical transition. Thus, the electronics and optical systems can successfully detect the yeast cells.

5.4. Hydrodynamic focusing to enhance RBCs counting with coplanar electrodes

5.4.1. Introduction

The second experiment proposed to study the effect of the hydrodynamic focusing is to evaluate the cell concentration of red blood cells with a microCoulter counter using coplanar electrodes. We have studied if the hydrodynamic focusing could enhance the sensitivity and reliability of RBCs counting.

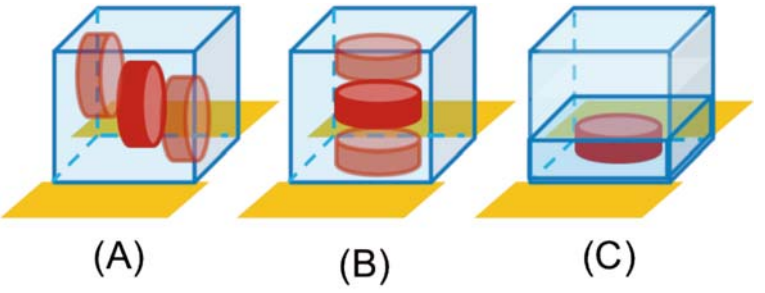

Figure 5.8: Schematic representation of the positions that red blood cell could take inside a channel of 10 μm width by 10 μm height. Even when the channel is designed to be similar to the cell size, the particular shapes of these cells allow them to take several positions and different orientation in front of the electrodes, represented in the schemes (a) and (b). This variation on the relative position to the electrodes could generate a wide deviation on the amplitudes obtained and even hide some counts due to their very low amplitudes. The focusing is used to orientate and force the cells to travel close to the electrodes as it is represented in (c).

However, RBCs have a characteristic shape which generates a particular problem with microcytometer devices developed with co planar electrodes. The RBCs morphology can be described as disk like-shaped with a low depression on the centre. The size is considered around 7 μm, which is the size of its major dimension, and the height is around 2,5 μm. Thus, a channel section of 10 μm^2 seems a good option to obtain optimal results in terms of cell impedance increment. However, in a channel section of 10 μm^2, a red blood cell could take several positions as it is represented in schemes (a) and (b) of Figure 5.8. This variability on the cell position with respect to the electrodes could then generate dispersion on the amplitude of the electrical transitions.

The hydrodynamic focusing is tested in this chapter to determine its ability to force RBCs to be oriented and closer to the electrodes as it is represented in the image (c) of Figure 5.8, in order to reduce the deviation of the obtained amplitudes of the electrical transitions.

The dispersion in red blood cells counting is related to two main reasons: the cell orientation and its position with respect to the electrodes. Figure 5.9 represents an image obtained by the stitching of 4 contiguous images of the same red blood cell travelling over a sensing area in channel of 10 μm^2. In these snapshots it is possible to see how the cell is changing its orientation while it is flowing along the channel.

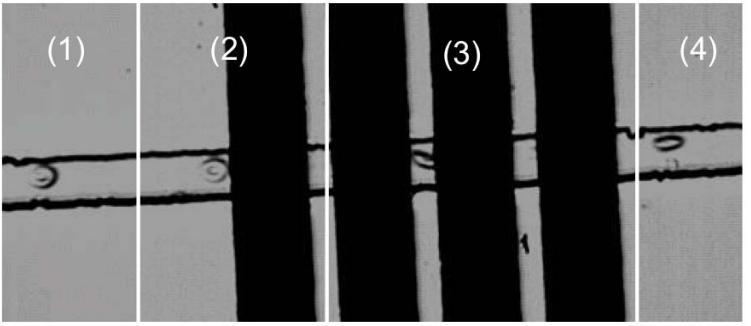

Figure 5.9: Screening image of 4 correlate consecutive frames of the same RBC crossing the sensing area in a micro device of cross-section of 10μm width by 10μm height. In the sequence it is possible to see how the cell is changing its orientation and position inside of the channel.

In Figure 5.10 it is represented a COMSOL calculation of the current on the two electrode pairs and the effect produced by different disk orientations. In the figure is presented two main possibilities. The case A is when the major dimension of the disk is oriented into the flow direction. The case B represents the disk with its major dimension orthogonal to the flow direction. The geometry used on this simulation was a channel height of 10 μm with a coplanar electrode of 20 μm in width separated 10 μm. The disk is 7 μm in its major dimension and 2.5 μm in its lower dimension. The solid lines between electrodes represent the electric field density. As it was expected, the electric field is mainly concentrated close to the electrodes. The current density between electrodes pairs was calculated by integrative COMSOL tools. The obtained values are shown below each pair of electrodes. The difference in current between both electrode pairs is proportional to the output of the electronic instrumentation in use and determines the amplitude of the electronic transitions.

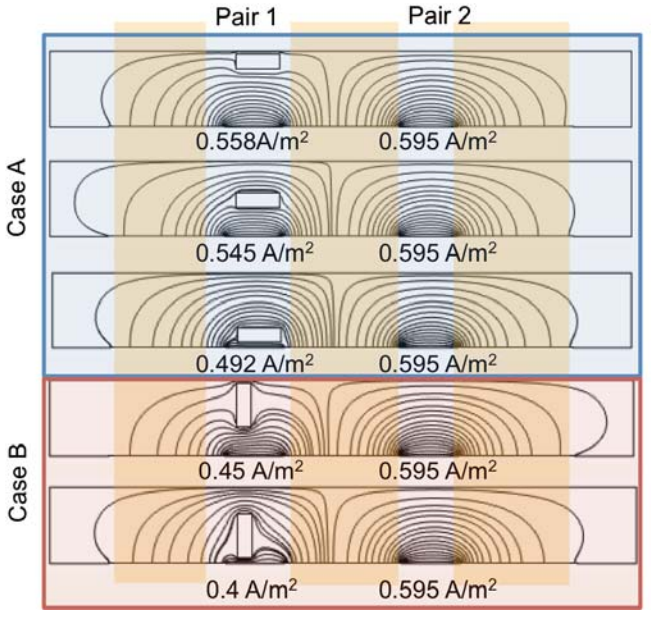

Figure 5.10: Comparison of the effect of increasing impedance of a disk cell model as an opaque element to the current lines. The COMSOL calculated values of the total current between electrode pairs present the real effect of the cell position and orientation to the co planar electrode geometry. Case A represents a disk particle with the major dimension oriented on the direction of the flow, while the case B represents a disk particle with the major dimension orthogonal to the flow direction.

Case A in Figure 5.10 demonstrates that the cell position over the electrode is important to generate different impedance effects by the same cell geometry. In case A, the difference between currents is maximal when the disk is near to the electrodes. In case B, the difference between the relative positions is smaller and all the currents are lower than those corresponding to the three positions in case A. Therefore, the position of cells in the channel and their orientation over the electrodes determine the amplitude of the electrical transitions.

5.4.2. Methods

In Figure 5.11 is represented the design of the system with the vertical focusing achieved by two different inlets on the same channel. The channel has a section of 10 μm in width and 8.5 μm in height, and the electrodes are 20 μm wide separated by 10 μm. When the hydrodynamic focusing was used to reduce the effective section of the sample stream, the effective impedance of the system is increased, as it was demonstrated in the previous characterisation (Figure 5.5).

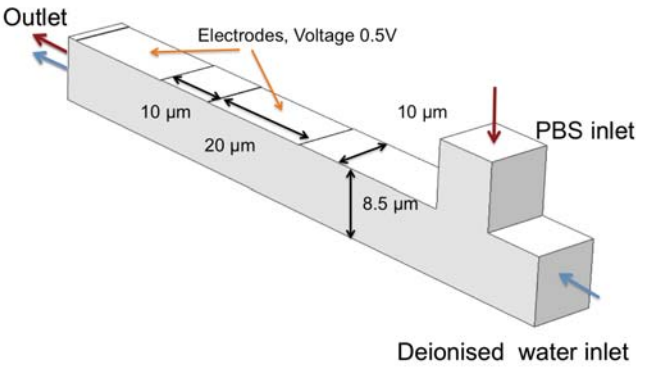

Figure 5.11: Schematic representation of the microfluidic device used to achieve the vertical focusing in a small channel of 8,5 μm height and 10 μm in width. The electrodes used are 20 μm width, and the electrode pairs were separated by 10 μm.

5.4.3. Characterisation of vertical focusing

The hydrodynamic focusing was also electrically demonstrated by using PBS solution (measured conductivity of 1.6 S/m) in the sample inlet, and deionized water (measured conductivity of 0.4 mS/m) in the vertical focusing. The impedance was measured by an impedance analyser (Agilent 4294A).

Figure 5.12 represents the differences in the impedance spectroscopy at several focusing conditions with the same bridge configuration. Increasing the flow rate of the focusing stream (Q_V), the effective confinement of the conductive solution induces an

increment of the impedance. The variability of the equilibrium of the Wheatstone bridge of the detection board was also studied. Figure 5.12 represents the signal obtained at the output of the bridge for a fixed equilibrium position of the Wheatstone bridge[4].

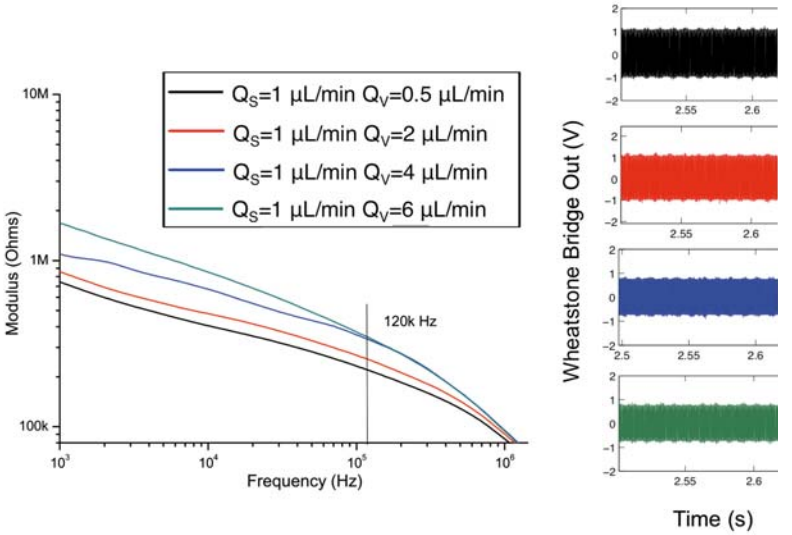

Figure 5.12: Left: Electrical impedance measured from a pair of electrodes at different hydrodynamic conditions. The Q_S is the flow rate applied to the simple inlet, in this case filled with a PBS solution with a measured conductivity of 1.6 S/m. The Q_V is the flow rate applied to the vertical focusing inlet, filled up with deionised water with a measured conductivity of 0.4 mS/m. Right: The represented signals indicate the signal acquired from the output of the Wheatstone bridge for the different flow conditions with a fixed position of the potentiometers used to build the two branches of the bridge (see Figure 13 in chapter 4).

The increment of the impedance by increasing the focusing condition has a direct effect in the equilibrium of the bridge, reducing the amplitude of the signal obtained. We demonstrated that there is a strong relation between the equilibrium condition of the bridge and the amplitude resultant of the detected particle transitions.

[4] See Wheatstone bridge section in chapter 4, section 4.3.3.1.

5.4.4. Results and discussion

In this experiments red blood cells (RBCs) were obtained from whole blood from a human donor. The plasma and the white blood cells were separated by centrifugation techniques and the remaining pellet of RBCs was re-suspended in PBS buffer and washed by centrifugation three times. Then, we prepared a controlled suspension with a density around 10^7 cells per ml, determined by a Neubauer chamber.

We used two different focusing conditions: first, the sample flow was fixed at 1 μL/min while the focusing flow rate was fixed at 0.1 μL/min. We consider this as a non-focalising condition. In this case, the theoretical sample height, h_s, was only reduced from 8.5 μm to 7.8 μm. The second focalisation condition was fixed at 1 μL/min for the sample stream and 1 μL/min for the focusing stream. Under this condition the effective cross-section was reduced to 4.2 μm, which means a height smaller than the main diameter of RBCs. This will force them to become oriented and to transit close to the electrodes (Figure 5.8c). The automatic acquisition of particles was programmed with a threshold of 0.05 V for both conditions.

The signal obtained under the first hydrodynamic conditions (1:0.1 μL/min) is plotted in Figure 5.13. The output signal from the Wheatstone bridge (inset) was very stable, and the amplitude value was always around 0.06 V. We can easily compare the density of cells contained in the sample dilution with the number of cells counted by the system under non-focusing conditions. Three independent experiments gave as result: 255 and 285 particles counted in two records of 4 seconds, and 529 particles counted in a record of 8.8 seconds. Thus, in a total of 16.8 seconds 1069 electrical transitions were counted. This means a ratio of 63±10 particles per second. The flow condition of 1 μL/min means a cell density of approximated 3789±600 cells per minute, which gives a cell density of approximately $3.7\pm0.6\cdot10^6$ cells/mL. The cell density detected by the counting process is roughly 3 times lower than the theoretical density of the prepared cell suspension.

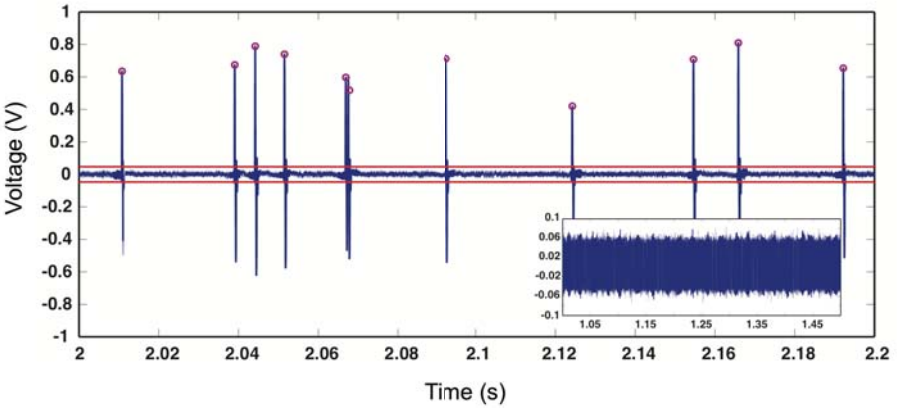

Figure 5.13: The electrical signal obtained from the instrumentation of the transitions of red blood cells diluted in PBS when a flow rate of 1 μL/min was fixed for the sample flow while the focusing flow rate was fixed at 0.1 μL/min. The inset shows the signal obtained directly from the Wheatstone bridge, the amplitude of the raw data before the demodulation process is of 0.06 V, The red lines indicate the threshold used for automatic detection of transitions (0.05 V), and the red circles indicate the transition detected and the value in V of the amplitude considered.

On the other hand, Figure 5.14 shows an example of the acquisition by the system under the focusing conditions of 1:1 μL/min. The bridge output indicates that mean amplitude value is 0.06V, very similar to the one found for the non-focusing case. As the bridge equilibrium is maintained we could consider that the changes in the amplitudes are not due to changes in the impedance of the bulk solution. Then, the differences of the detected voltages are considered related to the position of the cells.

The cell counting ratio under the focusing condition of 1:1 significantly increased with respect to the non-focusing condition. In this case, we counted a total of 2781 electrical transitions in a 16.8 seconds record. As before, these were detected in several experiments: 707 and 623 particles were counted in two periods of 4 s each, and 1451 particles were detected in a period of 8.8s. This counting means a ratio of 165±10 particles per second. Such a ratio under a flow condition of 1 μL/min, means a cell

density in solution of around $9.9\pm0.6\cdot10^6$ cells/mL, which is in complete agreement with the density expected from the sample.

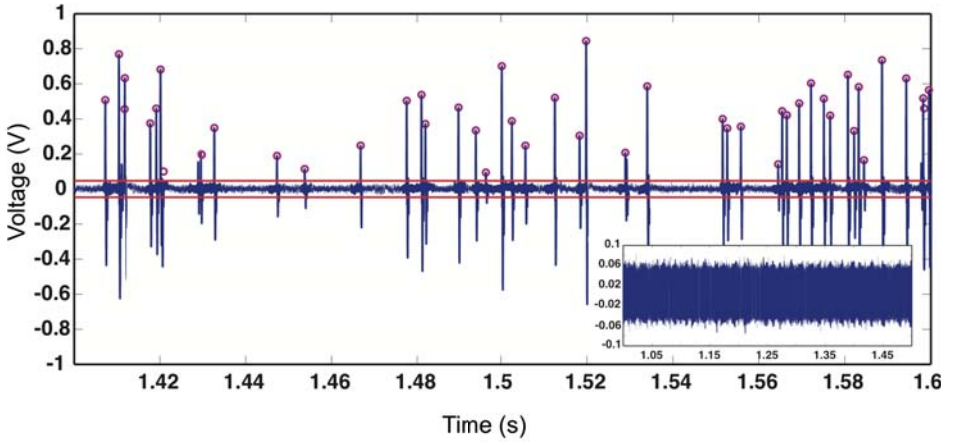

Figure 5.14: The electrical signal obtained from the instrumentation of the transitions of red blood cells diluted in PBS when a flow rate of 1 μL/min was fixed for the sample flow while the focusing flow rate was fixed at 1 μL/min. The inset shows the signal obtained directly from the Wheatstone bridge, the amplitude of the raw data before the demodulation process is around 0.06 V. The red lines indicate the threshold used to the automatic detection of transitions (0.05 V), and the red circles indicate the transition detected and the value in V of the amplitude considered.

Figure 5.15 represents the distribution of the voltage amplitudes for both cases. The black bars are the distribution of amplitudes for the case of non-focusing (1:0.1). In this case the voltages have a distribution with a mean value of 0.57 V and a maximum value of 0.65 V. Almost the 22% of the transitions detected had this maximum amplitude value. The red bars indicate the distribution of the voltage amplitude for a focusing rate 1:1. In this case the distribution was shifted to the low amplitudes, where the maximum number of events takes place, and the mean value was shifted to 0.33 V.

Due to the non-variation of the bridge output in both cases, we consider that the variation of the amplitudes in the cell population is directly related to the cell position

and orientation. Under focalisation conditions, the number of detected cells increases significantly (3 times more), and the new cell transitions mainly occur with low amplitudes. This lead us to think that these cells, which were not detected under non-focusing conditions, were now detected because they are closer to the electrodes.

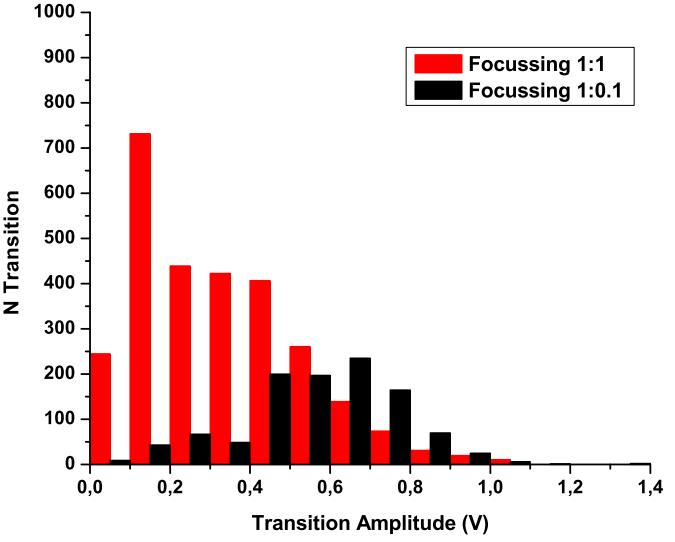

Figure 5.15: Histogram of the cell counts distribution by the amplitudes detected. Red bars indicate the distribution for the focusing case, while the black bars indicate the amplitude distribution for the non-focused case. It is shown that there is a displacement on the distribution.

Moreover, in Figure 5.15 is possible to detect differences in the distribution of transitions with high amplitudes, over 0.6 V between the focussing and non-focussing conditions. Under the non-focussing condition, the number of cells that rise high amplitudes is larger than in the focussing condition. We related this to the cell orientation, as the sample stream is reduced to 4.2 μm, this reduces the possible cell orientations as seen in the case of Figure 5.10A.

In this comparison we neglected the death volumes of the fluidic connections and the possible variations on the flow velocity. We only take in account the variability of

trajectories that the RBCs could take, and the cell orientation. Then, we could conclude that in non-focusing conditions, we are losing a large number of cells because they are travelling in flow planes closer to the top of the channel, far away from the electrodes.

5.5. Conclusion

The hydrodynamic focusing was used in a microfluidic system to increase its sensitivity and efficiency as a cell counter. The hydrodynamic focusing provides the system with an adjustable aperture in two dimensions.

In addition, the sensitivity of the device is increased since its resistive response is concentrated within the small sample flux defined by the aperture. We have experimentally proved that two-dimensional focusing increases the power of detection of the device by a factor of 1.6 with respect to an identical device with only one-dimensional hydrodynamic focusing. The increased efficiency of the system by using the hydrodynamic focusing, allow us to count and extrapolate the real cell RBCs density of the samples. Moreover, the focusing reduces cell position and orientation within the channel increasing the resolution of the microcytometer.

References:

1. N. Demierre, T. Braschler, P. Linderholm, U. Seger *et al.*, Characterization and optimization of liquid electrodes for lateral dielectrophoresis. *Lab on a Chip* **7**, 355 (2007).
2. A. Valero, T. Braschler, P. Renaud, A unified approach to dielectric single cell analysis: Impedance and dielectrophoretic force spectroscopy. *Lab on a Chip* **10**, 2216 (2010).
3. H. M. Shapiro, *Practical flow cytometry*. Practical flow cytometry, Third edition (Wiley Liss, New York, ed. Third edition, 1995).
4. J. H. Nieuwenhuis, F. Kohl, J. Bastemeijer, P. M. Sarro *et al.*, Integrated Coulter counter based on 2-dimensional liquid aperture control. *Sensors and Actuators B: Chemical* **102**, 44 (2004).
5. R. Rodriguez-Trujillo, C. A. Mills, J. Samitier, G. Gomila, Low cost micro-Coulter counter with hydrodynamic focusing. *Microfluidics and Nanofluidics* **3**, 171 (2007).
6. R. Rodriguez-Trujillo, O. Castillo-Fernandez, M. Garrido, M. Arundell *et al.*, High-speed particle detection in a micro-Coulter counter with two-dimensional adjustable aperture. *Biosensors and Bioelectronics* **24**, 290 (2008).
7. N. Watkins, B. M. Venkatesan, M. Toner, W. Rodriguez *et al.*, A robust electrical microcytometer with 3-dimensional hydrofocusing. *Lab on a Chip* **9**, (2009).
8. C. Bernabini, D. Holmes, H. Morgan, Micro-impedance cytometry for detection and analysis of micron-sized particles and bacteria. *Lab on a Chip* **11**, 407 (2011).

General conclusions

In this thesis we studied the electric fields possibilities to manipulate and sense biological samples in micro and nanofluidic environments with the aim of generating tools oriented to form a Point of care device.

We studied, **in Chapter 2**, the separation mechanism by electrophoresis of DNA molecules by its molecular weight in nanochannels. We investigated the movement of λ-DNA molecule using alternate electric fields to investigate the separation mechanism in nanochannels. The obtained results of mobility, the detection of preferential pathways, the movement of the molecules and the behaviour of the molecule with the AC electric fields lead us, to reject the hypothesis of the dielectrophoresis influence on the molecule movement. The results were compatible with a small network of obstacles inside the nanochannel that interact with the molecule. The best candidate to produce this network behaviour is the PVP accumulation on the channel walls.

In **Chapter 3**, we proposed a new system, by using dielectrophoresis, to separate and manipulate cells under continuous flow conditions, which is an important benefit to integrate this tools in a POC device. We used dielectric barriers to generate local maxima of electric field, which perform a dielectrophoretic barrier, which competes with the dragging forces inherent to the flow conditions. This competition was used to discriminate between cell sizes. The advantages of our device in front of other examples are the dimensions of the separation area, and the efficiency of the dielectrophoretic barriers designed.

In **Chapter 4**, we presented an instrumentation that was able to sense the variation of impedance generated by the cell. The system performs a suitable detection of particles for a high throughput cell cytometry applications, being able to distinguish cells sizes showing a linear response with the cell volume. The microfluidic system used consists in three coplanar electrodes geometry.

In **Chapter 5**, we used the hydrodynamic focussing as an essential tool to improve the performance of this coplanar electrode geometry. This focussing method aligns and orientates cells obtaining an increment of the counting sensibility and resolution.

Resumen en castellano

1. Introducción

Durante este último siglo se ha producido una revolución tecnológica e industrial en la microelectrónica y la computación. Junto con esta revolución, se han ido desarrollado las técnicas y las plataformas tecnológicas necesarias de microfabricación para esta tecnología. Hoy en día, estas técnicas de fabricación se están aplicando a diferentes ámbitos y materiales, lo que nos ha llevado a la aparición y el desarrollo de diferentes sistemas electromecánicos miniaturizados, denominados MEMS (sistemas micro electromecánicos, en sus siglas en inglés). Cuando estos sistemas MEMS se utilizan para contener o mover fluidos (sistemas fluídicos), utilizamos el termino de microfluídica.

Las aplicaciones de los sistemas MEMS son muy amplias, en concreto, los dispositivos microfluídicos han alcanzado gran relevancia en el ámbito de la biomedicina. La combinación de los métodos de microfabricación con la utilización de materiales biocompatibles, ha abierto una nueva y relevante perspectiva en la fabricación de sistemas *in vitro* miniaturizados.

La miniaturización de estos sistemas significa una importante mejora sobre otros dispositivos, debido a que, gracias sus reducidas dimensiones, trabajan con volúmenes de muestra reducidos, lo que además implica la disminución del volumen de reactivos necesarios, así como el aumento de la velocidad de procesado (*1*). A partir de estos sistemas, se deriva un nuevo concepto de dispositivo, los llamados Lab on a Chip, cuyo objetivo final es reproducir en pequeña escala un proceso estándar de laboratorio (*2, 3*).

El concepto de Lab on a chip (LOC) pretende que los sistemas o dispositivos sean completos e independientes, compactos y automatizados. Estos sistemas deben significar una mejora sobre las eficiencias que ofrecen los sistemas de laboratorio, así como reducir los costes tanto de fabricación como de procesado. Además, es importante que los ensayos se puedan realizar sin necesidad de las condiciones de trabajo propias de un laboratorio y del personal altamente cualificado.

Estas características son una oportunidad real y factible de generar sistemas apropiados para la atención primaria. Los sistemas orientados para la atención primaria, o *point of care* en inglés (POC), se definen como aquellos dispositivos que proporcionan un resultado analítico verídico en entornos cercanos al paciente, como entornos de atención primaria. Estos sistemas tienen como objetivo principal apoyar al diagnóstico, normalmente basado en la sintomatología, aportando un diagnóstico más fiable y barato.

Este tipo de dispositivos son de vital importancia en países en desarrollo, donde existe una importante carencia de recursos y facilidades como laboratorios apropiados, equipamiento, así como del personal adecuado. Los sistemas POC aportan la posibilidad de realizar estudios analíticos en zonas económicamente deprimidas. En países desarrollados, donde el control de los costes de la sanidad pública es prioritario, y además el envejecimiento de la población implica un aumento de las enfermedades crónicas, estos dispositivos pueden aportar soluciones y mejoras para el sistema y el conjunto de la población, aportando una mayor velocidad y calidad en la asistencia primaria y de emergencia, además de una reducción de costes en analíticas convencionales (*4, 5*). Los requerimientos que han de cumplir estos sistemas para poder ofrecer respuestas a estas necesidades han sido detallados y descritos por varios autores (*4-6*).

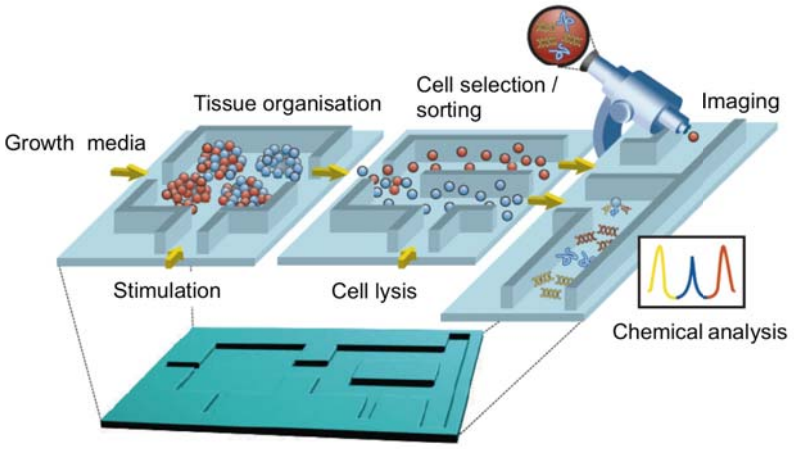

Figura 1: Esquema representativo de un sistema modular idealizado para el análisis celular. En el esquema se muestra 3 sistemas o módulos independientes e interconectados. Primero hay una zona de cultivo y estimulación celular, del que se obtiene la muestra de interés, posteriormente una etapa de separación y selección de las células de interés que, posteriormente, son lisadas para obtener el contenido. Finalmente, la parte analítica en la que se puede estudiar la composición molecular mediante técnicas electroquímicas o análisis celular.

La mayoría de los métodos analíticos para aplicaciones biológicas, se llevan a cabo en líquido y precisan de varios pasos. Estos pasos normalmente consisten en los diferentes procesos necesarios para la preparación o purificación de la muestra obtenida. Los diferentes procesos en que consta todo el experimento necesitan diferentes condiciones y herramientas, y en general, se suele enfocar el diseño en una serie de pasos o módulos con los que alcanzar el resultado analítico, como se puede ver en el esquema de un micro sistema idealizado en la Figura 1.

Uno de los sistemas de análisis más utilizado como herramienta de diagnóstico, para la detección de patógenos, es el análisis genético (*7*). Los más utilizados son los sistemas de electroforesis de DNA tanto en aplicaciones de detección como en aplicaciones de secuenciación (*8*). La separación de DNA mediante electroforesis, se suelen realizar en capilares o geles. La incorporación de los geles a sistemas microfluídicos cerrados,

suele ser cara y compleja, y además con una baja reproducibilidad. Por lo tanto, muchos autores plantean sistemas de separación más baratos orientados a generar estructuras que emulen a los geles, para realizar una separación de DNA por tamaño (*9, 10*).

Otro de los grandes sistemas de detección en aplicaciones biomédicas es la citometría de flujo. Estos sistemas tienen una gran versatilidad, más allá del simple recuento celular y, en combinación con sistemas de fluorescencia, pueden proporcionar información sobre la composición de la membrana, estructura y composición de la célula. Estos sistemas están muy extendidos en laboratorios para realizar un extenso número de análisis (*11*). Además de la detección óptica, existen otros sistemas basados en detección eléctrica mediante efecto Coulter (*12*).

La miniaturización de sistemas de recuento basados en campos eléctrica está muy estudiada y en la literatura existen ejemplos relevantes (*13*). Pero la mayoría de los sistemas de instrumentación utilizados son sistemas de análisis de impedancia comerciales o amplificadores lock-in. Estos sistemas comerciales resultan ser soluciones complejas y caras que difícilmente pueden ser integradas en un dispositivo miniaturizado.

Además de los sistemas de detección, uno de los módulos más importantes para este tipo de dispositivos es la capacidad de manipular y separar la muestra celular en el interior de los dispositivos. Existen herramientas de manipulación celular a escala micro como son, por ejemplo, las pinzas ópticas y magnéticas (*14, 15*), que requieren de complejos sistemas de control e instrumental. Por otro lado, los micromanipuladores y micropipetas no son óptimos para trabajar en sistemas cerrados (*16*). Como alternativa a estos sistemas, los campos eléctricos se han convertido en una opción muy útil y versátil (*17*).

En esta tesis doctoral nos planteamos aportar soluciones a estos tres puntos en concreto, lo que implica la utilización de campos eléctricos como herramienta principal.

2. Electroforesis, separación de ADN.

2.1. Introducción

La movilidad electroforética de las moléculas de ADN en solución es independiente de su peso molecular (*18*). Lo que implica que la identificación del peso molecular de una molécula de ADN mediante su carga, que se utiliza en la secuenciación, no es posible. Entonces para realizar la secuenciación o identificación de patógenos se requiere de la utilización de técnicas como la electroforesis en gel (*8*). Siendo la fricción con el gel, la responsable de generar una movilidad que si dependa de su peso molecular.

En la actualidad, podemos encontrar algunos ejemplos de sistemas que implementan estructuras periódicas con pequeños nanocanales que conectan pocillos de mayores dimensiones. Estos sistemas han sido capaces de separar moléculas en función de su tamaños, siguiendo los modelos de régimen de separación Ogston y separación entrópica (*19, 20*). Otra aproximación interesante es la emulación de un gel mediante la estructuración de una matriz de pilares de alta densidad (*21*), con este tipo de sistemas se ha podido reproducir la separación de moléculas de ADN por tamaño.

La reducción de la sección de un canal a la nano escala también es una aproximación válida para la separación por tamaño de moléculas de ADN. Pennathur y colaboradores (*22*) demostraron que era posible separar moléculas de entre 10 y 100 pares de bases en canales de 100 nm. Por otro lado, Cross et al. (*23*), obtuvo también resultados de separación, de moléculas mucho mayores, entre 2000 y 1000 pares de bases, en canales de 19 y 70 nm. Los dos relacionaron la capacidad de separación de los nanocanales con la interacción de la molécula de ADN con la superficie de las paredes.

En un trabajo posterior, Salieb-Beugelaar et al. (*24*) investigaron el movimiento de las moléculas en el interior de un canal de 20 nm. En este trabajo, se demuestra la posibilidad de separación de las moléculas de ADN de 48000 y 2800 pares de bases. Pero además, descubrieron que existe una dependencia de la movilidad de la molécula

y su movimiento con la intensidad de campo eléctrico aplicado. En este trabajo se reportan dos tipos de movimiento. Un movimiento que se describe como fluido, que la movilidad se incrementa cuando la intensidad de campo aumenta. Y otro movimiento en el que se describe como intermitente, en el que la movilidad se ve reducida dramáticamente. El movimiento intermitente es producido por paradas sistemáticas de las moléculas en zonas concretas del canal.

En este capítulo planteamos la posibilidad de determinar la naturaleza de las paradas detectadas, en concreto si estas son generadas por efectos dielectroforéticos que en el interior del canal. De esta manera, entender el fenómeno detrás de la separación de las moléculas de ADN por tamaño en el interior de un nanocanal.

Con este objetivo, aplicamos campos eléctricos alternos: mediante su valor medio generamos un campo en corriente continua (DC), y mediante la amplitud, un campo de corriente alterna (AC). En principio, la movilidad de la molécula viene dada por el campo en DC, mientras que el campo en alterna (AC) contribuye a aumentar el posible componente dielectroforético que depende del valor eficaz o *rms* del campo. De esta manera, podemos estudiar las variaciones de movilidad y de comportamiento de la molécula respecto al trabajo previo de Salieb-Beugelaar, con el objetivo de determinar el origen de las paradas.

2.2. Materiales y Métodos.

Los dispositivos utilizados son los mismos que utilizó Salieb-Beugelaar en su anterior trabajo (*24*). El dispositivo consiste en dos micro canales principales interconectados por 100 nanocanales de 20 nm de alto por 3 μm de ancho.

El campo eléctrico se genera mediante electrodos de platino colocados en el depósito de salida de los micro canales. Los campos eléctricos de alta intensidad se aplican mediante la combinación de un generador de funciones (Agilent 33220A) y un amplificador (Treck 677B). Utilizamos una solución preparada de TBE (Tris (Merck), Borato (Panreac) y EDTA (Sigma)). En el experimento utilizamos λ-DNA de 48000

pares de bases (New-England Biolabs), marcado fluorescentemente con el intercalador YOYO-1 (Invitrogen).

Para registrar el movimiento de las moléculas utilizamos un microscopio Leica con una cámara refrigerada iXon (Andor). A partir de las imágenes adquiridas se deriva la movilidad de la partícula. Para facilitar el estudio estadístico de los efectos de los campos alternos sobre el movimiento de las partículas, utilizamos dos tipos de movilidades: una movilidad calculada como la velocidad media de largos recorridos, que denominamos "*overall*", y otro tipo de movilidad obtenida en pequeñas distancias o segmentos que llamamos "*go*".

2.3. Resultados

2.3.1. Simulación de la deformación del campo eléctrico

Nos preguntamos si la rugosidad de las paredes del nanocanal puede generar una deformación efectiva del campo eléctrico, que pueda producir fenómenos dielectroforéticos. De las imágenes de microscopia de fuerza atómica (AFM) se obtiene una imagen de la superficie del canal en la que se observa que la rugosidad consiste en agujeros relativamente profundos, con un valor efectivo de 1.2±0.4 nm.

Para simular la distribución del campo eléctrico en el interior de nuestro canal, utilizamos un aplicativo de simulación (Multiphysics COMSOL). Sobre un corte axial del canal de 200 nm de largo por 20 nm de alto, aplicamos un campo eléctrico de 12 kV/m. En las paredes superior e inferior del canal, se han dispuesto una serie de agujeros y grietas para simular los que se han encontrado en la imagen de AFM.

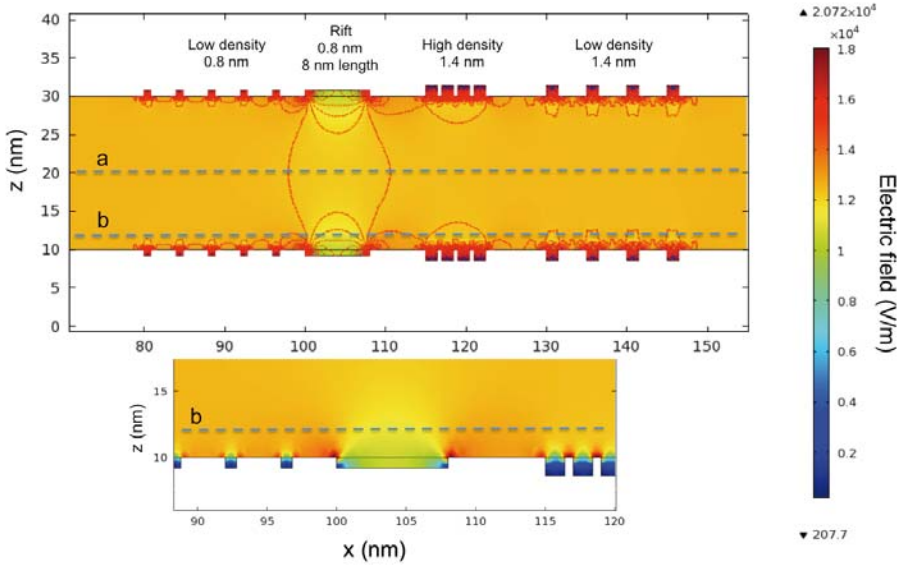

Figura 16: Representación de la distribución del campo eléctrico en un nanocanal, en la superficie del cual se han colocado agujeros y grietas para simular los detectados mediante microscopia de AFM. La representación por colores indica la intensidad de campo eléctrico. Las líneas rojas delimitan las zonas de igual valor de campo eléctrico. El efecto de la grieta si tiene un efecto en toda la sección del canal, mientras que los agujeros solo generan variaciones de campo locales muy cerca de la pared del canal.

El resultado de la simulación se puede observar en la Figura 16, que representa en colores la intensidad del campo eléctrico y su distribución. Las simulaciónes demuestran que las rugosidades y, en especial, la grieta generan cambios en la distribución del campo eléctrico y, que esta variación de campo depende del tamaño de los agujeros. Lo que también observamos es que este efecto se produce muy cerca de la superficie de las paredes, pero la grieta es capaz de afectar a la distribución del campo en toda la sección del canal, generando un mínimo de campo local, que puede estar involucrado en el mecanismo de atrapamiento.

2.3.2. Régimen de movimiento

Los resultados obtenidos presentan una diferencia clara entre dos tipos de movimiento y su dependencia con la intensidad de campo. En la Figure 2.13 se presenta la trayectoria de una única molécula de ADN a través de un nanocanal junto con la posición y velocidad de la partícula en cada instante de tiempo. El campo eléctrico aplicado es de 8 kV/m (DC) y 10 kV/m de amplitud (AC).

Para esta intensidad de campo, el movimiento de la molécula es fluido. Pero se pueden identificar algunos lugares concretos en los que la velocidad decae significativamente y las partículas son atrapadas por cortos periodos de tiempo. En particular ésta se para en los puntos 45 μm y 65 μm. En general, se observa que bajo estas condiciones de campo, las partículas siguen un camino preferente y que su velocidad se reduce en los mismo lugares.

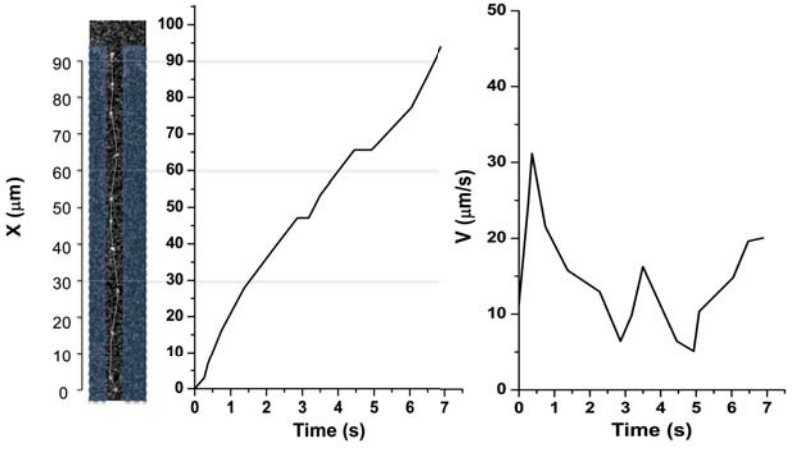

Figura 17: Representación del movimiento de una sola molécula de λ-DNA cuando se aplica un campo eléctrico de baja intensidad (DC 8 kV/m and AC 10 kV/m). La imagen se ha generado acoplando 11 fotogramas de una adquisición de video. El canal está delimitado por las marcas azules. Además se incluye la posición y velocidad de la molécula en función del tiempo.

En el caso de intensidades de campos eléctricos elevados, por ejemplo de 160 kV/m (DC) y 160 kV/m de amplitud (AC), el movimiento de las partículas es totalmente diferente. En la Figure 2.16 se puede ver la evolución de una molécula en el mismo nanocanal. El movimiento de las moléculas en este caso, es claramente un movimiento intermitente en el que la molécula es atrapada durante largos periodos de tiempo. Algunas de estas posiciones de parada y atrapamiento coinciden con las que encontramos en el caso de movimiento fluido, en la Figure 2.13.

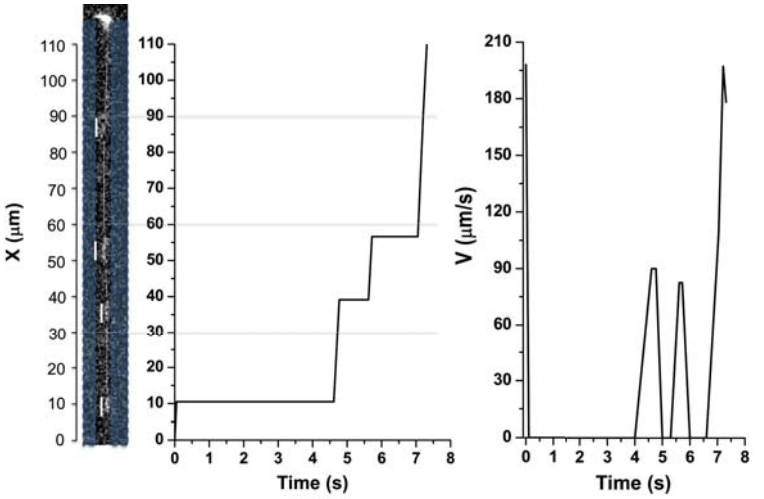

Figura 18: Representación del movimiento de una sola molécula de λ-DNA cuando se aplica un campo eléctrico de baja intensidad (DC 160 kV/m and AC 160 kV/m). La imagen se ha generado acoplando 5 fotogramas de una adquisición de video. El canal está delimitado por las marcas azules. Además se incluye la posición y velocidad de la molécula en función del tiempo.

Estos resultados indican la existencia de caminos preferenciales en el interior de los canales y que los atrapamientos y paradas ocurren en los mismos lugares. Además se observa que la molécula al moverse, experimenta una mecánica de movimiento en la que se estira y se pliega. Estos dos resultados indican la existencia de algún tipo de barrera física en el interior de los canales.

2.3.3. Movilidad para campos alternos

En la Figure 2.18 presentamos los cálculos obtenidos de movilidad media o "overall" para diferentes campos eléctricos aplicados. En la Figure 2.18 se representan las movilidades de las moléculas para diferentes valores de amplitud (AC), en función de los campos eléctricos aplicados (DC).

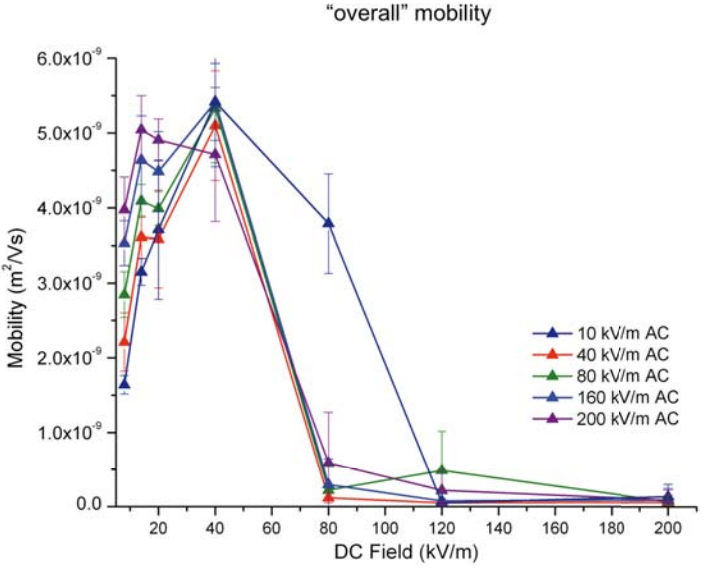

Figura 19: La movilidad media, "overall", en función de la intensidad de campo eléctrico en corriente continua para diferentes amplitudes de campo en corriente alterna añadidas. Las marcas representan la media, y la barras la desviación estándar. Se puede observar como la movilidad depende del campo eléctrico en corriente continua aplicado, de manera que la movilidad aumenta hasta un límite de intensidad de campo de 40kV/m. A partir de este límite la movilidad cae drásticamente y aparece el movimiento intermitente. Por debajo de este límite, el efecto de la movilidad se ve incrementado con la amplitud.

La movilidad muestra una dependencia general con la intensidad de campo en DC muy similar a la que Salieb-Beugelaar presenta en su trabajo (*24*), con independencia del campo en alterna que se aplica . La movilidad aumenta con el campo hasta un umbral o límite a partir del cual se ve reducida drásticamente. Pero se puede comprobar como para las intensidades de campo inferiores a los 40 kV/m existen diferencias

significativas, de manera que la movilidad también aumenta cuando aumenta la amplitud del campo utilizado.

Los resultados de la movilidad junto con el estudio de la dinámica del movimiento de las moléculas contradicen nuestra hipótesis de paradas generadas por fenómenos dielectroforéticos. Al contrario de lo esperado, al aplicar campos en alterna, el comportamiento de las moléculas no presenta cambios significativos respecto a los resultados anteriores (*24*).

2.4. Polyvynilpyrrolidone (PVP) como gel

Comparando los resultados obtenidos con la literatura sobre sistemas de electroforesis en gel (*25, 26*) y con los modelos de movilidad descritos por Slander y Noolandi (*27*), podemos afirmar que las moléculas se encuentran barreras físicas y constricciones en el interior del nanocanal. Además, en los sistemas de separación en gel que utilizan campos en corriente alterna para desplazar las moléculas (BSFGE, biased sinusoidal field gel electrophoresis, en sus siglas en ingles), se observa la mecánica de movimiento en el que la molécula se encoge y estira (*28*), de la misma manera que se observa en el movimiento fluido.

Las imágenes de AFM muestran una superficie de canales pulida, presentando valles, y no picos, que puedan interferir en el movimiento de la molécula. Por otro lado, las longitudes de las cadenas de PVP utilizadas en nuestro caso pueden alcanzar los 25 nm, lo que podría generar localmente una barrera. La fuerte carga superficial de las paredes de los canales y la concentración de polímero nos permite estimar que la capa absorbida en las paredes del canal puede alcanzar un grosor de 4 nm, lo que puede generar una reducción de la sección del canal a 12 nm. Estos datos nos permiten pensar que este polímero, al ser absorbido en las paredes del canal, forma una serie de barreras, enredos y una reducción efectiva de la sección del canal, que generan tanto la separación como el comportamiento descrito.

2.5. Conclusiones

Los resultados obtenidos del movimiento de las moléculas, y la evolución de la movilidad en dependencia con los campos eléctricos, son compatibles con un movimiento en condiciones en gel.

Los resultados de los experimentos tienden a demostrar que la hipótesis de trampas dielectroforéticas no es consistente. Por otro lado, el movimiento observado de las moléculas parece indicar la presencia de barreras físicas en el interior de los canales.

El polímero utilizado en el experimental parece ser el mejor candidato para ser el responsable de las paradas, mediante la reducción de la sección del canal y la aparición de obstáculos, generando puntos de atrapamiento en el interior del canal.

3. Manipulación celular

3.1. Introducción

Los dispositivos para la atención médica primaria requieren de herramientas de manipulación celular con una instrumentación sencilla eficaz. Una solución muy interesante son los campos eléctricos, que pueden ejercer fuerzas sobre las células mediante fenómenos como la electroforesis y dielectroforésis sin necesidad de marcadores o actuadores (*17*). De las dos, la fuerza dielectroforética es las más sencilla de implementar en entornos microfluídicos utilizando microelectrodos desde el interior del dispositivo.

Dentro de los sistemas de separación mediante dielectroforesis, nosotros nos centramos en aquellos que pueden realizar una separación celular en condiciones de flujo continuo. Estos sistemas son muy útiles en los sistemas POC modulares. En la literatura existen varios ejemplos muy interesantes, tanto desde el punto de vista de diseño como de las capacidades de separación (*29-38*).

Desde el punto de vista de la integración y miniaturización pueden resultar inconvenientes las dimensiones que presentan la mayoría. Estas dimensiones están relacionadas con el hecho de que la fuerza dieléctrica es más débil que la fuerza de arrastre que experimentan las células contenidas en un fluido en movimiento. La manera más sencilla de reducir la velocidad del fluido sin comprometer la capacidad de volumen procesado por tiempo, es aumentar la secciones y tamaño de los canales. Los dispositivos capaces de separar o manipular células en velocidades elevadas, suelen utilizar soluciones tampón isotónicas de baja conductividad. El uso de bajas conductividades requeriría un pretratamiento de la muestra, ya que el medio fisiológico suele ser de alto contenido iónico.

Nuestro objetivo en este capítulo es obtener un dispositivo capaz de separar células por tamaño en condiciones de flujo mediante fuerzas dielectroforéticas, en un dispositivo

de dimensiones reducidas que facilite la integración y en condiciones fisiológicas de alta conductividad.

3.2. Diseño del separador y balance de fuerzas

En un sistema de separación de flujo continuo la mayor fuerza en competición con la fuerza dielectroforética es la de arrastre que ejerce el fluido en movimiento sobre la partículas que contiene. La velocidad de la partícula se define como la resultante de las dos fuerzas actuando sobre ella, como expresa la ecuación 1.

$$u_p = v - \frac{a^2 \varepsilon_m \mathrm{Re}[CM] \nabla |E|^2}{6\eta} \qquad \text{Ecuación 1.}$$

La velocidad de la partícula (u_p)es el resultado de la diferencia entre la fuerza de arrastre del fluido y la fuerza dielectroforética, que depende principalmente de la intensidad de campo *E*, la parte real del factor CM y el radio de la célula *a* (*v* es la velocidad del fluido, ε_m permitividad del medio, η es la viscosidad del fluido). Tal y como expresa la ecuación 1, la competencia entre las dos componentes mecánica y eléctrica tiene una relación cuadrada con el radio de la célula. De esta manera, la relación con el tamaño está implícita en la ecuación y así la capacidad de distinguir entre tamaños celulares.

La estrategia que nos planteamos es la de generar un sistema barrera que cree un máximo local de campo eléctrico que repela las células (dielectroforesis negativa) en competencia con el flujo, de manera que para una misma velocidad las células de un tamaño menor a *a* serán arrastradas por el flujo, mientras que células mayores que *a* serán desviadas de la trayectoria del flujo.

Para generar máximos de campo eléctrico que tengan efecto en toda la sección del canal utilizamos barreras dieléctricas. Estas son capaces de generar un campo eléctrico no homogéneo, apareciendo máximos locales que tienen influencia en toda la altura del

canal. La Figure 3.17 presenta la comparación de la distribución de campo eléctrico generado únicamente por un par de electrodos y utilizando barreras dieléctricas.

Proponemos un dispositivo que implemente las barreras dieléctricas como columnas de PDMS, y para garantizar que las células sean influenciadas por los máximos de campo, utilizamos la focalización hidrodinámica. Para ello, planteamos dos canales independientes que tienen un punto de unión en el que se presentan las columnas de PDMS. El sistema consta de tres entradas de fluido, en el canal superior hay dos entradas, una para la muestra y otra para el fluido de focalización principal, la tercera entrada de fluido se coloca en el canal inferior.

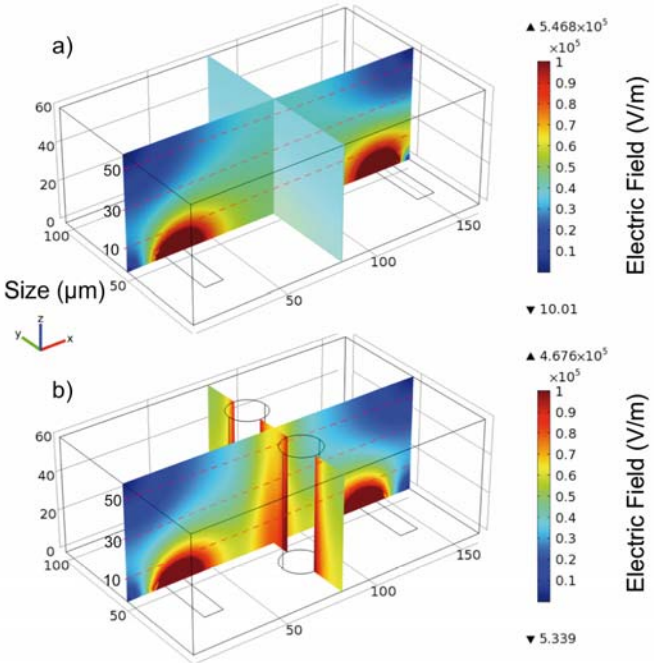

Figura 20: Comparación de la distribución de campo eléctrico en el caso de utilizar o no barreras dieléctricas con electrodos coplanares. Los electrodos se encuentras separados 100 μm. En el primer caso (a) se identifican los máximos locales en los perfiles de los electrodos, y en el espacio entre electrodos el campo es aparentemente homogéneo. En el caso (b) las barreras dieléctricas generan otro máximo local entre las columnas.

3.3. Materiales y métodos

El flujo continuo de la muestra y de los flujos de focalización es controlado por bombas para jeringas (KdScientific), que se inyectan en el interior del dispositivo mediante tres entradas. El campo eléctrico se genera aplicando una señal en corriente alterna, gracias a un generador de funciones (TABOR Electronics).

Para estudiar la evolución de las partículas y cuantificar la separación utilizamos una cámara Hamamatsu instalada en un microscopio invertido Olympus IX71. La eficiencia de separación se calcula contando las partículas que son desviadas del total de las partículas que fluyen entre las barreras en 7 experimentos independientes para cada una de las condiciones de flujo ensayadas.

3.4. Resultados

3.4.1. Separación de partículas de látex

La capacidad de separación de partículas por tamaño se realiza utilizando partículas de látex de diferentes tamaños, de 10 μm y 6 μm de diámetro. Las partículas se disuelven en agua desionizada con una conductividad de 0.4 mS/m. Para este experimento utilizamos una señal de 10 Vpp con una frecuencia de 10^7 Hz.

En la Figure 3.21 se observa una imagen real del sistema de separación con un esquema para indicar la distribución del fluido focalizado y las fuerzas aplicadas. La fuerza de arrastre (drag), en gris, obliga a las partículas a cruzar desde el canal superior hacia el inferior. La fuerza DEP, en rojo, representa la fuerza generada por el campo eléctrico cuando se activa el generador de funciones.

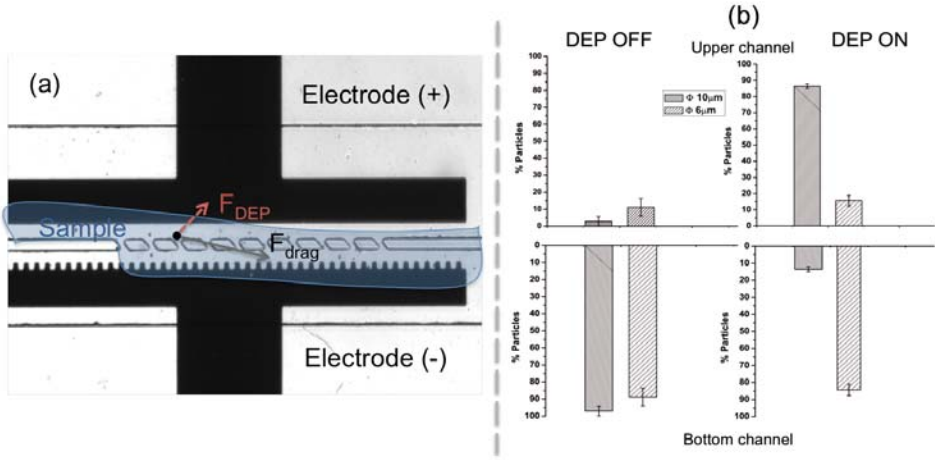

Figura 21: Resultados de la separación del sistema en condiciones de flujo de 0.6 μL/min para la muestra y de 0.8 μL/min para la focalización superior. La imagen de la izquierda es la zona de separación, donde se indica el camino de la muestra para las condiciones de focalización, además de un esquema de las fuerzas que participan. En el caso de que el campo eléctrico sea activado aparecerá el componente dielectroforético del esquema. En la imagen de la derecha se presentan los resultados y recuento de las trayectorias de dos tamaños de partículas. En el caso de ausencia de la fuerza dielectroforética los dos tipos de partículas son desviados hacia el canal inferior. En el caso de la aplicación del campo, las partículas más grandes se ven afectadas por el campo y son desviadas permaneciendo en el canal superior, mientras que en el caso de las partículas pequeñas, la fuerza dielectroforética es menor que la de arrastre y se ven forzadas a pasar al canal inferior.

En la Figure 3.21b se muestra la distribución de las partículas cuando el campo eléctrico está desactivado (DEP OFF) y cuando está activado (DEP ON). En el caso en que no se aplica el campo eléctrico la mayor parte de las partículas cruzan la intersección arrastrados por el flujo. En el momento en que se aplica el campo eléctrico, las partículas de mayor tamaño experimentan una fuerza de repulsión mayor que las pequeñas. Esta fuerza es suficiente para contrarrestar la fuerza de arrastre del flujo. El resultado es que un 90% de las partículas de 10 μm se mantienen en el canal superior. Las condiciones de flujo son de 0.6 μL/min para los flujos de focalización y

0.8 μL/min para el flujo de la muestra. Estas condiciones de flujo implica una velocidad lineal de 1.3 mm/s.

3.4.2. Separación de glóbulos rojos y monocitos

El mismo sistema se utiliza para estudiar la capacidad de desviación de células sanguíneas y probar la existencia de una ventana de flujos que permita la separación por tamaño. En este experimento utilizamos glóbulos rojos obtenidos de donantes y monocitos cultivados de la línea inmortal THP-1 disueltos en PBS con una conductividad medida de 1.6 S/m. La señal utilizada en este experimento es una señal sinusoidal de 10 Vpp y 10^6 Hz.

La tabla 1 indica si el sistema es capaz de desviar las células en diferentes condiciones de flujo de la muestra, en todos los casos los flujos focalización son de 0.6 μL/min. Mientras que los glóbulos rojos son desviados en competencia con flujos de hasta 0.2 μL/min, la fuerza experimentada por las células THP-1 permite que sean desviadas para flujos mayores, por lo que la separación sería efectiva para estas condiciones de flujo.

	0.1 μL/min	0.2 μL/min	0.3 μL/min	0.4 μL/min
RBCs	✔	✔	✖	✖
THP-1	✔	✔	✔	✖

Table 1: Esta tabla indica la desviación de las células para diferentes condiciones de flujo de la muestras. √, en el caso de que sean desviadas o ×, en el caso de que la fuerza dielectroforética no sea suficiente para desviar la célula. La tabla compara el límite de flujo de muestra para encontrar las condiciones óptimas para realizar la separación de los dos tipos de células. El marco rojo indica las condiciones más favorables para la separación.

Las eficiencias de separación demostradas por el dispositivo son significativas en comparación con la mayoría de los dispositivos que trabajan en condiciones

fisiológicas de alta conductividad. Aunque nuestro dispositivo no ha obtenido resultados muy significativos en términos de caudal procesado, sí que lo son las velocidades lineales, lo que significa que las barreras dieléctricas generadas son muy eficientes.

3.5. Conclusiones

El dispositivo presentado es capaz de desviar células de su trayectoria en condiciones fisiológicas utilizando la dielectroforesis negativa. En este sentido se han encontrado las condiciones de focalización óptimas para poder separar dos tipos celulares por tamaño. Este sistema ha sido capaz de desviar monocitos viajando a velocidades de 1 mm/s en un sistema de dimensiones muy reducidas, lo que significa un mejora sobre otros sistemas que trabajan en condiciones fisiológicas.

Podemos afirmar que este sistema es una buena solución para ser integrado en sistemas microfluídicos orientados a integrar sistemas POC.

4. Microcitómetro de impedancia

4.1. Introducción

La citometría de flujo es un sistema ampliamente utilizado en el diagnóstico de enfermedades y en otros estudios (*11*). La microcitometría ha sido durante los últimos años un tema muy estudiado debido a sus múltiples aplicaciones. En la literatura se pueden encontrar gran cantidad de dispositivos y métodos (*13*).

Los citómetros basados en medidas de impedancia tienen una serie de ventajas respecto a los sistemas Coulter (*12*). Primero, permiten obtener más información sobre las celulas, y segundo, que los campos eléctricos alternos son más sencillos de aplicar. Pero por otro lado, requieren de un sistema de medida más complejo. En la literatura podemos encontrar muchos ejemplos, el primero de este tipo fue desarrollado por Gawad et al. (*39*). En este trabajo presentan un sistema de puente de Wheatstone para transformar las variaciones de impedancia en una señal eléctrica modulada, mediante un sistema *lock-in* la señal es demodulada. Otros utilizan otro tipo de técnicas de transducción pero el tratamiento de la señal normalmente se realiza mediante sistemas comerciales (*40-42*).

Desde el punto de vista de instrumentación, en la literatura hay ejemplos de sistemas electrónicos (*43, 44*), básicamente centrados en la demodulación de la señal obtenida de un transductor de impedancia. Los más destacados se centran en el tratamiento de la señal mediante elementos de tratamiento de señal digital, que suelen ser costosos.

Nuestro objetivo es desarrollar un sistema de instrumentación de bajo coste que nos permita además de contar la población celular, realizar la medición del tamaño de la célula. Para validar las transiciones eléctricas obtenidas utilizamos un sistema óptico de detección. Este sistema nos permite comprobar el funcionamiento de la instrumentación y, además, caracterizar y analizar las señales obtenidas.

4.2. Materiales y métodos

4.2.1. Sistema electrónico e instrumentación

El sistema eléctrico propuesto está basado en la arquitectura típica de un sistema demodulador clásico analógico. La instrumentación de demodulación consta de tres elementos básicos un rectificador de onda completa, un filtro pasa bajos para la eliminación de la señal portadora y finalmente un filtro pasa altos para estabilizar la señal y eliminar cualquier potencial en corriente continua.

Para el control y caracterización se han desarrollado una serie de aplicaciones informáticas para la adquisición de la señal eléctrica de la instrumentación de forma sincronizada con la adquisición de imágenes reales del interior del dispositivo en LabVIEW. Las señales eléctricas se adquieren mediante una tarjeta de adquisición (National Instruments), mientras que las imágenes son adquiridas mediante una cámara de alta velocidad (Fotron) conectada a un microscopio invertido (Olympus IX71). Posteriormente, el análisis conjunto de las señales de forma sincronizada se realiza mediante un aplicativo en MATLAB.

4.3. Resultados

4.3.1. Estudio de las transiciones eléctricas

Este sistema de instrumentación ha sido testado utilizando glóbulos rojos obtenidos de donantes y disueltos en PBS (1.6 S/m). Los resultados confirman la capacidad de la instrumentación para detectar los cambios de impedancia generados por las células al pasar sobre el área de detección, así como la dependencia de las amplitudes y morfologías de la señal obtenida con la geometría de los canales y el equilibrio óptimo del puente.

El sistema sincronizado nos permite evaluar las señales electrónicas con la posición de la célula en el área de detección, como muestra la Figure 4.13. Gracias a la sincronización, se ha podido certificar la fiabilidad de la electrónica para detectar

células. Se ha demostrado que más del 95 % de las transiciones detectadas están generadas por la transición de las células sobre la zona de detección. El 5 % restante se debe a transiciones eléctricas que superan el umbral de detección, pero que en la imagen óptica no es posible detectar la célula, posiblemente por una cuestión focal del microscopio.

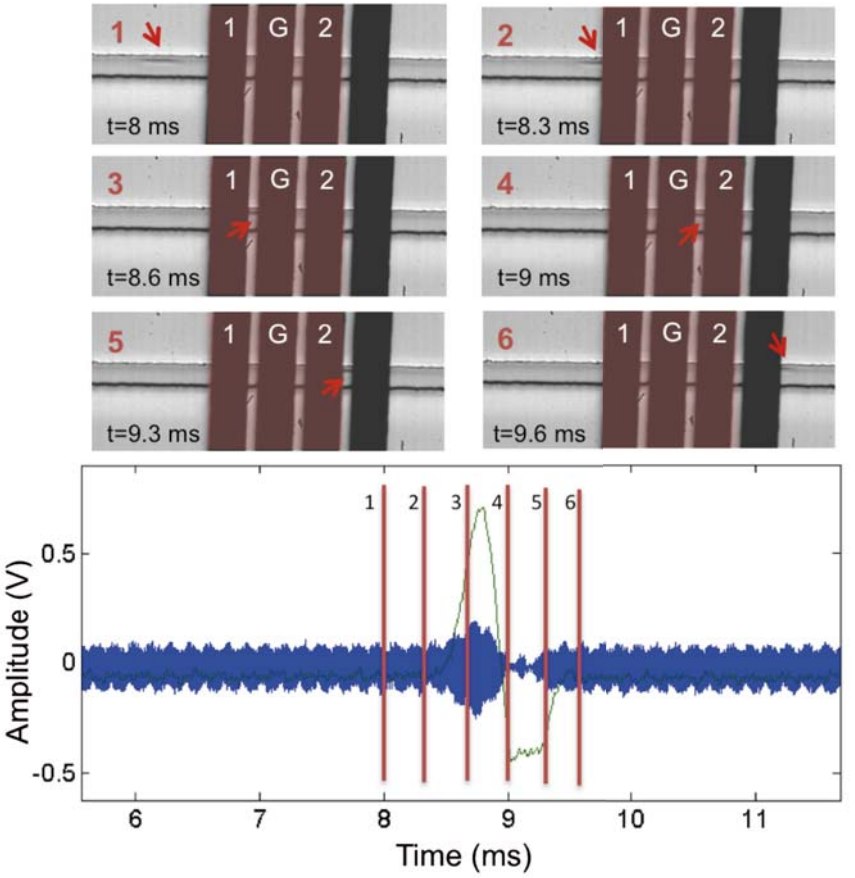

Figura 22: Representación de la sincronización eléctrica y óptica de la transición de un glóbulo rojo cruzando la zona de detección. La señal azul es la señal que se obtiene del puente de Wheatstone y la verde es el resultado de la etapa de demodulación. Las imágenes representan diferentes posiciones de la célula. Las barras rojas indican el instante de tiempo de cada imagen.

4.3.2. Velocidad de procesado

Para evaluar la capacidad de procesado del sistema hemos utilizado glóbulos rojos de donantes y células cultivadas THP-1, disueltas en PBS en una relación de 100:1. En este caso utilizamos un dispositivo microfluídico con una sección de canal de 20 μm de ancho por 20 μm de alto.

La capacidad de detección se observa en la Figure 4.16, mediante el resultado de una adquisición de 8.8 segundos en la que se han detectado 4767 células en total. La velocidad de transición mínima de las células es de 0.2 ms, lo que nos lleva a afirmar que la instrumentación presentada podría alcanzar un velocidad de procesado de 5000 partículas por segundo.

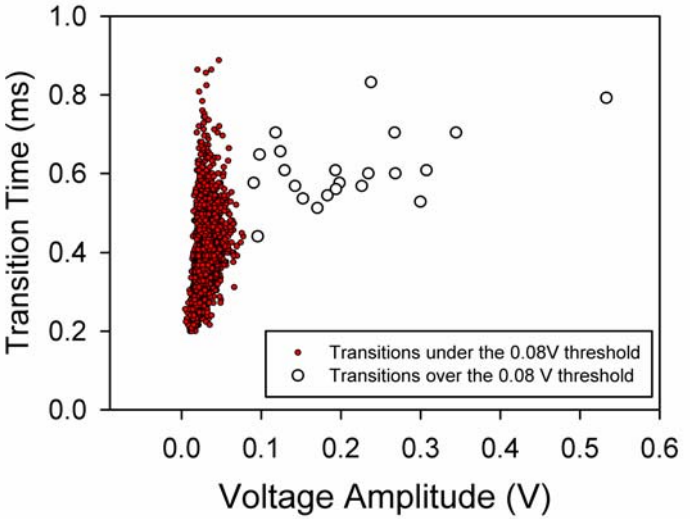

Figura 23: Representación del tiempo de paso frente a la amplitud de 4767 transiciones de células detectadas en 8.8 segundos. Esta adquisición se ha realizado a alta velocidad de la muestra, demostrando la capacidad de detectar 542 células por segundo. En esta adquisición se han utilizado dos umbrales para poder distinguir entre dos tipos celulares. El umbral fijado a 0.01 V para definir que la transición eléctrica ha sido producida por célula, mientras que el umbral fijado en 0.08 V para detectar los monocitos.

Por otro lado es importante remarcar que las transiciones eléctricas presentan diferencias en amplitud que permiten pensar que el sistema es capaz de discriminar el tamaño celular.

4.3.3. Determinar el volumen celular

Para determinar la relación entre la amplitud de las señales eléctricas obtenidas y el volumen de las células, seleccionamos de una serie de adquisiciones independientes en las mismas condiciones de equilibrio de las dos ramas del puente, una serie de transiciones eléctricas validadas con la imagen de la célula que ha generado la transición. De esta manera, estamos reduciendo las variaciones en amplitud derivadas de la posición de la célula respecto los electrodos.

El resultado se presenta en la Figure 4.18. En el caso de glóbulos rojos se ha reducido la población a 63 transiciones y en el caso de monocitos a 10 transiciones. En este estudio se han incluido una serie de células anómalas de gran tamaño que han generado amplitudes de transición muy elevadas. El cálculo del volumen de las células se deriva de calcular su diámetro a partir de la imagen obtenida, teniendo en cuenta que los monocitos en suspensión son esféricos mientras que los glóbulos rojos se consideran un cilindro de altura 2.5 μm. De esta manera podemos determinar una relación lineal entre el volumen de la partícula y la amplitud de su transición eléctrica.

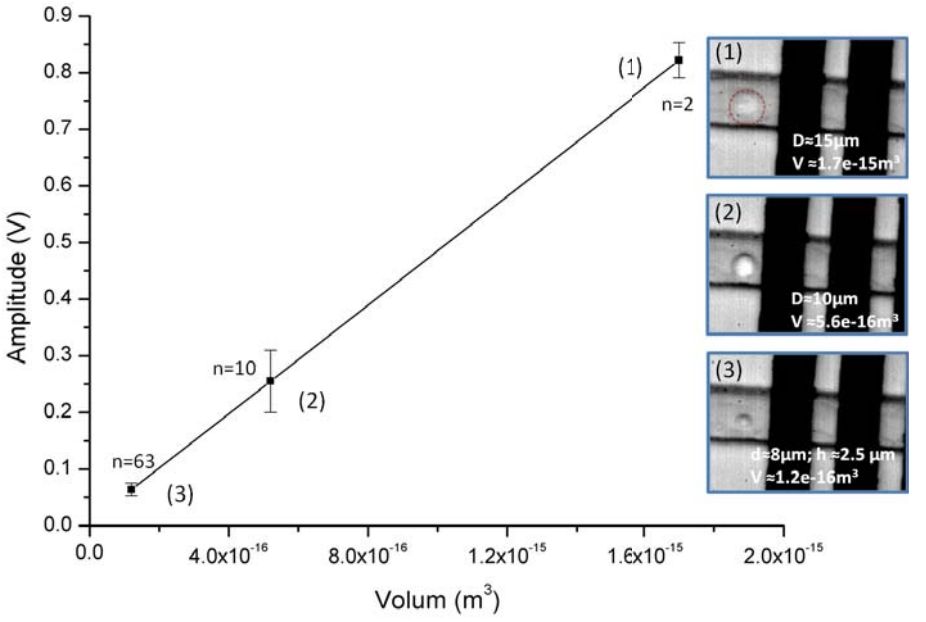

Figura 24: Relación entre la amplitud de las transiciones y el volumen calculado de la célula. En esta gráfica se puede ver como, bajo las mismas condiciones de equilibrio del puente, las amplitudes de las transiciones siguen una relación lineal con el volumen celular. En la imágenes se muestran los tres tipos celulares utilizados para calcular los volúmenes. Para monocitos (1 y 2) el volumen se ha calculado considerándolos esferas y el diámetro se ha calculado mediante procesado de imagen. El volumen de los glóbulos rojos se ha calculado como un cilindro de altura 2.5 µm con una base calculada mediante el procesado de imagen.

4.4. Conclusiones

Se ha desarrollado un sistema de instrumentación capaz de detectar células mediante la utilización de un método de medida basado en la detección de impedancia eléctrica en un sistema microfluídico.

El sistema de instrumentación se ha validado utilizando un sistema óptico sincronizado que nos ha permitido estudiar desde la fiabilidad del sistema. Mediante este método

hemos detectado que el equilibrio del puente tiene mucha influencia sobre la morfología y las amplitudes de las transiciones.

El sistema ha demostrado tener una capacidad de procesado muy elevada, con la posibilidad de alcanzar una velocidad de 5000 células por segundo. Por otro lado, se ha demostrado que las diferencias relativas en amplitud de transiciones obtenidas de células de diferentes tamaños tienen una respuesta lineal con el volumen.

Por lo tanto, la instrumentación presentada es una posibilidad barata y sencilla, óptima para ser utilizada como método de cuantificación en sistemas POC.

5. Citometría y focalización hidrodinámica

5.1. Introducción

El sistema microfluídico de detección utilizado en esta tesis consiste en una estructura de electrodos coplanares, muy sencilla de fabricar y barata. Pero esta geometría tiene un importante inconveniente, la distribución del campo eléctrico que genera en el interior del canal. Esta distribución de campo no es homogénea e implica una reducción de la sensibilidad en los planos más alejados de los electrodos.

En este capítulo nos planteamos mejorar este sistema de detección utilizando la focalización hidrodinámica. Estudiamos dos casos concretos. Primero estudiamos la posibilidad de mejorar la sensibilidad del sistema, utilizando la focalización hidrodinámica para mejorar la relación de impedancia ($R_0/\Delta R$), que se obtiene de partículas muy pequeñas comparadas con la sección del canal. Segundo, nos planteamos mejorar la capacidad de recuento de glóbulos rojos, de manera que podamos asegurar que detectamos todas las células y poder calcular la densidad celular de la muestra.

El objetivo principal de este capítulo es demostrar que al focalizar hidrodinámicamente el flujo de la muestra, utilizando líquidos de muy baja conductividad como flujos de focalización, la respuesta en impedancia del sistema mejora las prestaciones de detección.

5.2. Resultados del sistema de alineamiento

En este primer apartado el objetivo principal es demostrar que mediante la focalización podemos aumentar la sensibilidad del sistema, de manera que podamos detectar una célula muy pequeña en un canal de mayores dimensiones. La idea principal es mejorar la relación ($R_0/\Delta R$), para que los cambios de impedancia generados por partícula puedan ser detectables.

5.2.1. Aumento de la sensibilidad

En este caso hemos utilizado partículas de 20 μm en una canal de 180 μm de ancho por 65 μm de alto. Las condiciones de focalización generan una dimensión efectiva del flujo de la muestra de 25 μm de ancho y 32 μm de alto.

La Figure 5.6 presenta la comparación de los histogramas de amplitud de las transiciones eléctricas detectadas por el sistema. En ella se puede comprobar como en el caso de las partículas focalizadas la sensibilidad mejora aumentando la amplitud media de las señales.

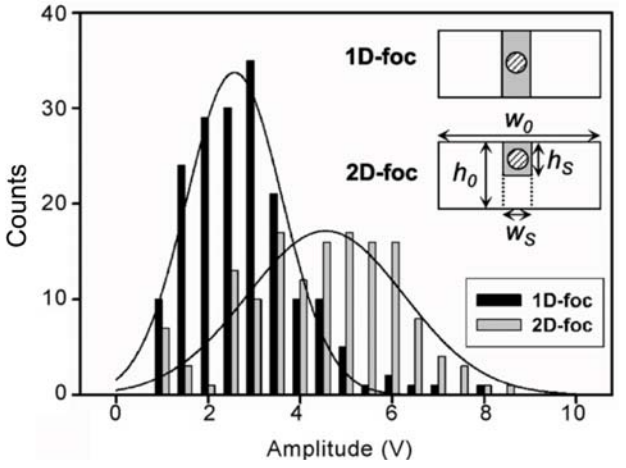

Figura 25: Comparación de los histogramas de las amplitudes obtenidas para focalización 1D y 2D. Las medias calculadas de las distribuciones son 2.8 y 4.4 V, respectivamente. La distribución se ha ajustado a una distribución normal.

5.2.2 Detección de levaduras

Utilizamos una muestra de levaduras (*Saccharomyces cerevisiae*) en una disolución de 27 g/L de NaCl, con una conductividad de 2.87 S/m. Las condiciones de focalización se fijan para crear una apertura de 20 μm de ancho por 20 μm de alto. La Figure 5.7 presenta la adquisición eléctrica y óptica obtenida de una transición detectada.

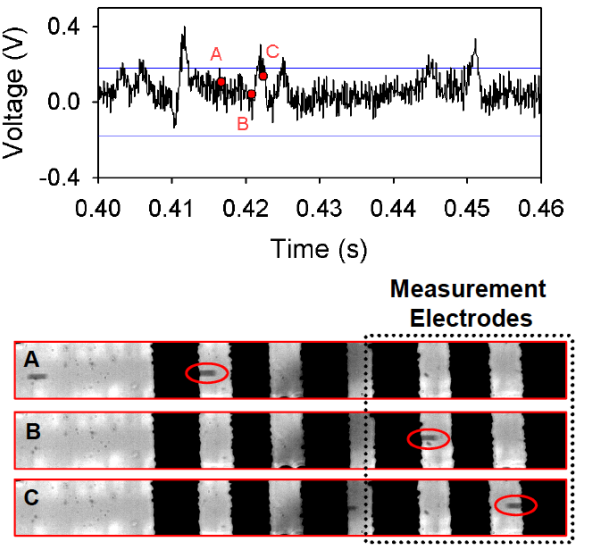

Figura 26: Sincronización de las medidas eléctrica y óptica del paso de levaduras sobre la zona de detección. En la parte superior se presenta la adquisición eléctrica de la señal, las líneas horizontales indican el nivel del umbral eléctrico fijado para la detección. La parte inferior muestra la levadura macada con un circulo en tres posiciones diferentes, el instante de tiempo al que corresponden está indicado en la señal eléctrica.

5.3. Resultados de recuento de glóbulos rojos

Debido a su forma tan característica, los glóbulos rojos presentan algunas dificultades de detección cuando se usan electrodos coplanares. Por ejemplo, un sistema fluídico de 10 μm de ancho por 10 μm de alto podría parecer una buena opción para realizar un recuento efectivo, pero estas células pueden tomar diferentes posiciones y orientaciones en el interior del canal (Figure 5.8) que dificultan un recuento efectivo de su población.

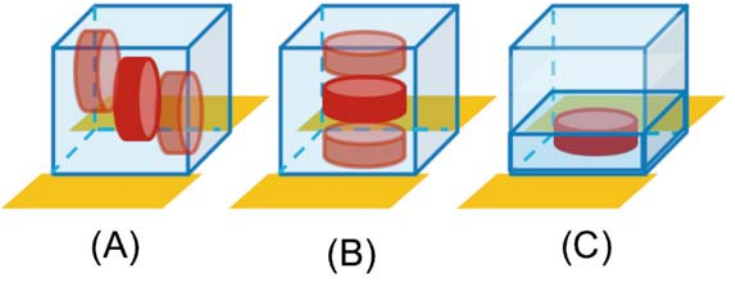

Figura 27: Representación esquemática de las posiciones que un glóbulo rojo puede tomar en el interior de un canal de 10 μm de ancho por 10 μm de alto, representadas en el esquema (a) y (b). Esta variabilidad de su posición relativa a los electrodos puede generar una desviación de las amplitudes eléctricas, incluso podría enmascararlas. La focalización se utiliza para orientar y forzar a estas células a viajar cerca de los electrodos como se presenta en el esquema (c).

La focalización hidrodinámica además de alinear las partículas y mejorar la sensibilidad del sistema, se puede utilizar para orientar las células a su paso por los electrodos.

En este apartado comparamos los resultado obtenidos de recuento de una población de glóbulos rojos en condiciones de focalización. Para poder comparar los resultado obtenidos mediante focalización y no focalizados, analizamos los cambios que se producen en el puente de Wheatstone. De esta manera intentamos determinar que las amplitudes de las transiciones solo dependen de la posición de las células respecto a los electrodos y no de cambios en el equilibrio del puente.

En este caso se utiliza una muestra de glóbulos rojos, disueltos en PBS, con una concentración controlada de 10^7 células/mL en un sistema microfluídico de 10 μm de ancho por 8.5 μm de alto. Realizamos una focalización vertical de 1:0.1 μL/min lo que implica una altura efectiva de la sección de la muestra de 7.8 μm de alto, y una focalización efectiva de 1:1 μL/min, que implica una sección efectiva de 4.2 μm. En

los dos casos el equilibrio del puente se mantiene para obtener 0.06 V de amplitud de la señal.

La Figure 5.15 muestra la comparación de las amplitudes, se puede ver claramente como la distribución cambia sensiblemente. Por un lado, aumentan la cantidad de transiciones con amplitud por debajo de 0.4 V, mientras que la población por encima de ese valor se mantienen. Lo que parece indicar que el sistema ha sido capaz de detectar un mayor número de células gracias a la focalización. Este aumento de la población es significativo en tanto en cuanto la densidad celular derivada de las adquisiciones en condiciones de focalización 1:0.1 es de 10^6 células/mL, mientras que para 1:1 es aproximadamente de 10^7 células/mL, que corresponde con la densidad real calculada de la muestra.

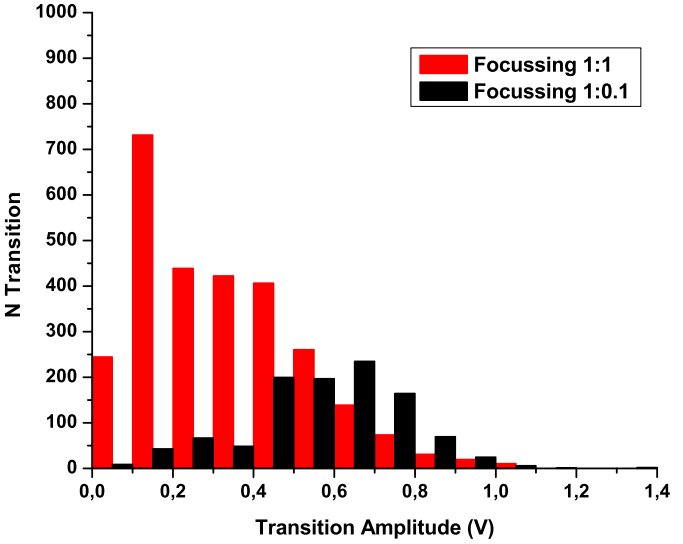

Figura 28: Histograma de la distribución de las cuentas obtenidas. La distribución de barras rojas representan la distribución para las condiciones de focalización 1:1, mientras que las barras negras indican la distribución de amplitud para las condiciones de focalización 1:0.1.

5.4. Conclusiones

La focalización hidrodinámica mejora sensiblemente la prestaciones del sistema de detección basado en electrodos coplanares. Primero, porque además de ser un sistema de alineamiento y ordenación muy válido para sistemas de recuento de células. Y, segundo, porque como se ha demostrado, mejora la sensibilidad y la resolución del sistema en cuanto reduce el error derivado de la posición de las células respecto a los electrodos.

Referencias:

1. G. M. Whitesides, The origins and the future of microfluidics. *Nature* **442**, 368 (2006).
2. T. Vilkner, D. Janasek, A. Manz, Micro total analysis systems. Recent developments. *Analytical Chemistry* **76**, 3373 (2004).
3. P. S. Dittrich, K. Tachikawa, A. Manz, Micro total analysis systems. Latest advancements and trends. *Analytical Chemistry* **78**, 3887 (2006).
4. C. D. Chin, V. Linder, S. K. Sia, Lab-on-a-chip devices for global health: Past studies and future opportunities. *Lab on a Chip* **7**, 41 (2007).
5. P. Yager, G. J. Domingo, J. Gerdes, Point-of-Care Diagnostics for Global Health. *Annual Review of Biomedical Engineering* **10**, 107 (2008).
6. P. Yager, T. Edwards, E. Fu, K. Helton *et al.*, Microfluidic diagnostic technologies for global public health. *Nature* **442**, 412 (2006).
7. F. Sanger, A. R. Coulson, A rapid method for determining sequences in DNA by primed synthesis with DNA polymerase. *Journal of Molecular Biology* **94**, 441 (1975).
8. J.-L. Viovy, Electrophoresis of DNA and other polyelectrolytes: Physical mechanisms. *Reviews of Modern Physics* **72**, 813 (2000).
9. K. D. Dorfman, DNA electrophoresis in microfabricated devices. *Reviews of Modern Physics* **82**, 2903 (2010).
10. G. B. Salieb-Beugelaar, K. D. Dorfman, A. v. d. Berg, J. C. T. Eijkel, Electrophoretic separation of DNA in gels and nanostructures. *Lab on a Chip* **9**, 2508 (2009).
11. H. M. Shapiro, *Practical flow cytometry*. Practical flow cytometry, Third edition (Wiley Liss, New York, ed. Third edition, 1995).
12. W. H. Coulter, U. S. P. a. T. Office, Ed. (United States, 1953), vol. 2,656,508.
13. T. Sun, H. Morgan, Single-cell microfluidic impedance cytometry: a review. *Microfluidics and Nanofluidics* **8**, 423 (2010).
14. M. Ozkan, T. Pisanic, J. Scheel, C. Barlow *et al.*, Electro-Optical Platform for the Manipulation of Live Cells. *Langmuir* **19**, 1532 (2003/03/01, 2002).

15. M. Ozkan, M. Wang, C. Ozkan, R. Flynn *et al.*, Optical Manipulation of Objects and Biological Cells in Microfluidic Devices. *Biomedical Microdevices* **5**, 61 (2003).
16. H. Thielecke, I. Impidjati, H. Zimmermann, G. Fuhr, Gentle cell handling with an ultra-slow instrument: creep-manipulation of cells. *Microsystem Technologies* **11**, 1230 (2005).
17. J. Voldman, Electrical forces for microscale cell mnaipulation. *Annual Review of Biomedical Engineering* **8**, 425 (2006).
18. B. M. Olivera, P. Baine, N. Davidson, Electrophoresis of the nucleic acids. *Biopolymers* **2**, 245 (1964).
19. J. Han, J. Fu, R. B. Schoch, Molecular sieving using nanofilters: Past, present and future. *Lab on a Chip* **8**, 23 (2008).
20. J. Fu, J. Yoo, J. Han, Molecular Sieving in Periodic Free-Energy Landscapes Created by Patterned Nanofilter Arrays. *Physical Review Letters* **97**, 018103 (2006).
21. R. Ogawa, H. Ogawa, A. Oki, S. Hashioka *et al.*, Fabrication of nano-pillar chips by a plasma etching technique for fast DNA separation. *Thin Solid Films* **515**, 5167 (2007).
22. S. Pennathur, F. Baldessari, J. G. Santiago, M. G. Kattah *et al.*, Free-Solution Oligonucleotide Separation in Nanoscale Channels. *Analytical Chemistry* **79**, 8316 (2007).
23. J. D. Cross, E. A. Strychalski, H. G. Craighead, Size-dependent DNA mobility in nanochannels. *Journal of Applied Physics* **102**, 024701 (2007).
24. G. B. Salieb-Beugelaar, J. Teapal, J. v. Nieuwkasteele, D. Wijnperle *et al.*, Field-Dependent DNA Mobility in 20 nm High Nanoslits. *Nano Letters* **8**, 1785 (2008).
25. B. Åkerman, Cyclic migration of DNA in gels: DNA stretching and electrophoretic mobility. *Electrophoresis* **17**, 1027 (1996).
26. A. E. Barron, D. S. Soane, H. W. Blanch, Capillary electrophoresis of DNA in uncross-linked polymer solutions. *Journal of Chromatography A* **652**, 3 (1993).

27. G. W. Slater, J. Noolandi, New Biased-Reptation Model For Charged Polymers. *Physical Review Letters* **55**, 1579 (1985).

28. T. Shikata, T. Kotaka, Biased sinusoidal field gel electrophoresis for large DNA separation. *Macromolecules* **24**, 4868 (1991).

29. Y. Huang, X. B. Wang, F. F. Becker, P. R. Gascoyne, Introducing dielectrophoresis as a new force field for field-flow fractionation. *Biophys. J.* **73**, 1118 (August 1, 1997, 1997).

30. J. Yang, Y. Huang, X.-B. Wang, F. F. Becker *et al.*, Differential Analysis of Human Leukocytes by Dielectrophoretic Field-Flow-Fractionation. *Biophysical Journal* **78**, 2680 (2000).

31. I. F. Cheng, H.-C. Chang, D. Hou, H.-C. Chang, An integrated dielectrophoretic chip for continuous bioparticle filtering, focusing, sorting, trapping, and detecting. *Biomicrofluidics* **1**, 021503 (2007).

32. K.-H. Han, A. B. Frazier, Lateral-driven continuous dielectrophoretic microseparators for blood cells suspended in a highly conductive medium. *Lab on a Chip* **8**, 1079 (2008).

33. M. D. Vahey, J. Voldman, An Equilibrium Method for Continuous-Flow Cell Sorting Using Dielectrophoresis. *Analytical Chemistry* **80**, 3135 (2008).

34. M. S. Pommer, Y. Zhang, N. Keerthi, D. Chen *et al.*, Dielectrophoretic separation of platelets from diluted whole blood in microfluidic channels. *Electrophoresis* **29**, 1213 (2008).

35. S. Chang, Y.-H. Cho, A continuous size-dependent particle separator using a negative dielectrophoretic virtual pillar array. *Lab on a Chip* **8**, 1930 (2008).

36. T. Braschler, N. Demierre, E. Nascimento, T. Silva *et al.*, Continuous separation of cells by balanced dielectrophoretic forces at multiple frequencies. *Lab on a Chip* **8**, 280 (2008).

37. M. D. Vahey, J. Voldman, High-Throughput Cell and Particle Characterization Using Isodielectric Separation. *Analytical Chemistry* **81**, 2446 (2009).

38. S.-I. Han, S.-M. Lee, Y.-D. Joo, K.-H. Han, Lateral dielectrophoretic microseparators to measure the size distribution of blood cells. *Lab on a Chip* **11**, 3864 (2011).

39. S. Gawad, L. Schild, P. Renaud, Micromachined impedance spectroscopy flow cytometer for cell analysis and particle sizing. *Lab on a Chip* **1**, 76 (2001).

40. K. Cheung, S. Gawad, P. Renaud, Impedance spectroscopy flow cytometry: On-chip label-free cell differentiation. *Cytometry Part A* **65A**, 124 (2005).

41. H. Morgan, D. Holmes, N. G. Green, High speed simultaneous single particle impedance and fluorescence analysis on a chip. *Current Applied Physics* **6**, 367 (2006).

42. J. H. Nieuwenhuis, F. Kohl, J. Bastemeijer, P. M. Sarro *et al.*, Integrated Coulter counter based on 2-dimensional liquid aperture control. *Sensors and Actuators B: Chemical* **102**, 44 (2004).

43. F. R. E. De Bisschop, in *Instrumentation and Measurement Technology Conference, 2006. IMTC 2006. Proceedings of the IEEE*. (2006), pp. 525-529.

44. S. Zheng, Y.-C. Tai, in *Microtechnologies in Medicine and Biology, 2006 International Conference on*. (2006), pp. 16-19.

Special acknowledgement

I would like to acknowledge the work done by 5 researchers in the elaboration of the present PhD thesis. Their collaboration, advice and work were essential to the development of this adventure.

First, special thanks to Jan Eijkel and Georgette Beugelaar, who participated in the DNA work. Without Jan, it would have been impossible to explain our results and give sense to my appreciations and ideas about the role of the PVP in the experiments.

Many thanks to Marc Castellarnau, who participated in the Dielectrophoresis work. He believed in my idea of developing a continuous flow separation of cells, and turned it in a reality. He worked in the design of the device and helped me in the fabrication and characterisation experiments.

Special thanks also to Romén Rodriguez-Trujillo and Miquel Garrido, who contributed to the Coulter system. Miquel helped with the design of the electronic system that I have been using all these years. Romén developed the hydrodynamic focussing concept in his thesis and helped me with the signal processing of the large amount of data obtained.

List of publications

Electrokinetic DNA transpot in 20 nm high nanoslits: Evidence for movement through a wall absorbed nano gel.
Castillo-Fernández O, SAlieb-Beugelaar G.B., van Nieuwkasteele Jan, W. Bomer, Johan G. Arundell Martin, Samitier Josep, van den Berg Albert, Eijkel, Jan C.T.
Electrophoresis 2011, 32(18): p.2402-2409.

Electrokinetic techniques applied to electrochemical DNA biosensors
Mir M, Martínez-Rodríguez S, Castillo-Fernández O, Homs-Corbera A, Samitier J.
Electrophoresis 32, 811-821 (2011).

High speed particle detection in a micro-Coulter counter with two-dimensional adjustable aperture
Romen Rodriguez-Trujillo, Oscar Castillo-Fernandez, Miquel Garrido, A. Valencia and G. Gomila
Biosens. Bioelectron. (2008), doi:10.1016/j.bios.2008.04.005

Chips & Tips: Rapid prototyping of a PMMA microfluidic chip with integrated platinum electrodes
Martin Arundell, Adai Colom Diego, Oscar Castillo and Josep Samitier
Lab on a Chip - Chips and Tips 8 (11) (2008)

Congress participation

Selective electroplating of gold electrodes inside microfluidic channels for biomedical sensing

Rodriguez-Trujillo R, Castillo-Fernandez O, Homs-Corbera A, Samitier J,.

Ibernam 2009, Sevilla, Andalucía, Spain, 26th – 27th of November 2009. Proceedings, pp 39.

DNA transport in 20nm Nanoslits by AC and DC electric fields.

G.B. Salieb-Beugelaar, Ó. Castillo-Fernandez, M. Arundell, J.Samitier, A. van den Berg and J.C.T. Eijkel.

Proceedings of the 13th International Conference on Miniaturized Systems for Chemistry and Life Sciences, Jeju, Jeju (Korea) November 1 - 5, 2009.

Study of DNA mobility in 20 nm channels using AC and DC electric fields.
Castillo-Fernandez O, Salieb-Beugelaar G.B, Martin Arundell, Berg A, Jan Eijkel, Samitier J.
10th TNT Trends in Nanotechnology, Barcelona, Spain, 7-11 September 2009, Oral presentation.

Synchronised Instrumentation for a Micro-Coulter Counter.
Castillo-Fernandez O., Rodriguez-Trujillo R., Miquel Garrido, Antoni Valencia, Martin Arundell, Gabriel G.
1st MicroScale Bioseparations and Methods for Systems Biology. Berlin 9-13 Marzo, 2008

Yeast cells detection in a very fast and highly versatile microfabricated cytometer.
Rodriguez-Trujillo R., Castillo-Fernandez O. Arundell M., Josep Samitier and Gabriel Gomila. Proceedings of the 12th International Conference on Miniaturized Systems for Chemistry and Life Sciences, San Diego, California (USA) October 12 - 16, 2008.